Développement d'un dispositif expérimental basé sur ladigitalisation des signaux et dédié à la caractérisation desfragments de fission et des neutrons prompte émis

Nathallia Varapai

N° d'ordre : 3274

CENBG : 2006

THÈSE

Présentée à

L'UNIVERSITÉ BORDEAUX I

ECOLE DOCTORALE DES SCIENCES PHYSIQUES
ET DE L'INGENIEUR

Par **Natalia VARAPAI**

POUR OBTENIR LE GRADE DE

DOCTEUR DE L'UNIVERSITÉ BORDEAUX I

Spécialité : Noyaux, Atomes, Agrégats, Plasmas

****

Titre : Développement d'un dispositif expérimental basé sur la digitalisation des signaux et dédié à la caractérisation des fragments de fission et des neutrons prompte émis

****

Thèse soutenue le : 7 Décembre 2006

Après avis de :

MM. C. Wagemans, Professeur Université de Gand	**Rapporteurs**
MM. H. Faust, Physicien, Institut Laue-Langevin, Grenoble	

Devant la commission d'examen formée de :

Mme. M.M Aléonard, Professeur, Université de Bordeaux I	**Examinateurs**
MM. B. Haas, Directeur de Recherche	
MM. O. Serot, Physicien, CEN Cadarache	
MM. G. Barreau , Directeur de Recherche	**Directeur de thèse**

Centre d'études nucléaires de Bordeaux-Gradignan

- 2006 -

Acknowledgements

A lot of people have contributed to the achievement of this work. I would like to express my gratitude to Dr. Olivier Serot, my supervisor, for his patient teaching, many fruitful discussions, sharing his knowledge with me, and for his inspiring and constructive guidance in the preparation of this manuscript. Dear Olivier, thanks a lot.

I would also like to express my thanks to Dr. Gerard Barreau for all the interesting discussions we had and for his help with the achievement of the experimental part of this work. Dear Gerard, thank you very much.

My very special thanks to Dr. Nikolai Kornilov for his patient guidance, a lot of very helpful discussions and for his help during the experiment and data analysis. My deep thanks to you, Nikolai.

I am very indebted to Dr. Franz-Josef Hambsch for his supervision, his patient teaching and help during my stay at the Institute for Reference Materials and Measurement in Geel, Belgium. Thanks a lot.

I am very grateful to Dr. Stephan Oberstedt for many discussions we had together. I would also like to thank Dr. Shakir Zeinalov and Dr. Vitali Khriatchkov for the constructive discussions we had and their valuable help.

My very special thanks to Olivier Litaize for all his help and for the many interesting discussions we had. My thanks to Patrick Talou for his critical look on my thesis.

I am very grateful to all the LINAC and VdG staff members at the IRMM for their warm welcome and for providing me with the best possible working conditions. Many thanks for the very friendly atmosphere. My special thanks to Volker Fritsch, the technician at the VdG with the "magic hands".

Last but not the least, special thanks to my Mom, Sister and Wouter Geerts. Mom and Alena, huge thanks for believing in me, supporting and encouraging me during the last years and for your love. Thanks a lot for all. I love you very much. Schatje, je bent de beste. Dank je wel voor jouw liefde, steun en vertrouwen in mij.

Contents

Chapter 1

Introduction

Neutron multiplicity investigations and measurements of the fission fragment characteristics in neutron-induced fission reactions on actinides such as ^{239}Pu and ^{235}U in the thermal and resonance energy ranges are very important. First of all, these investigations are necessary for better understanding the basic physics of the fission process. The amelioration of our knowledge of the fission phenomenon lies in particular in the determination of the following nuclear properties:

- the deformation of the two fragments near the scission point;
- partition of Q-value between different degrees of freedom: excitation energy, leading to neutron and γ emission, and kinetic energy;
- the influence of the spin on the emission of the fragment yield and the emission of prompt neutrons.

These investigations are also relevant in reactor control and safety issues. Fission yield measurements on both ^{235}U [Ham99] and ^{239}Pu [Dem02] have shown fluctuations of the fission fragment mass distribution from resonance to resonance. Those fluctuations are larger in the case of ^{235}U. ^{239}Pu is a major actinide and its importance is growing due to its use in MOX (mixed oxide) fuel elements. For resolved neutron-resonance energies the fluctuations of the average number of prompt neutrons, $\overline{\nu}_p$, have been observed as a function of incident neutron energies [Fre74]. The origin of these fluctuations has not been clearly identified. Comparing prompt neutron multiplicity data from different nuclear data

libraries (as ENDF-BVI.8, JEF-2.2, JEFF-3.1 and JENDL-3.3), differences can be observed for both nuclei ^{239}Pu and ^{235}U (Fig.1.1). So, the neutron multiplicity investigations for these actinides in resonance neutron induced fission are strongly needed.

However, the measurement of the fission fragment properties and the determination of $\overline{\nu}_p$ for the reaction ^{239}Pu(n,f) in the above mentioned energy region is rather difficult for several reasons:

- only one measurement of the fission fragment and neutron properties at thermal and 0.3 eV energy points was performed [Bat04];
- it is necessary to find a good compromise between the need of a thick target in order to increase the statistics and the high intrinsic α-decay rate of ^{239}Pu which affects the resolution of the detector;
- it is necessary to have a highly energy-resolved neutron beam;
- the fact that the emitted neutrons have to be measured in coincidence with fission fragments decreases the geometrical efficiency of the whole detector system. So, several neutron detectors are needed, which complicates the acquisition system.

Recently, the problem of the fission fragment property determination for ^{239}Pu was studied. Due to the thick target a special scheme for the rejection of pile-up events has been developed [Dem98, Dem02]. It was shown that it is possible to reject more than 90 % of the pile-up pulses for a ^{239}Pu sample with an activity of $\sim$ 1 MBq. But the results showed too large uncertainties. So, several improvements are necessary in order to obtain a better accuracy. One way is to use the digital technique. In recent years, digital processing technology is slowly replacing the traditional analogue technique for nuclear physics applications [Kor03, Bar04].

This new technique is based on the digitalization of the signals from the detectors and has several advantages:

- it gives the possibility of simplifying the analogue technique when separate units for the selection and storage of the information are used;

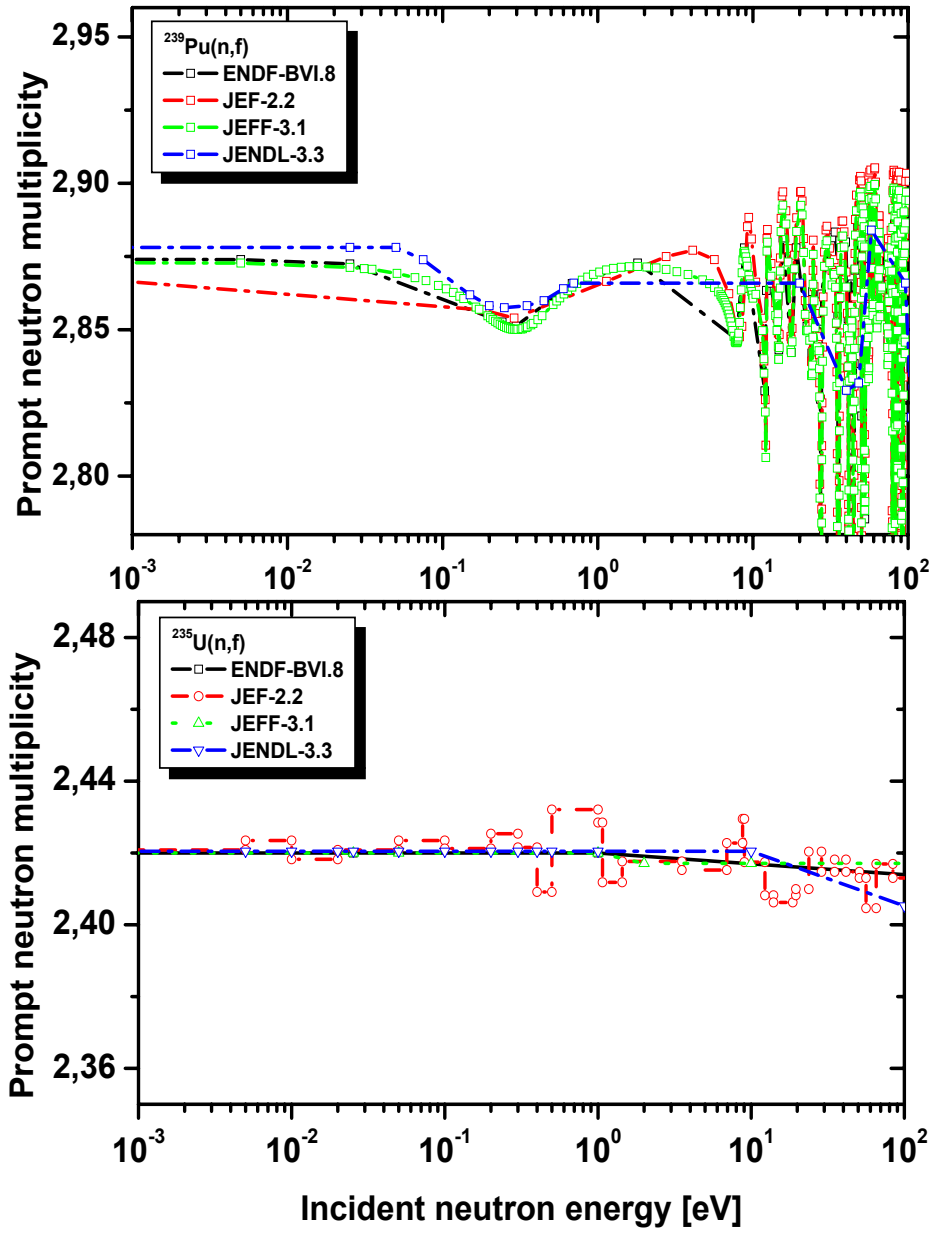

Figure 1.1: Prompt neutron multiplicity for ^{239}Pu (upper part) and ^{235}U (lower part) from different nuclear data libraries (ENDF-BVI.8, JEF-2.2, JEFF-3.1 and JENDL-3.3).

- it allows to extract the maximum amount of information contained in the signal shape. In the case of an ionization chamber this signal contains the necessary information on the particle kinetic energy, emission angle and mass;

- it is possible to modify the analysis procedure without repeating the experiment;

- it allows a proper elimination of undesirable events such as pile-up pulses. However, there is also the possibility to implement special off-line methods of the pile-up affected pulses correction. This will improve the resolution of the detection and simplify the studies of fission fragment properties for the actinides with high α-activity, such as ^{239}Pu.

The aim of this work is to show the feasibility of the experiment on ^{239}Pu(n,f) using the entirely new experimental technique. To test the digital technique and to verify the methods of off-line analysis, a ^{252}Cf source is used since here both the fission fragments and the emitted prompt neutron properties are well known.

The outline of this thesis is as follows: Chapter 2 gives an overview of the experimental tools used in this work. Chapter 3 explains the analysis procedure of the digitalized anode signal from an ionization chamber. Chapter 4 gives a detailed explanation of the analysis procedure of the digitalized signal from a neutron detector. In Chapter 5 the analysis procedure of the fission fragment events in coincidence with neutrons is given. The comparison of the results obtained using both the analogue and digital techniques is also presented.

Chapter 2

Experimental Setup

In this chapter a detailed description of the experimental tools is given. The working principles of the detectors (an ionization chamber and a neutron detector) and the acquisition system are described.

2.1 The ^{252}Cf Sample

The ^{252}Cf sample was prepared in September 2003 at the Khlopin Radium Institute, Russia. The sample had an activity of $3.5 \cdot 10^4$ Bq, a thickness of Cf $\sim$ 3.4 ng/cm^2 and was evaporated on a Ni backing layer of 250 nm thickness. The sample holder material is Al with a thickness of 0.5 mm. The active target diameter is 10 mm. The target isotopic composition as well as the fission rates of the source at the beginning (10 February 2005) and at the end (27 April 2005) of the experiment are listed in Table 2.1. The contributions from ^{249,250,251}Cf (sf) are negligible.

2.2 The Ionization Chamber

A double Frisch-grid ionization chamber (IC) was used as a fission fragment detector. As shown in [Bud87], it is possible to obtain the fragment kinetic energy, the emission angle and the fragment mass by measuring in coincidence the pulse-height of the signals from the chamber electrodes for each fragment. The

Isotope	Initial Isotopic Composition (in Atom %)	Fission rates		
		13.09.2003	10.02.2005	27.04.2005
^{249}Cf	12.17	$2.49 \cdot 10^{-7}$	$2.48 \cdot 10^{-7}$	$2.48 \cdot 10^{-7}$
^{250}Cf	15.93	1.34	1.24	1.23
^{251}Cf	7.49	$1.18 \cdot 10^{-9}$	$1.18 \cdot 10^{-9}$	$1.18 \cdot 10^{-9}$
^{252}Cf	64.41	1070	737	698
total	100.00	$\sim$ 1071	$\sim$ 738	$\sim$ 699

Table 2.1: Initial isotopic composition of the ^{252}Cf target and the fission rates at the moment of the preparation (13 Sept. 2003), beginning (10 Feb. 2005) and end (27 Apr. 2005) of the experiment.

ionization chamber covers $\sim 4\pi$ geometry. The schematic view of the detector is shown in Figure 2.1.

The detector consists of two parallel ionization chambers with Frisch grids and a common cathode. The ^{252}Cf sample is mounted at the center of the cathode. The anodes and cathode are stainless steel plates with a circular shape and with a diameter of 177.8 mm. The grids were made with a 50 μm thick wire mesh and were grounded. The chamber was operated with a gas flow of 0.1 l/min of P-10 mixture (90 % Ar + 10 % CH_4) and the pressure in the chamber was kept at $\sim$ 1050 mbar. The P-10 gas mixture was chosen for the following reasons:

- the recombination effects are less prominent in this gas mixture;
- the pulse height for this gas mixture is very little dependent on the pressure and voltages applied to the ionization chamber [Ham95];
- the pulse height defect is small [Ham95, Tov02].

The bias voltage applied to the cathode was -1700V, and +1000V for the anodes. The distances between the grid - anode and the cathode - grid are 6 mm and 30 mm, respectively. The distance cathode - grid is chosen according to the

requirement that all fission fragments should be stopped in the space between the cathode and the grid.

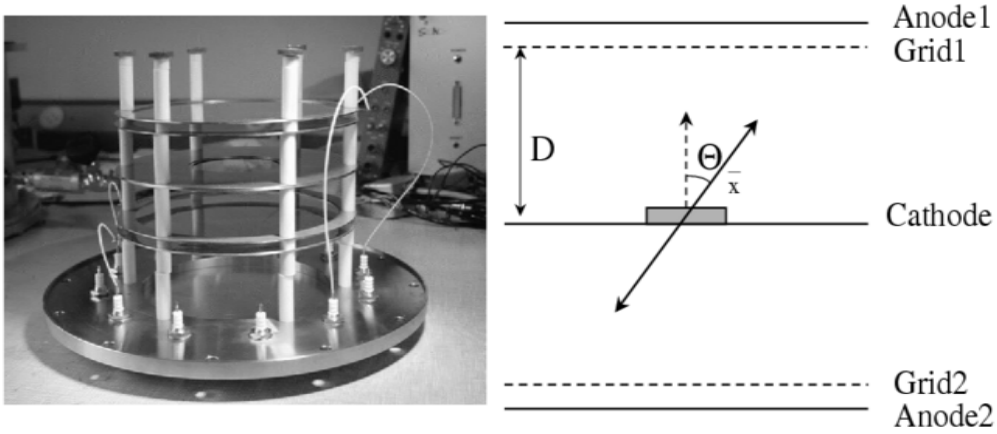

Figure 2.1: Schematic view of the ionization chamber with 2 anodes, 2 Frisch grids and common cathode.

The detection principle is based on the collection of all charges created in the volume between the cathode and the grid during the ionization of the atoms of the counting gas. Due to the electrostatic field the positive ions drift to the cathode and the free electrons move towards the anode. Several criteria should be taken into account. First of all, in order to keep the grid as transparent as possible for the electrons the following criterion is required (according to [Bun49]):

$$\frac{E_A}{E_C} \geq \frac{1+\frac{2\pi r}{g}}{1-\frac{2\pi r}{g}}, \tag{2.1}$$

where E_A and E_C are the electric fields at the anode and cathode sides, respectively; r is the radius of the grid wire (r=0.05 cm) and g is the distance between two wires of the grid (g=0.1 cm). Another criterion is the optimization of the electric field. The field should be strong enough to allow the collection of almost all charges, but weak enough not to cause secondary ionization effects.

The detailed description of the signal generation in an ionization chamber is given in [Bud87, Viv98]. In an ideal case when the electron collection is completed and, at the same time, the anode is shielded by the Frisch grid from the induction

of the moving charges in the volume between grid and cathode, the total charge induced on each of the electrodes is given by:

$$Q^{-}_{anode} = -n_0 e, \tag{2.2}$$

$$Q^{-}_{cathode} = n_0 e(1 - \frac{\overline{X}}{D}\cos\theta), \tag{2.3}$$

$$Q^{-}_{grid} = n_0 e\frac{\overline{X}}{D}\cos\theta, \tag{2.4}$$

$$Q^{-}_{sum} = Q^{-}_{anode} + Q^{-}_{grid} = -n_0 e(1 - \frac{\overline{X}}{D}\cos\theta), \tag{2.5}$$

where n_0 is the number of ion pairs created in the detector gas; $\overline{X}$ - the center-of-gravity position of the ionization track; D - the cathode-grid distance; θ - the angle between the normal of the cathode and the particle track (see Fig.2.1).

In case of the analogue technique the four signals $Q_{anode,i}$ and $Q_{sum,i}$ (where i=1,2 for backing and sample sides, respectively) are used for the analysis. The anode signals $Q_{anode,i}$ provide the information on the fission fragment kinetic energy, while the signals $Q_{sum,i}$ which are the sum of the anode and grid signals provide the information on the fragment emission angle. The time dependence of the charge induced on each electrode is shown in Fig.2.2 (from Ref.[Bud87]).

In case of the digital processing technology the information on the particle, i.e. kinetic energy and emission angle, is contained in the signal shape. This information can be extracted using the procedures of the digitalized signal analysis explained in Chapter 3.

2.3 The Neutron Detector

Scintillator detectors are widely used in nuclear physics for neutron spectroscopy since they have good n-γ discrimination capability [Smi68], high detection efficiency for fast neutrons [Kno00] and relatively good resolution [Ver68]. When

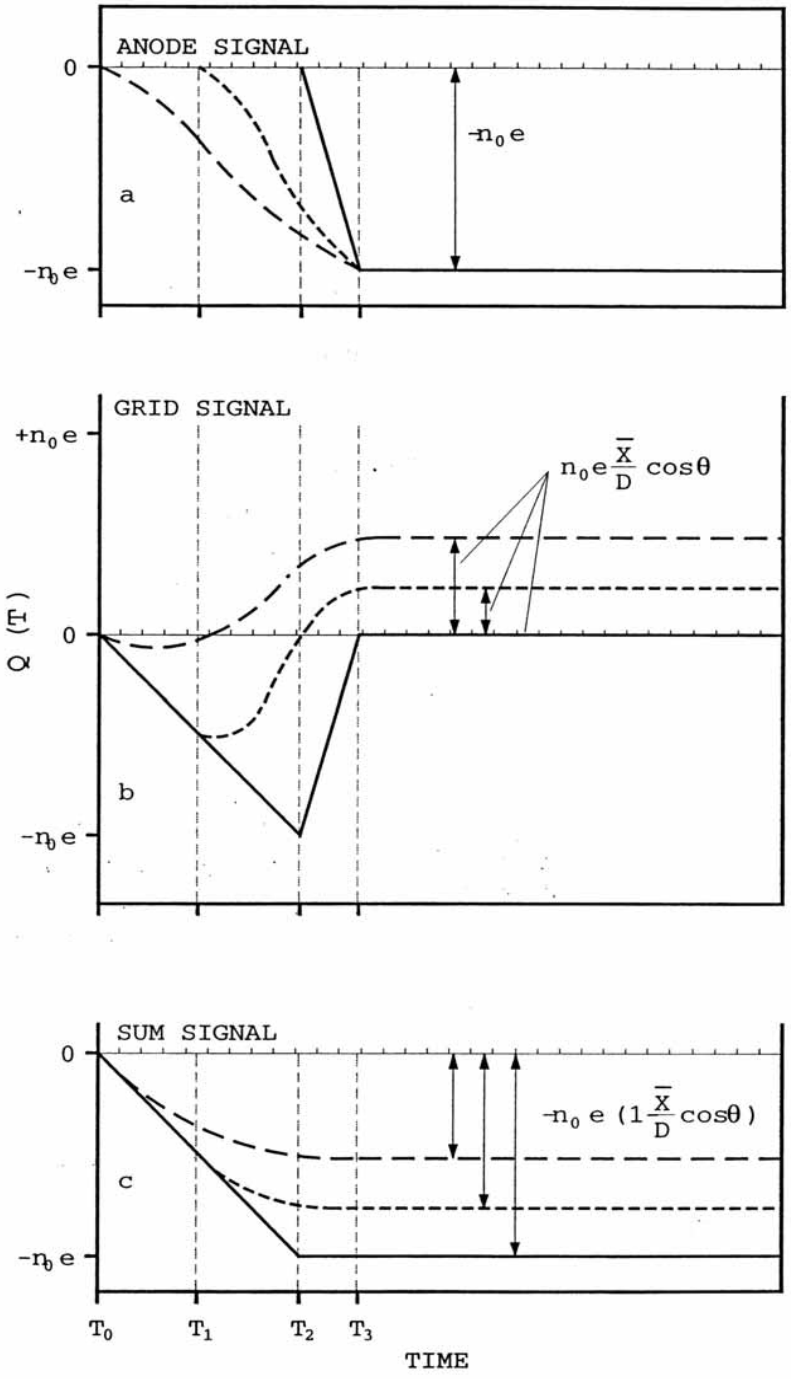

Figure 2.2: Signal outputs from the anode, grid and sum of the two signals for fission fragments emitted with an angle θ=90^0 (solid line), 45^0 (dotted line), 0^0 (dashed line).

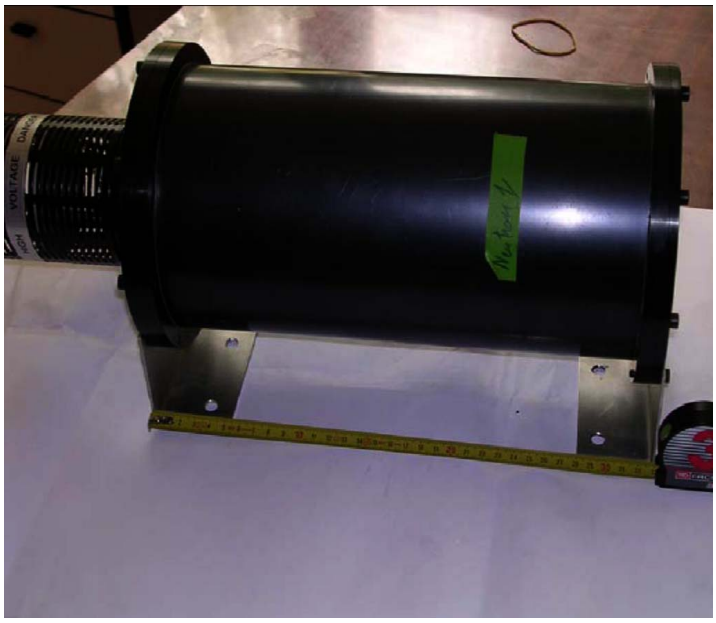

Figure 2.3: The neutron detector (liquid scintillator NE213 coupled to a Photomultiplier XP2041 inside aluminium housing).

a nuclear particle strucks certain materials it emits a small flash of light, i.e. a scintillation. These materials are known as scintillating materials. The radiation passes through the material of the detector, its atoms and molecules are excited. Deexcitation photons are then emitted. By coupling the scintillator to an amplifying device such as a Photomultiplier (PM) which converts the scintillation into electric pulse one can obtain a particle detector. The analysis of the electrical pulse gives the information concerning the incident radiation.

Several types of scintillator materials exist: organic crystals, organic liquids, plastic etc.. The liquid organic scintillator NE213 is chosen in the present experiment as it satisfies the following requirements:

- the detector should be efficient for the detection of fast neutrons;

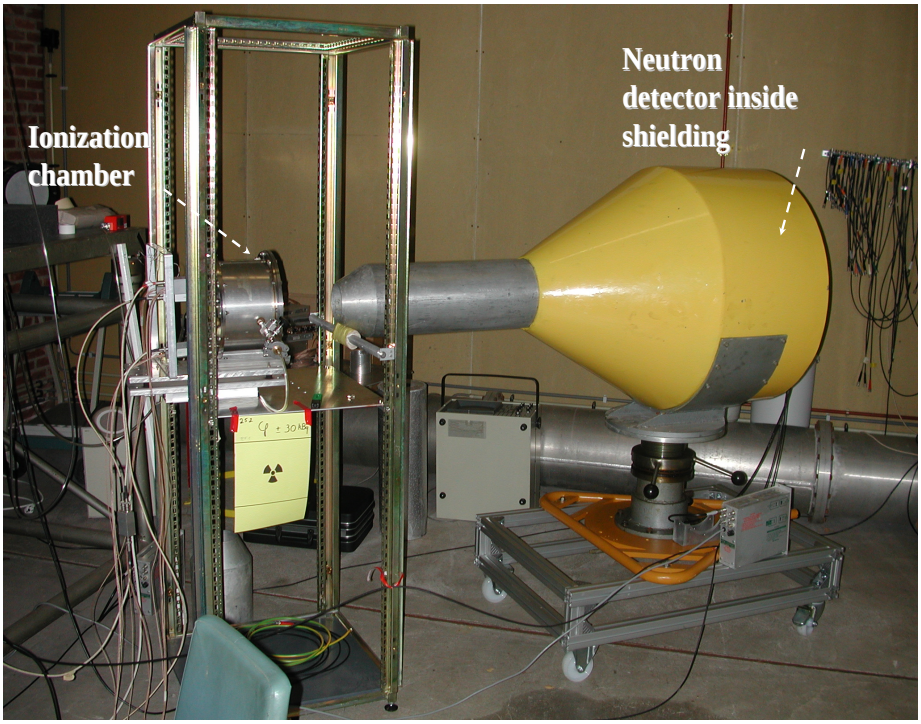

Figure 2.4: Experimental set-up with the ionization chamber and well collimated neutron detector inside shielding.

- the detector should exhibit a good n - γ discrimination.

In the present experiment, a 15 cm diameter and 6 cm thick NE213 liquid scintillator coupled to a 10 cm diameter XP2041 photomultiplier was used (Fig.2.3), on loan from the CEN Bordeaux Gradignan. The detector was placed in a polyethylene shielding at a distance of 1.47 m from the IC (see Fig.2.4). The solid angle covered by the neutron detector is 0.064 %. The anode signal of the PM was used in the Time-of-Flight (TOF) technique and for the identification and discrimination between γ-rays and prompt neutrons by means of Pulse Shape analysis.

2.4 Electronics and Data Acquisition

2.4.1 Data Acquisition Software

The data acquisition is based on 2 synchronized waveform digitizers (WFD) from FAST-ComTec company [Fast]. The used waveform digitizers are fast 12 bit analogue/digital converter boards which are PCI bus compatible. They are able to work in different sample rates and numbers of input channels. In the present work one WFD1 (one input channel, 200 MHz sampling frequency, i.e. 5 ns/channel) was used to record the sum of the anode signal of the neutron detector with the cathode signal of the ionization chamber. At the same time the second WFD2 (2 input channels, 100 MHz sampling frequency, i.e. 10 ns/channel) was used to record the fission fragment waveforms. The cathode signal from the IC gives the start-time (fission) while the anode signal from the neutron detector gives the stop-time (neutron or γ-rays). Both time stamps are used for the determination of the neutron energy using the TOF technique. The digitalized signals were stored on the hard disk event by event.

Data storing was carried out by a software based on a LabView programming environment. It is a graphical development environment designed by National Instruments Laboratory [NILab] and adjusted for our purposes by FAST-ComTec [Fast]. This software allows us to interface with electronical digitalized signals, to store the experimental data on a disk as well as to apply a simple data analysis for meaningful information.

Fig.2.5 shows the layout of the LabView software. Here, the 4 upper windows visualize the signals that arrive at the first WFD and the 4 bottom windows are reserved for the second WFD. During the experiment, the first and third display rows show the digitalized signals while the other windows give the simple pulse height analysis (second and fourth rows). In our experiment only one upper window was used for WFD1 (1 channel available) and 4 bottom windows were used for WFD2 in order to display the fission fragment events. All experimental data are stored on the hard disk of a fast PC system.

The Wave Form Digitizers can work in external or internal trigger modes. The description of each mode will be given in the following paragraphs, as well

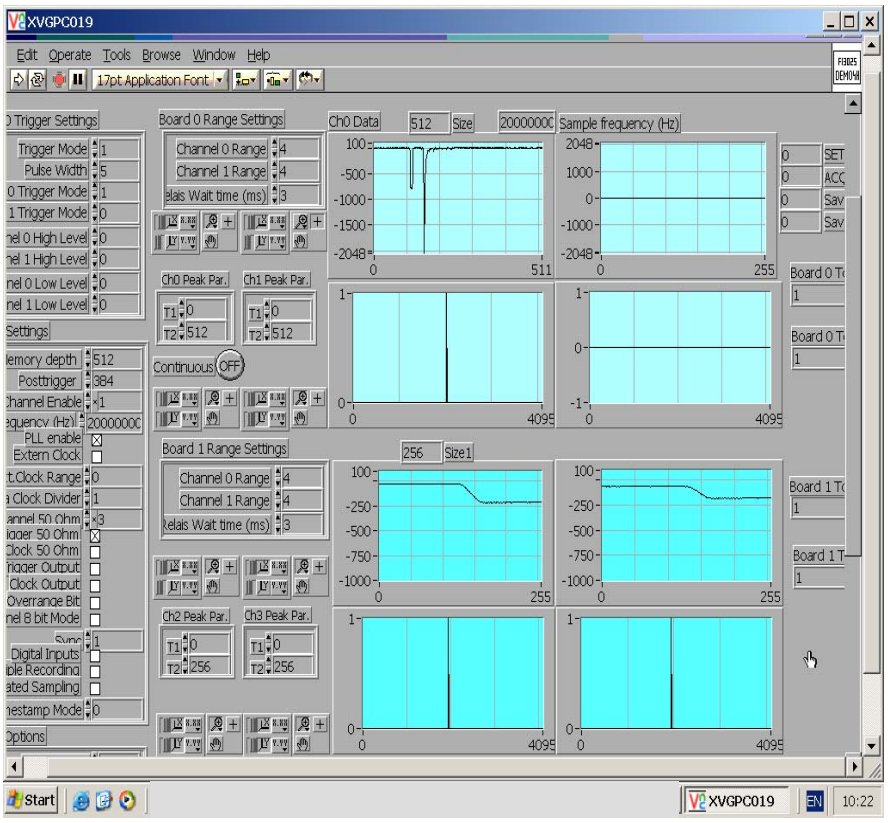

Figure 2.5: Schematic layout of the LabView programming environment. 4 upper windows are reserved for the signals arriving to WFD1; 4 bottom windows used for the signals arriving to WFD2.

as the choice of the optimized experimental set-up for the present work.

2.4.2 External Trigger Mode

The experiment was planned to be done in 2 separate steps: to measure the fission fragments in and without the coincidence with the emitted prompt neutrons. In both measurements WFDs worked in the external trigger mode. The external trigger for WFD should be a TTL signal. This signal was created in different ways for both experiments.

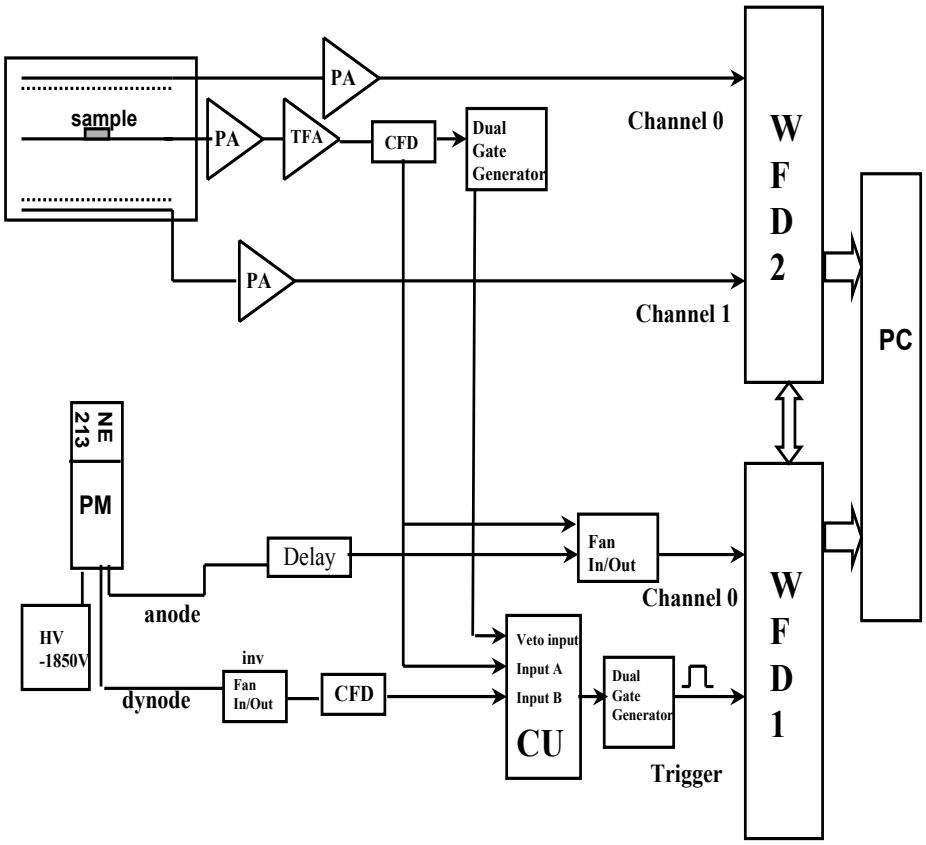

Figure 2.6: Schematic layout of the measurement with external trigger of fission fragments in coincidence with emitted prompt neutrons (2-3 trigger events/sec). PA - Preamplifier; TFA - Timing Filter Amplifier; CFD - Constant Fraction Discriminator; HV - High Voltage; CU - Coincidence Unit; WFD - Wave Form Digitizer; PC - Computer.

1st step: measurement of the fission fragments in coincidence with the emitted prompt neutrons.

Fig.2.6 presents the experimental diagram for the measurements of the fission fragments and emitted prompt neutrons in coincidence. Both WFDs were set to work in the external trigger mode, i.e. there is a signal created externally and

then sent to the trigger input of the WFD1. The WFD1 was set to be a "master" board while the WFD2 was set as a "slave" board. As soon as the work of both digitizers is synchronized, it is sufficient to send the trigger signal to only one digitizer marked as "master".

The dynode signal from the neutron detector and the cathode signal from the IC were used to create the trigger signal for both WFDs. First of all, the dynode signal was inverted in the linear Fan In/Out [LeCroy] and then was sent to the Constant Fraction Discriminator (CFD) [ORTEC]. One output signal of the CFD was fed to the "input B" of the coincidence unit (CU). The cathode signal from the IC after amplification by the charge-sensitive Preamplifier (PA) and by the Timing Filter Amplifier (TFA) was fed to the CFD input. One output signal of CFD was fed to the "input A" of the CU while the second output signal of CFD was sent to a Dual Gate Generator (DGG) where the coincidence window was created. This coincidence window was sent to the "Veto input" of the CU. When both the cathode signal of the chamber and the dynode signal of NE213 arrive within the coincidence window, the CU creates a signal that is then fed to the DGG. The TTL signal from the dual gate generator was used as the external trigger signal. Both anode signals from the IC were amplified by the charge-sensitive PA [Bon03] and were sent to the 2 channels of the WFD2. The cathode signal from the IC and the delayed signal from the NE213 was sent to channel 0 of the WFD1 through Fan In/Out.

2nd step: measurement of the fission fragments without coincidence.

The experimental set-up for the measurement of the fission fragment properties without the coincidence with emitted prompt neutrons is presented in Fig.2.7. For this experiment the external trigger signal was created only from the cathode signal of the IC (timing output of the preamplifier). This set-up is similar to the one used in the analogue experiments and can be used for the measurements of fission fragment properties.

Encountered problems with the external trigger mode.

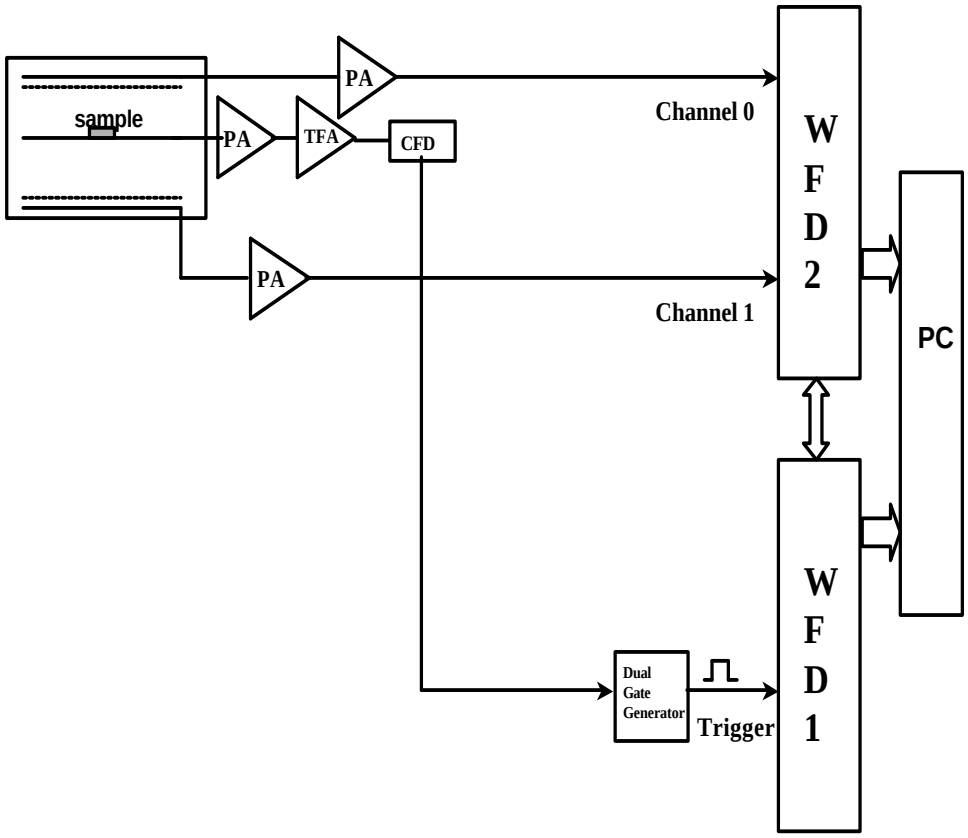

Figure 2.7: Schematic layout of the measurement with external trigger of the fission fragments without the coincidence with emitted prompt neutrons ($\sim$ 800 trigger events/sec). PA - Preamplifier; TFA - Timing Filter Amplifier; CFD - Constant Fraction Discriminator; DGG - Dual Gate Generator; WFD - Wave Form Digitizer; PC - Computer.

The dead time of the whole system should be the same for the measurements of the fission fragments (FF) with or without coincidence with the emitted prompt neutrons. The dead time is the finite time required by the detector to process an event which is usually related to the duration of the pulse. The dead time determination is explained below (see section 2.5.2). During the test measurements using the set-ups with external trigger created in different ways the number of the trigger signals sent to the WFD input was different for each experiment (with and without the coincidence between FF and neutrons). Unfortunately, the num-

ber of events acquired by LabView was different from the number of the trigger events sent to the WFD. In addition, the dead times for the different number of the trigger events were not equal. The problem of the different dead time must be avoided for the experiments dedicated to the neutron multiplicity determination. One way to solve this problem is to use the internal trigger mode for the WFDs triggering.

2.4.3 Internal Trigger Mode

The experimental set-up where both waveform digitizers work in the internal trigger mode satisfies all requirements and can help to solve the problem of the different dead time. Using this experimental set-up it is possible to measure simultaneously the fission fragment in coincidence with the emitted prompt neutrons and, in the same experiment, measure the fission fragments without the coincidence with emitted prompt neutrons.

The block diagram of the electronics used with internal trigger mode is presented in Fig.2.8. The signals from both anodes of the IC were fed into the charge-sensitive PA. Then the output signals from the preamplifiers were fed directly into 2 channels of the WFD2 running with the sampling frequency of 100 MHz. The cathode signal of the IC was fed into the same type of PA; then the PA output signal was sent to the Timing Filter Amplifier (TFA) and to the Constant Fraction Discriminator (CFD). The trigger level of the CFD was set above the noise level. The output signal of the CFD has a rectangular shape and is used as the trigger after the summation in the Linear Fan In/Out with the detector pulse. This sum is sent to the channel 0 of the WFD1 running with the frequency of 200 MHz. This board is set as a "master" board for the trigger and timing synchronization, while the second WFD was set as a "slave" board. In this case both boards are triggered by any signal arriving into the channel 0 of the WFD1 (cathode signal plus detector pulse or only detector pulse). The parameters of the internal trigger (posttrigger channels, negative edge, voltage limits within the signal) were set in the LabView software. If the input signal corresponds to the requirements for the internal trigger, it triggers both WFDs and the acquisition starts. The cathode signal from the IC indicates the "start" of the fission and the

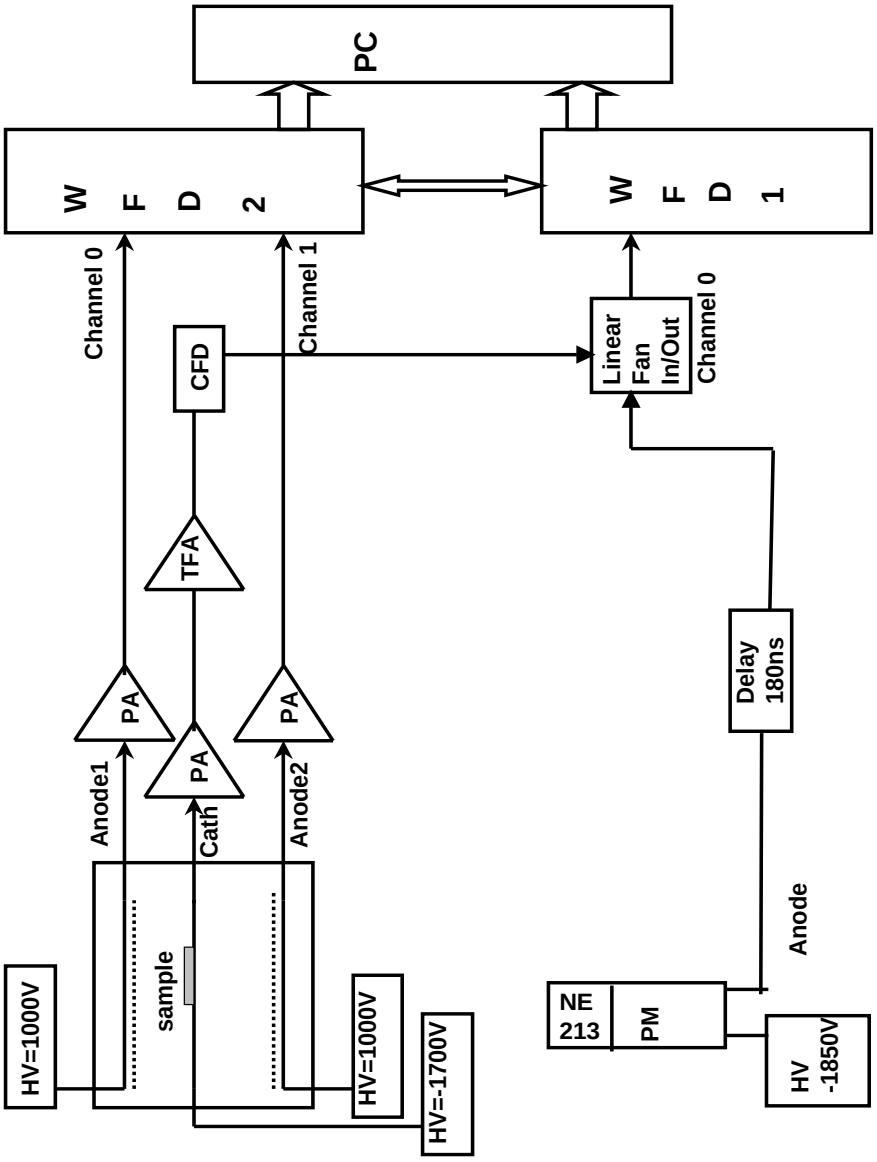

Figure 2.8: Schematic view of the experimental set-up with internal trigger. HV - High Voltage Supply; PA- Preamplifier; TFA - Timing Filter Amplifier; CFD - Constant Fraction Discriminator; PM - Photomultiplier; WFD - Wave Form Digitizer

detector pulse gives the "stop" position needed for the TOF spectrum determination. The procedure of the determination of "start" and "stop" positions for the TOF spectrum will be explained in the Chapter 4.

2.5 Measurements and Data Sorting

2.5.1 The Experiment

The experiment ran for 53.36 days (i.e. 1 280,68 h). The acquired data rate per day was $\sim$ 40 Gb. The data were stored on a fast removable hard disk with a 120 Gb capacity. When the disk was full, the experiment was stopped, then the disk replaced and the experiment restarted. The total amount of data was reduced in order to be able to store all data on the available disk space. The total number of events acquired with the LabView software was $\sim 1.1 \cdot 10^9$ events. These events include:

- the fission fragment events (cathode and 2 FF) plus the neutron detector pulse;
- the fission fragment events (cathode and 2 FF) without coincidence with the neutron detector pulse;
- the cathode pulse and one of the fission fragments with or without the pulse from NE213;
- the events containing only the neutron detector pulse.

During the experiment the LabView software counted the events saved on the disk. At the end of the experiment we had 21 series. Every series corresponds to the measurements during several days before the change of the full disk. After a simple preliminary analysis of the experimental data, series by series, it was found that the data of one series were damaged. These data were removed from the analysis. So, the actual acquisition time is 1 193,68 hours.

2.5.2 Dead Time Determination

As mentioned above, the dead time is the time required by the detector to process an event and is insensitive to the next one. When calculating the effect of dead time, the entire detection system must be taken into account. It was seen that the dead time is very high which is mainly due to the too slow LabView software.

After the digitalization of the input pulses, the information should be transferred to the memory of the computer and then stored on the hard disk. This process takes time and therefore reduces the counting rate. In order to evaluate the dead time value of the LabView processing an external pulse counter was installed. The cathode signal of the ionization chamber and the signal from the neutron detector were fed into the inputs of the external counter. Summing the average counting rate (neutron + γ) from the NE213 (161 counts/sec) and from the ionization chamber (773.79 counts/sec) and comparing the obtained value to the average counting rate given by the internal LabView counter (230.49 counts/sec) one can determine the dead time. This value is equal to 75.3 %

One can see that the dead time value is very high. But due to the choice of the internal trigger mode and the possibility to acquire in a single experimental run the fission fragment events in coincidence with neutrons as well as without coincidence, the value of the dead time is the same for all type of events. So, this high value does not affect too negatively the present work.

2.5.3 Data Sorting

As mentioned earlier, during the measurement, a big amount of data was acquired on the hard disk (about 40 Gb per day). The amount of data had to be reduced without loosing any information. For this purpose a special software using a Fortran code was developed. This software separated all experimental data, event by event, into different files where data were stored in the binary format:

- coinc.nnn - all coincidence events, i.e. fission fragment events in coincidence with prompt neutrons and γ were stored in the same files;

- fragm.nnn - fission fragment events, i.e. there are only the signals from the cathode and both anodes of the IC. As the amount of the data was big, only every 30th event was stored;
- neutr.nnn - events where both WFDs were triggered by the signal from the NE213. In that case, the signals from the IC (cathode and 2 anodes) were absent; there are only the signals from the neutron detector. In order to reduce the amount of the data only every 10th event was recorded;
- oneff.nnn - several fission fragment events were reported from only one anode signal.

2.5.4 General Remark

Comparing the digital and the analogue techniques one can say that the digital technique is about 150 times more demanding in terms of data storage space. For example, let us consider one event where 2 fission fragments are detected in coincidence with one neutron. In the analogue technique for the storage of this event about 14 bytes of disk space are needed: the information 2 anodes + 2 grids + 1 cathode + neutron (Q_{fast} and Q_{slow}) => $7 \cdot 16$ bit = 112 bit = 14 bytes. While in the digital technique it is necessary to have about 2 kbytes per event: 2 FF $\cdot$ 256 channels $\cdot$ 2 bytes + 1 neutron $\cdot$ 512 channels $\cdot$ 2 bytes = 2 kb. So, the digital technique demands more storage space and is time consuming (due to the high dead time). However, this technique allows a very clean and reliable determination of the fission fragment and prompt neutron characteristics.

A complete analysis of the experimental data was done off-line. A special software was developed using the Fortran computer language in order to extract all necessary information such as the neutron energy, angular, mass and kinetic energy distributions of the fission fragments. The following chapters explain in detail the procedures of the off-line analysis of these data. The results of the analysis are presented as well as a comparison with the data obtained by the use of the analogue technique.

Chapter 3

Fission Fragment Analysis

In this section a detailed description of the analysis of the fission fragments without the coincidence with neutrons will be done. The off-line analysis of the fission fragment events is done with the help of several programs which were initially developed by Khriatchkov [Khr99], and were improved for the present work.

The programs operate with the anode pulse (see Fig.3.1). In this figure the cathode signal of the IC recorded by the WFD1 (5 ns/channel) can be seen together with both signals from the anodes of the IC recorded by the WFD2 (10 ns/channel). The cathode signal indicates the point corresponding to the beginning of the linear increase of the signal due to the grid inefficiency (that will be discussed in section 3.1.2). The positions of the anode signal maxima correspond to the moment of the arrival of the last electrons to the anode. This position is the same for all anode pulses due to the definite distance between cathode and anode in the ionization chamber. The time T_0 is the time needed for the electrons to go from the cathode to the anode (T_0=1.03 μs).

The programs determine the anode Pulse Height which is proportional to the kinetic energy; the center-of-gravity of the ionization track from the slope of the anode pulse from which we can infer the fission fragment emission angle. Hence, it is important to apply several corrections to the raw pulses such as:

- base line fluctuations;
- calibration of the anode pulses;
- correction for the grid inefficiency;

- correction for the preamplifier discharge ("ballistic" effect);
- search for the pile-up events and criteria for their rejection.

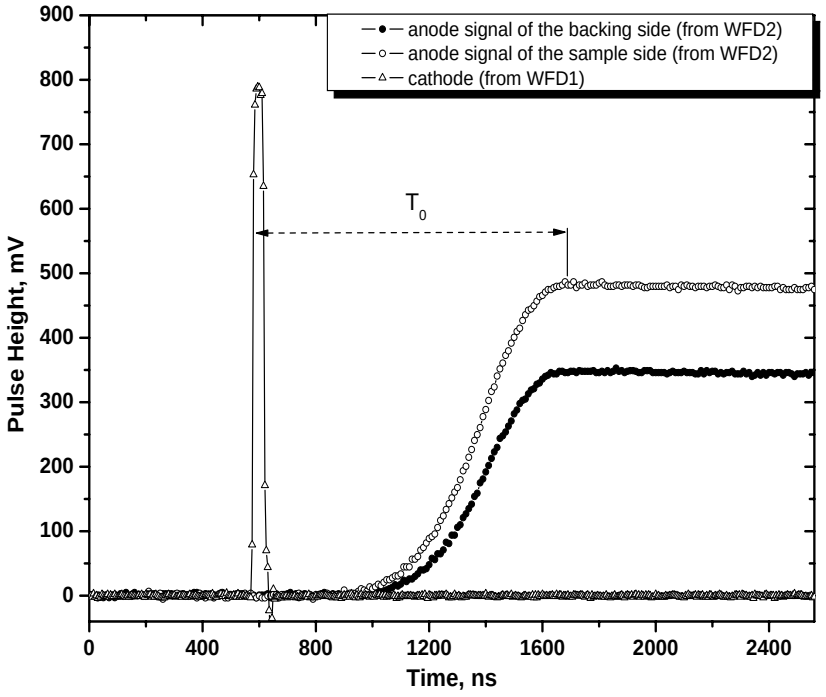

Figure 3.1: The typical example of the cathode and anode waveforms (backing and sample sides). The time T_0 is the time needed for the electrons to go from the cathode to the anode.

Then the programs apply the obtained correction parameters to the anode pulse and determine the following fission fragment characteristics:

- the ionization track center-of-gravity and pulse height distributions;
- the fission fragment angular distributions. The fission fragment emission angle with respect to the normal to the cathode can be determined from the slope of the anode signals. A typical example is given in Fig.3.2, where 2 fission fragments with the same pulse height but emitted at different angles are presented.

- the fission fragment energy loss in the sample and backing material of the target;
- the kinetic energy and mass distributions of the fission fragments.

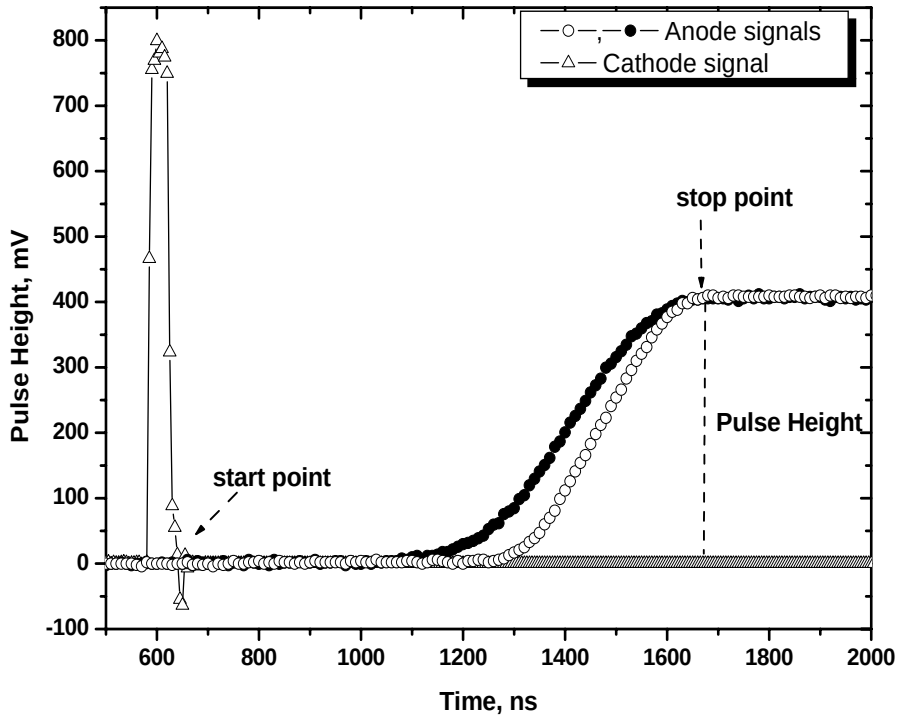

Figure 3.2: An example of the signals induced on the anodes by fission fragments with the same energy (i.e. the same pulse height) but different emission angles (i.e. different slope).

3.1 Data Analysis Procedure

3.1.1 Base Line Shift Correction and Relative Calibration

In all programs the first applied correction is the correction for the base line fluctuation which is caused by the preamplifier (see Fig.3.3).

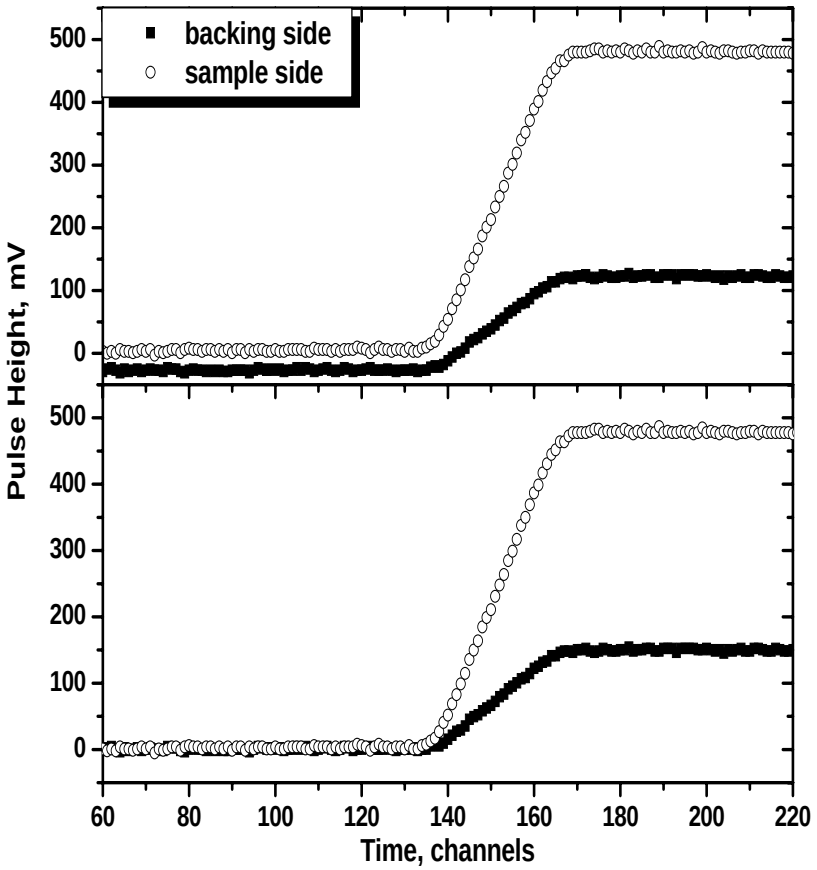

Figure 3.3: The base line correction on the anode signals. The upper part shows the raw anode pulses while the lower part presents the same pulses after the base line shift correction.

The next correction is the relative calibration of the anode pulse height due to the different amplification of the Preamplifiers (PA). The amplitude calibration is performed by connecting each preamplifier to the anodes and to a pulse generator. The voltage from a generator was fed into the test input of PA. The output of the preamplifiers was transmitted to the oscilloscope. For each preamplifier the following relation was obtained:

$$signal_i(Volt) = a_i PH_i(channels) + b_i \tag{3.1}$$

where i = 1,2 stand for backing and sample, respectively.

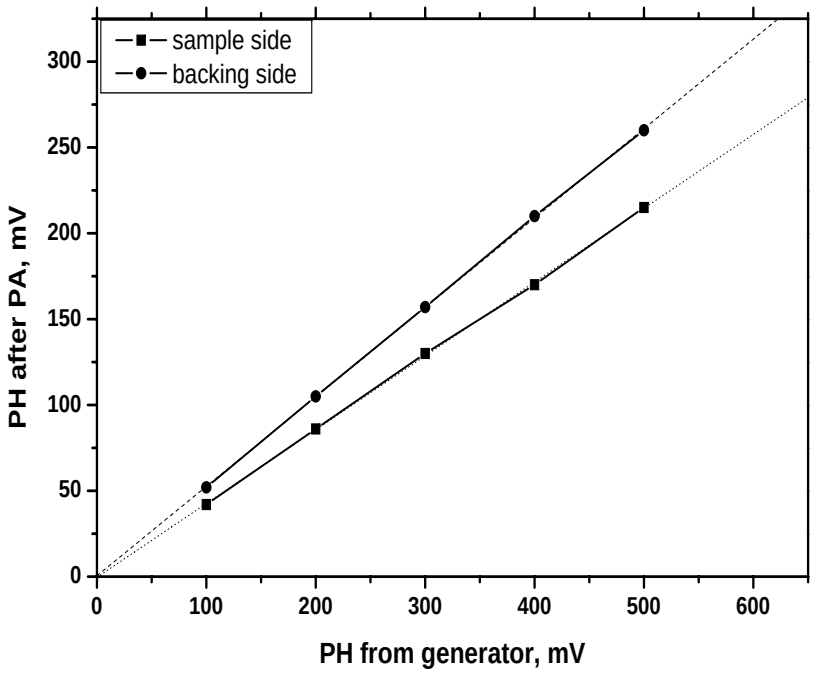

Figure 3.4: The relative calibration of anode pulses due to the different amplification of the preamplifiers.

Finally, using the parameters of the linear fits (see Fig.3.4) the raw data are corrected via:

$$PH_i(channels) = \frac{signal_i(Volt) - b_i}{a_i} \tag{3.2}$$

The next steps are the correction of the anode pulse for the grid inefficiency and for the preamplifier discharge in order to determine the real pulse height of the anode signal.

3.1.2 Pulse Height Determination

3.1.2.1 Grid Inefficiency

The Frisch grid is used to remove the dependence of the pulse amplitude on the position of the interaction. The Frisch grid is made to be as transparent as possible to electrons. Since each electron passes through the same potential difference between grid and anode and contributes equally to the signal pulse, the pulse height is now independent of the position of formation of the original ion pairs. A Frisch grid should provide a sufficient shielding of the anode during the time when electrons are moving from the cathode to the grid. Unfortunately, the grid does not shield perfectly and hence a fraction of the charge is already induced on the anode during the passage between the cathode and the grid.

According to the Bunemann formula [Bun49], it is possible to estimate the grid inefficiency:

$$\sigma = \frac{l}{l+p}, \tag{3.3}$$

where

$$l = \frac{d}{2\pi}(\frac{\rho^2}{4} - ln\rho), \tag{3.4}$$

$$\rho = \frac{2\pi r}{d}. \tag{3.5}$$

Here p is the anode-grid distance (6 mm); r is the grid wires radius (50 μm); d is the distance between the grid wires (0.1 cm). The grid inefficiency, calculated by these formulas, was found to be 3 %.

As shown in Ref.[Bun49], the Bunemann formula can be used only for the parallel wire grid. Since, in the present work, a meshed wire grid was used, the Bunemann formula could not be used to determine the grid inefficiency. One of the important advantages of the signal digitalization is the possibility to find the value of the grid inefficiency for the meshed grid directly from the anode signal.

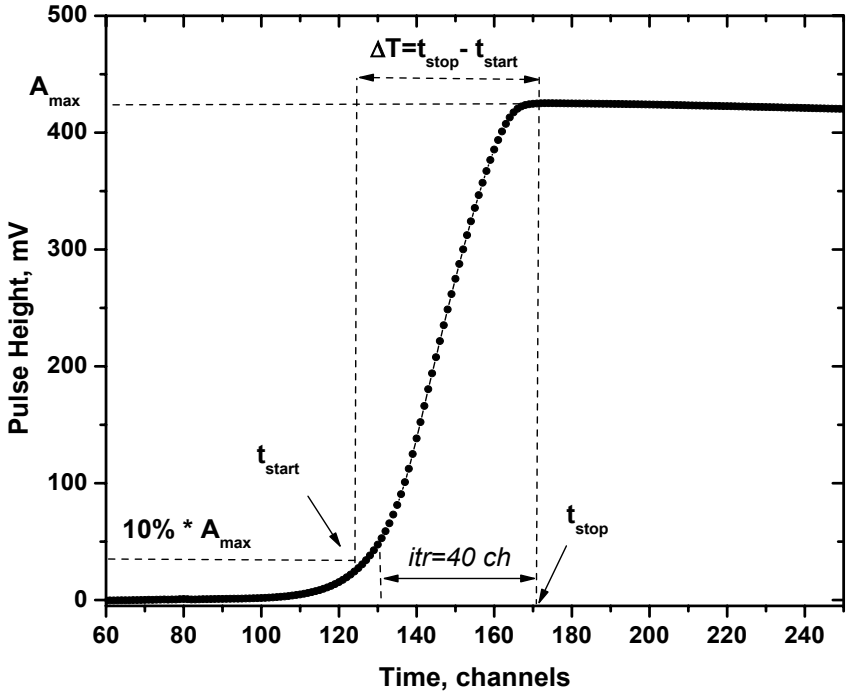

Figure 3.5: Determination of the t_{start} and t_{stop}. t_{start} is determined as the position of the 10% of the signal maximum (A_{max}). In this example, the signal was not taken into account for the average signal determination since $\Delta T > itr$.

The following procedure was applied. The program checks all anode signals corrected for the base line shift, event by event, and determines the beginning (t_{start}) and the end (t_{stop}) of the anode signal formation. For every anode signal, t_{start} was determined as the position of the 10 % from the signal maximum (see Fig.3.5). t_{stop} corresponds to the position of the signal maximum (A_{max}), i.e. the time when the last electrons arrive at the anode. Then the value ΔT=t_{start} - t_{stop} is compared to the arbitrary chosen value *itr* (40 channels) . This parameter is chosen to be small enough in order to select the events emitted with cos$\theta \sim 1$ (θ being the angle of the fission fragment emission with respect to the normal of the cathode (see Fig.2.1)). These fragments have little energy loss in the target material, and the grid inefficiency can be determined properly. As the result of

the program operation two ASCII files were created. They contain the average anode signals for 2 parts of the IC, i.e. sample and backing sides. These average signals were obtained from all anode pulses which satisfy the condition: $\Delta T \leq itr$. All pulses were summed and then averaged over the number of pulses in this sum.

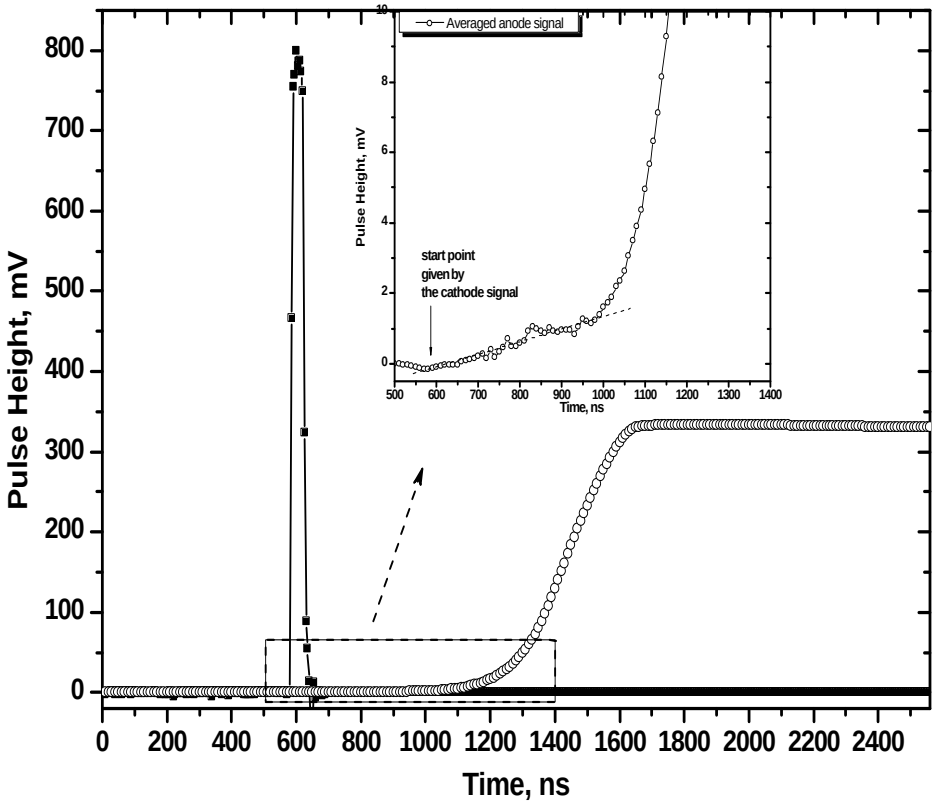

Figure 3.6: The average anode pulse and the linear fit of the linear part of the signal (zoomed figure) used for the determination of the grid inefficiency.

An example of the linear increase (and the linear fit) of this region is shown in Fig.3.6. As it was mentioned before, due to the grid inefficiency a fraction of the charge is induced on the anode during the passage in the space between cathode and grid. This behavior can be seen in Fig.3.6 where the anode signal starts to increase right after the cathode signal. So, this linear increase region corresponds

to the grid inefficiency. A linear fit y=a+b·t of this part of the signal can be done. The parameters of the fit permit to determine the true start of the signal (y=0):

$$t_{start} = -\frac{a}{b}, \tag{3.6}$$

and the grid inefficiency σ:

$$\sigma = \frac{y_{stop}}{A_{max} - y_{stop}} = \frac{a + b \cdot t_{stop}}{A_{max} - (a + b \cdot t_{stop})}, \tag{3.7}$$

where A_{max} is the maximum amplitude of the averaged anode signal.

The true start (t_{start}) is the same as the start indicated by the presence of the cathode signal (see Fig.3.2). Hence, even in a case where the cathode signal is not saved together with the anode pulses, the above described procedure permits to determine precisely the start of the fission process.

The grid inefficiency was found to be (1.1 ± 0.3) % for both grids (sample and backing sides). The uncertainty on the grid inefficiency is due to the choice of the channels for the linear fit, the linear fit itself and the choice of the value of *itr*. The value of the grid inefficiency is lower than the value obtained from the Bunemann formula. It can be explained from the difference of the grid geometry for the parallel wire and meshed grids. Meshed grids are designed to provide a better shielding of the anodes.

3.1.2.2 "Ballistic" Effect

In the next step the anode signal should be corrected for the preamplifier discharge, so called "ballistic effect" (see Fig.3.7a). In this figure one can see the fluctuations of the anode pulse. Due to these fluctuations it is impossible to determine the true stop of the signal (the time of the arrival of the last electrons to the anode) and the true pulse height of the anode pulse. One can also see the exponential decrease of the signal due to the preamplifier discharge. So, the signal should be corrected for the "ballistic" effect. That correction allows us to

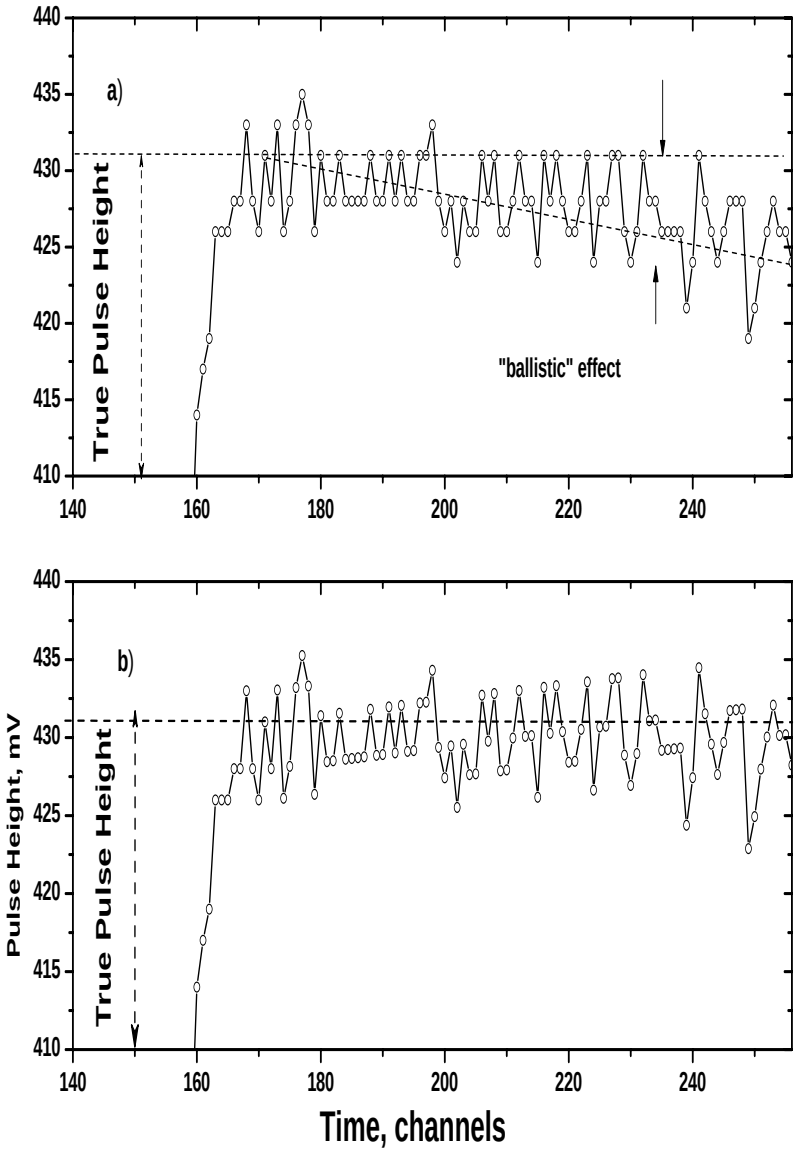

Figure 3.7: Example of the exponential decrease of the digitized anode signal due to the preamplifier discharge (a), corrected for the "ballistic" effect anode pulse (b) and true pulse height found as the average value. The WFD channel width is 10 ns/channel.

reconstruct the true anode Pulse Height that will be then used for the fragment energy determination.

First of all, it is necessary to determine the position of the complete arrival of all electrons to the anode and the height of the signal maximum at this point. It can be done by the least square method. These parameters are needed for the exponential fit of the signal part starting from the position of the last arrival of all electrons (t_{stop}) down to the end of the signal (end of the channel scale):

$$Y = A_{max} \cdot exp(\frac{-(t - t_{stop})}{\tau}). \tag{3.8}$$

The obtained values for the preamplifier discharge τ are 84.6 μs and 32.2 μs for the preamplifiers of the backing and sample sides, respectively. An example of the correction for preamplifier discharge is displayed in Fig.3.7b. The true pulse height was found as the average value over all signals starting from t_{stop} till the end of the anode pulse corrected for the "ballistic" effect. The values τ, t_{stop} are then applied to every anode pulse in the next steps of the analysis. Note that the value of the preamplifier discharge is the same for every anode signal of the chosen side of the IC (backing or sample) as this value is a characteristic of the used Preamplifiers.

3.1.3 Rejection of "Pile-up" Events

In recent years techniques for rejecting pile-up events have attracted the interest of various scientists. First, a pulse pile-up rejection technique has been developed by Budtz-Jørgensen and presented in [Bud87]. This technique reduces pulse pile-up by more than a factor 30. Then, a novel scheme has been developed by Demattè ([Dem98],[Dem02]) that leads a rejection rate of 90 % of pile-up affected pulses from a plutonium sample with an activity of $\sim$ 1 MBq. The pile-up rejection is necessary in order to avoid wrong determination of the pulse height.

The digitalization gives the opportunity not only to simplify the experimental set-up, but also to save the fission fragment signals contaminated by the pile-up events in order to analyse them off-line. In this work such events were rejected

in the off-line analysis but it is possible to develop and to apply a special off-line procedure to correct the signal for the pile-up without rejecting this anode pulse from the whole analysis. It is very useful in particular when we use a very high α-activity sample.

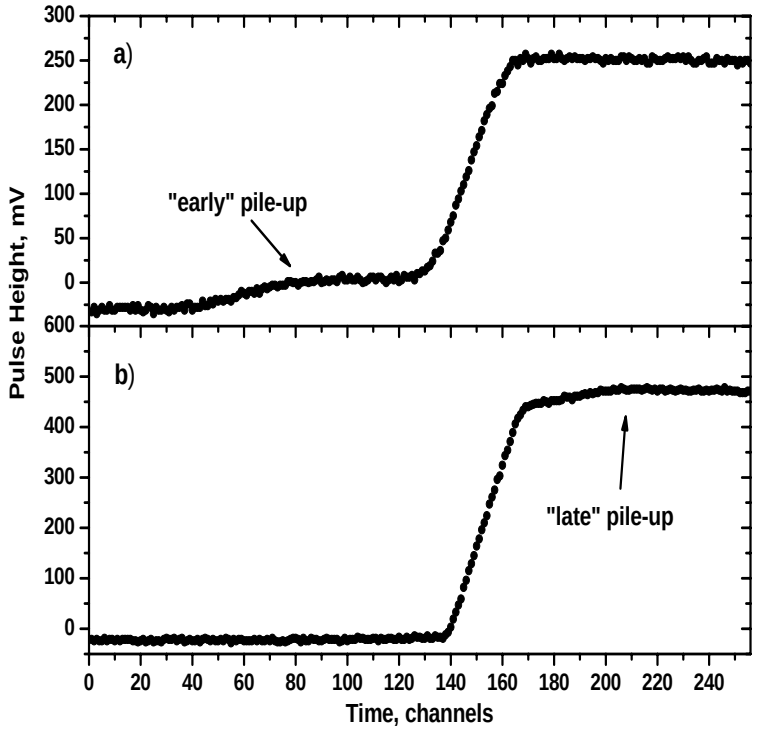

Figure 3.8: Examples of the fission fragment events with "early" (a) and "late" (b) pile-up.

When an α-particle occurs before a fission fragment reaches the anode, one can speak about "early" pile-up (see Fig.3.8a). A "late" pile-up corresponds to α-particle reaching the anode after the fission fragment (see Fig.3.8b).

The following procedure can be applied for the search of such events and their rejection. The program is carrying out a complex analysis of the initial signal (no correction for the base-line fluctuations, grid inefficiency and the preamplifier discharge have been done). This analysis consists in a search for the extra peaks, matching the initial signal with the zero line as well as matching the position of an exponential decay for every event with a model signal. This operation is

done event by event. The model signal is the signal created from the information found in the previous steps of the analysis, i.e. position of the "start" and "stop" of the signal, grid inefficiency and the exponential decay. The signal with pile-up is marked as "bad" and is rejected from further processing.

3.1.4 Center-of-Gravity and Angular Distributions

The knowledge of the center-of-gravity of the ionization track permits the determination of the fragment emission angle. In general, this quantity is a function of the fragment kinetic energy E, mass A and charge Z, i.e. $\overline{X}$(E,A,Z):

$$\overline{X} = \frac{1}{n_0} \int_0^R x\rho(x)dx, \tag{3.9}$$

where n_0 is the number of ion pairs created in the detector gas, $\rho(x)$ is the ionization density along the track, R is the particle range, x is the distance from the origin of the track.

In the case of the analogue technique the center-of-gravity is determined from the sum of the grid and the anode signals expressed as (see Ref.[Bud87]):

$$P_{sum} = -n_0 e \cdot (1 - \frac{\overline{X}}{D} cos\theta), \tag{3.10}$$

where D is the cathode - grid distance.

The $\frac{\overline{X}}{D} cos\theta$ values inferred from the knowledge of the P_{sum} and P_{anode} are stored versus the anode pulse height into a 2-dimensional matrix. Then the cosine of the emission angle can be calculated as:

$$cos\theta = \frac{P_{anode}^{corr} - P_{sum}}{P_{anode}^{corr} \cdot \frac{\overline{X}}{D}}, \tag{3.11}$$

where P_{anode}^{corr} is the anode pulse height corrected for grid inefficiency:

$$P_{anode}^{corr} = P_{anode} - \sigma \cdot P_{sum}, \tag{3.12}$$

and where the $\frac{\overline{X}}{D}$ values are determined as the length of the 2-dimensional matrix center-of-gravity versus the anode pulse height.

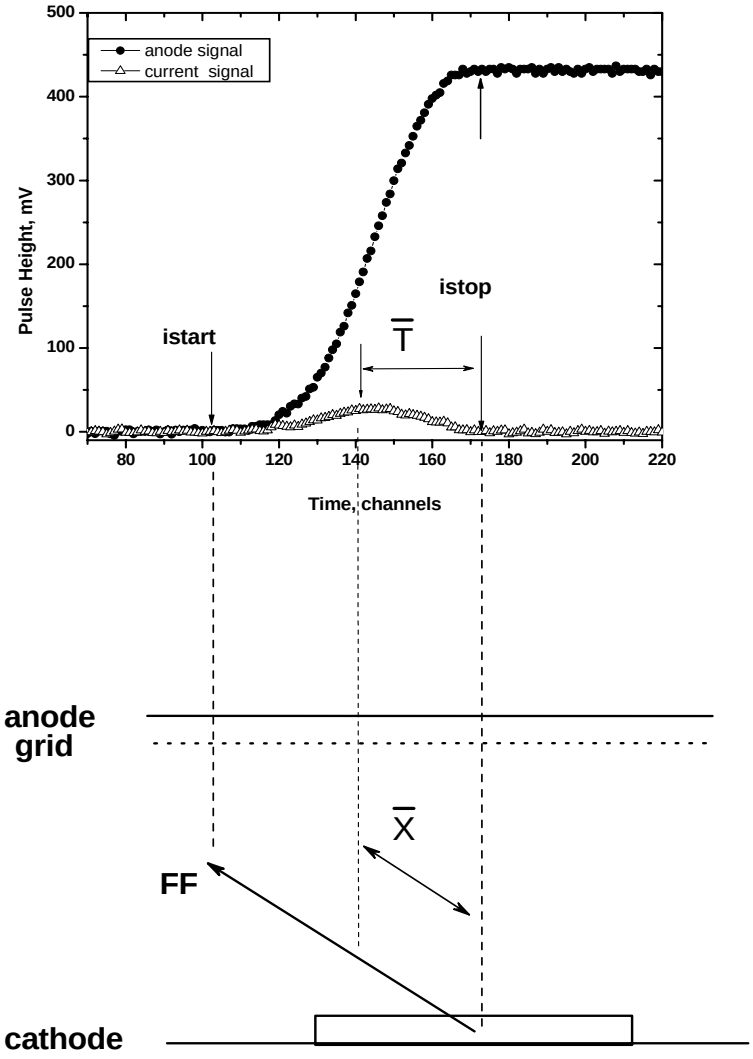

Figure 3.9: The schematic view of the center-of-gravity arrival time determination.

In our experiment we do not determine directly the distance between the origin of the ionization track and the position of the center-of-gravity of this track. This distance can be obtained from the electron drift velocity w and the time needed for the electrons to reach the anode. Figure 3.9 illustrates the schematic view of the fission fragment track and the corresponding formation of the anode pulse. When the electrons from the end of the ionization track reach the anode, the signal pulse starts (*istart*) and it stops when the last electrons from the origin of the track arrive at the anode (*istop*). In order to calculate the time $\overline{T}$ needed for the electrons located at the distance $\overline{X}$ along the track to reach the anode, we need to determine *istart* and *istop* for each event. It can be done using the following two steps procedure:

- First of all, it is necessary to apply the earlier found corrections to the anode signal and to reject the pile-up events. The used "start" position for every corrected signal is determined as 10 % of the pulse maximum (see Fig.3.5). The "stop" position is the position of the maximum of the corrected anode pulse. This value is the same for all pulses while the "start" position is different for each signal due to different fission fragment emission angles.

- Then the current signal from the corrected anode step-like signal is calculated by the differentiation of the charge pulse. The time $\overline{T}$ is determined from this current signal N_i by the following formula:

$$\overline{T} = \frac{\sum_i (t_{stop} - i) \cdot N_i}{\sum_i N_i}, \tag{3.13}$$

where i is the channel scale (i=1, 256) with 10 ns channel width. Then this value is plotted versus the corrected anode pulse height.

Fig.3.10 presents the resulting 2-dimensional distributions for the backing (a) and sample (b) sides respectively. The projections on the X and Y axes are presented in Fig.3.11. One can see the shift in pulse height distributions between the distribution of the backing side and the one for the sample side. It can be explained by the energy loss of the fission fragment in the sample and backing

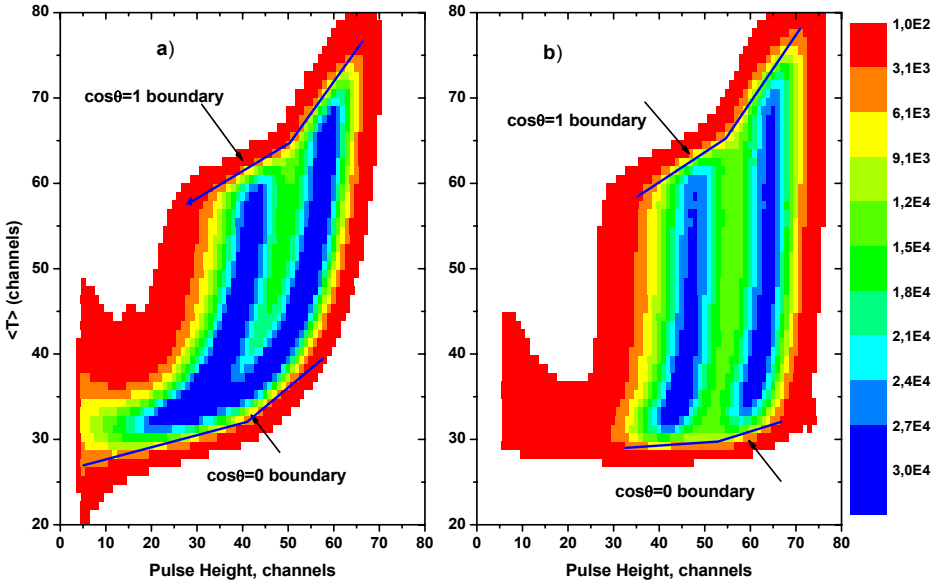

Figure 3.10: The resulting two-dimensional distributions of the "center-of-gravity arrival time" $\overline{T}$ (Eq. 3.13) of the ionization track versus pulse height of the anode signals for the backing (a) and sample (b) sides of IC.

materials. The effect of this energy loss can be also seen in the left part of Fig.3.11 in the region of small center-of-gravity values.

From the time of the center-of-gravity arrival to the anode, one can infer the emission angle of the fission fragments. The procedure of the fission fragment emission angle calculation is similar to the one applied in the case of the analogue technique. The boundaries of the 2-dimensional matrix in Fig.3.10 corresponding to $cos\theta \sim 0$ and $cos\theta \sim 1$ should be determined. It can be done by plotting for each anode pulse height channel the projection of the 2-dimensional matrix on the Y axis. The 2 maxima of this 1-dimensional spectrum give the information on the $\overline{T}$(E) values for $cos\theta \sim 0$ and $cos\theta \sim 1$, i.e. $\overline{T}_{min}$ and $\overline{T}_{max}$ values. The

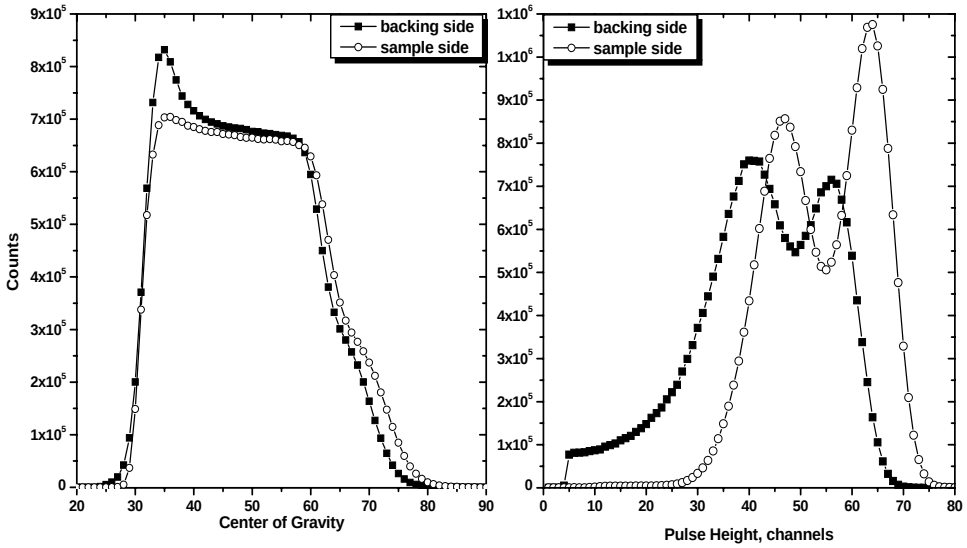

Figure 3.11: The resulting one-dimensional distributions of the "center-of-gravity arrival time" $\overline{T}$ (Eq. 3.13) of the ionization track (left) and the anode pulse height (right) for the backing and sample sides of IC.

cosine of the emission angle can then be calculated as:

$$cos\theta = \frac{\overline{T} - \overline{T}_{min}}{\overline{T}_{max} - \overline{T}_{min}}. \tag{3.14}$$

The values of the $cos\theta$ are plotted versus the anode pulse height and the resulting 2-dimensional distributions for the backing (a) and the sample (b) sides of IC are shown in Fig.3.12.

The $cos\theta$ distributions on the backing and sample (Fig.3.13) sides should be identical. So, the plot of $cos\theta_2$ for the sample side versus $cos\theta_1$ for the backing side should be a line at a 45^0 angle with respect to both axes (see Fig.3.14).

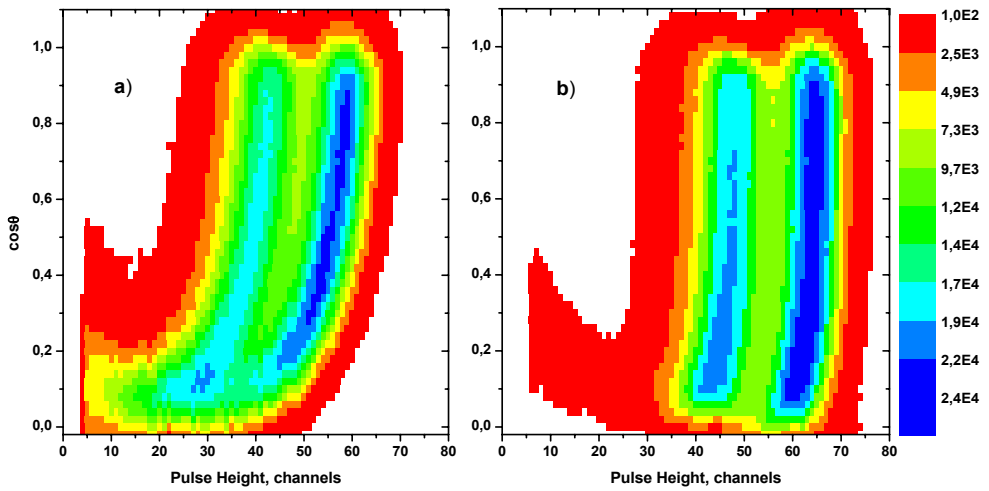

Figure 3.12: The resulting two-dimensional distributions of the cosine of the fission fragment emission angle versus the pulse height for the backing (a) and sample (b) sides of IC.

By plotting the difference $\triangle cos\theta = cos\theta_1 - cos\theta_2$ one can assess the quality of the $cos\theta$ determination (see Fig.3.15) since the $\triangle cos\theta$ distribution is perfectly centered on zero. The width if this distribution is mainly due to:

- the angular resolution of the IC;
- the fission fragments which are not perfectly aligned due to the neutron emission and fission fragment diffusion in the backing.

The information on the emission angle allows us to determine the energy loss of the fission fragments passing through the target material. The determination of the energy loss is explained in the next paragraph.

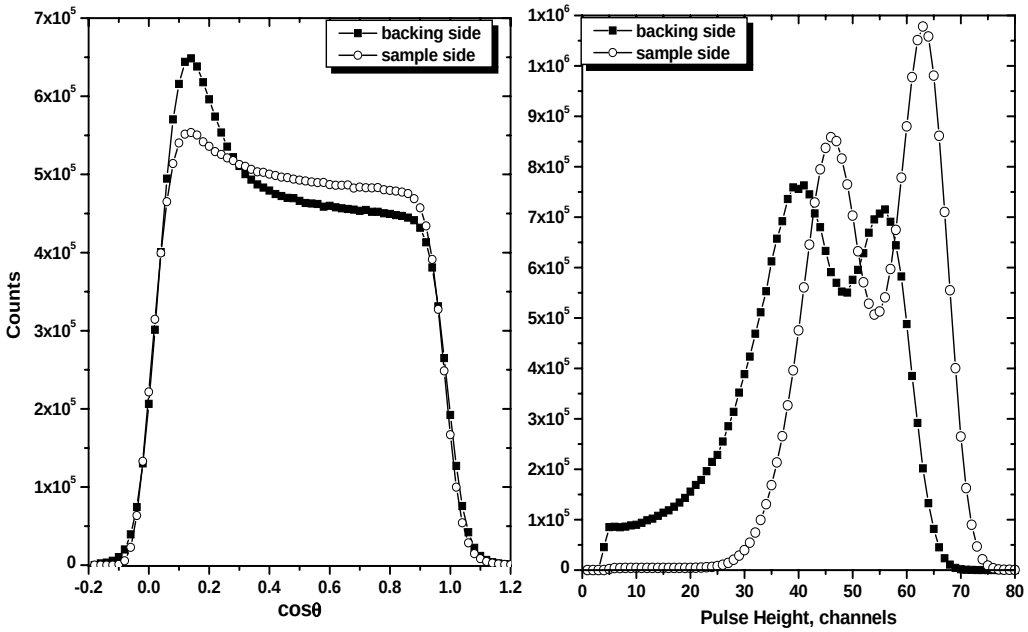

Figure 3.13: The resulting one-dimensional distributions of the cosine of the fission fragment emission angle (left) and the anode pulse height (right) for the backing and sample sides of IC.

3.1.5 Energy Loss

Due to the finite thickness of the target, the fission fragments loose their energy in the sample and backing of the target. In Fig.3.12 one can see the angle dependent energy loss of the fission fragments in the sample and backing. The energy loss of the fission fragments emitted at $\theta \sim 90^0$ is higher than the one for the $\theta \sim 0^0$. It can be explained by the fact that fission fragments emitted at $\theta \sim 90^0$ are traveling more distance in the sample and sample plus backing before they reach the atoms of the counting gas, as can be seen in Fig.3.16. Here d_{sample} and $d_{backing}$ are the distances that fission fragments emitted at angle θ with the respect to the normal to the cathode are traveling in the sample and sample plus backing,

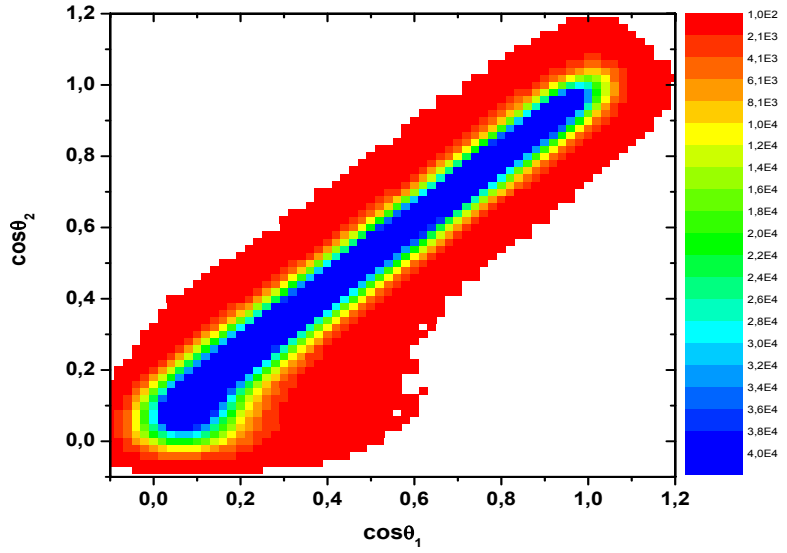

Figure 3.14: $cos\theta_2$ distribution (sample side) versus $cos\theta_1$ distribution (backing side).

respectively; t_{sample} and $t_{backing}$ are the thicknesses of the sample and backing, respectively.

Let us assume that the fission fragments were emitted at half thickness of the sample. So, the distance traveled by the fragments in the sample and backing can be expressed as:

$$d_{sample} = \frac{t_{sample}}{cos\theta_{sample}}, \tag{3.15}$$

$$d_{backing} = \frac{t_{sample} + t_{backing}}{cos\theta_{backing}}. \tag{3.16}$$

Furthermore, the energy loss in the sample and backing is known to be proportional to d_{sample} and $d_{backing}$. So the pulse height can be given as::

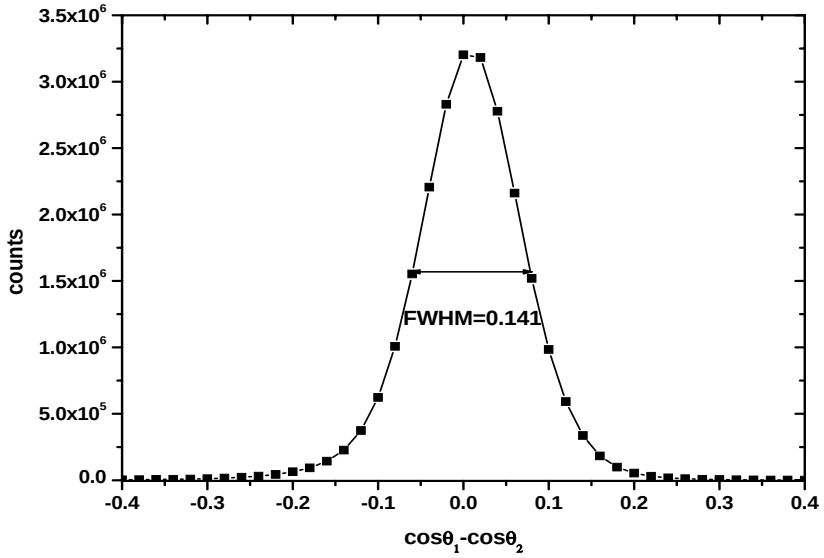

Figure 3.15: The difference in the angular distributions between two sides of the ionization chamber (backing and sample).

$$PH_{sample} = PH^{ideal} - k_{sample} \cdot \frac{t_{sample}}{cos\theta_{sample}}, \tag{3.17}$$

where PH^{ideal} is the anode pulse height in the ideal case, i.e. if the sample would have zero thickness. In the same manner one can determine the anode pulse height on the backing side:

$$PH_{backing} = PH^{ideal} - k_{backing} \cdot \frac{t_{sample} + t_{backing}}{cos\theta_{backing}}, \tag{3.18}$$

where k_{sample} and $k_{backing}$ are the proportional factors. The program operates with the 2-dimensional matrix cosθ versus anode pulse height (Fig.3.12) and searches for the positions of the maxima of the light and heavy fission fragment groups for various values of the cosine of the fission fragment emission angle. The maxima of the heavy and light fragment groups are determined by a superposition of two curves. Therefore, the average loss of the fission fragment in the sample and backing can be determined by plotting the average anode pulse height of the

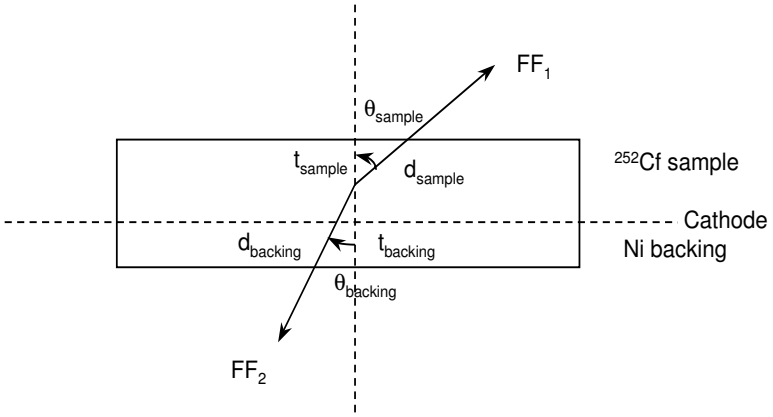

Figure 3.16: Schematic representation of the fission fragment passing through the sample and backing.

light fragment peak as a function of $1/\cos\theta$. The resulting two sets of data are presented in Fig.3.17. These two sets should converge to the same point called PH^{ideal}.

The measured average energy loss $\triangle$E in the sample is ~ 0.68 MeV/cosθ and the one for the backing is ~ 3.74 MeV/cosθ. The experimental pulse height is corrected for the energy loss and a new value of the pulse height $PH^{corrected}$ is obtained. The PH^{ideal} value is used for the calibration of the $PH^{corrected}$ to the fragment energy in MeV, as is explained in the next paragraph.

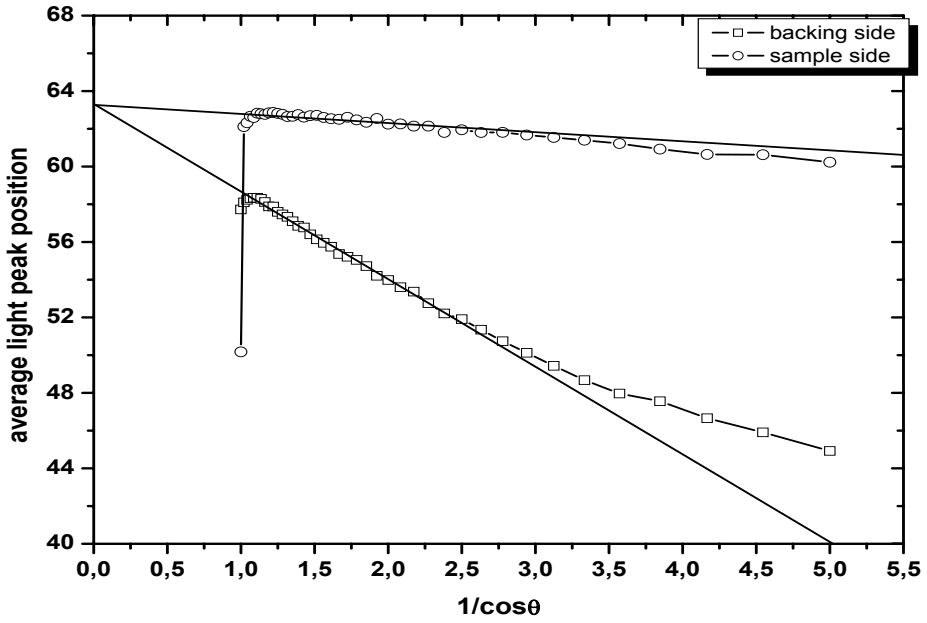

Figure 3.17: The fragment energy loss in the sample and sample plus backing as a function of $1/\cos\theta$.

3.1.6 Mass and Energy Distributions

In any experiment one can assess the properties of the fission fragments only after the emission of prompt neutrons. Pre-neutron emission mass and energy distributions can be obtained using the iterative procedure described in Ref.[Sch66].

The iteration procedure starts by assuming that the pre-neutron masses $m_1^* = m_2^* = 126$ (for ^{252} Cf), where indices 1 and 2 are related to two parts of the ionization chamber (backing and sample). The superscript *, here and in the following, indicates fission fragment properties before neutron emission. These pre-neutron masses have the pre-neutron energies E_1^* and E_2^*. From the momentum and mass conservation laws :

$$m_1^* E_1^* = m_2^* E_2^*, \tag{3.19}$$

$$m_1^* + m_2^* = A, \tag{3.20}$$

$$m_i = m_i^* - \overline{\nu}_i(m_i^*), \tag{3.21}$$

where i=1,2; A is the mass of compound nucleus (A=252) and $\overline{\nu}_i(m_i^*)$ is the number of neutrons emitted from the i-th fragment, one can obtain:

$$m_1^* = A\frac{E_2^*}{E_1^* + E_2^*}, \tag{3.22}$$

$$m_2^* = A\frac{E_1^*}{E_1^* + E_2^*}. \tag{3.23}$$

It is obvious that the pre-neutron energy should be known in order to determine the pre-neutron mass. As mentioned above, during the experiment and after the off-line analysis one has access to the post-neutron emission properties, i.e. corrected anode pulse height that is proportional to the post-neutron energy of the fission fragment. When the experimental values of the anode pulse height are corrected for the energy loss of the fission fragments in the sample and its backing one can obtain the post-neutron energies. It can be done by the calibration of the corrected pulse height to the known value of the average kinetic energy of the light fragment as:

$$E_i(MeV) = \overline{E}_i^{light}(MeV) \cdot \frac{PH_i^{corrected}(channels)}{PH_i^{ideal}(channels)}, \tag{3.24}$$

where PH^{ideal} is the value of the ideal pulse height in channels found during the energy loss determination (see paragraph 3.1.5), $\overline{E}^{light}$ is the known average kinetic energy of the light peak for ^{252}Cf, i=1,2 for backing and sample of the target.

Then the obtained post-neutron energies should be corrected for the Pulse Height Defect (PHD) as explained in Refs. [Bud87], [Ham95], [Tov02] :

$$E_i^{corrected} = E_i + PHD(m_i). \tag{3.25}$$

Pulse Height Defect occurs due to the non-ionizing collisions of the fission fragments and the atoms of the counting gas while these fragments are slowing down in the gas. The PHD depends on the gas mixture. The detailed explanation of the PHD calculation is given in Appendix A.

The procedure, developed by Schmitt, Neiler and Walter [Sch66] allows to deduce the pre-neutron masses m_i^* from the experimentally measured quantities. Let us assume that the fission fragment velocities stay almost unchanged, i.e. V_i^*=V_i although their kinetic energies change due to the neutron emission. The reason of this assumption is the conservation of momentum as well as the fact that the neutrons are emitted isotropically in the center-of-mass-system of the fragments (in its own reference frame). Therefore:

$$E_i^* = E_i \frac{m_i^*}{m_i}. \tag{3.26}$$

So, substituting the pre-neutron energies in (Eqs. 3.22 - 3.23) by its expression as a function of the post-neutron energy (Eq. 3.26), one obtain the pre-neutron mass as:

$$m_1^* = A \cdot \frac{\frac{m_2^*}{m_2} E_2}{\frac{m_1^*}{m_1} E_1 + \frac{m_2^*}{m_2} E_2}, \tag{3.27}$$

$$m_2^* = A \cdot \frac{\frac{m_1^*}{m_1} E_1}{\frac{m_1^*}{m_1} E_1 + \frac{m_2^*}{m_2} E_2}. \tag{3.28}$$

After the simplification, Eqs. (3.27 - 3.28) become:

$$m_1^* = A \cdot \frac{E_2}{\frac{E_1}{1+\beta} + E_2}, \tag{3.29}$$

$$m_2^* = A \cdot \frac{E_1}{E_1 + E_2 \cdot (1+\beta)}, \tag{3.30}$$

where

$$1+\beta = \frac{m_2^*}{m_2}\cdot\frac{m_1}{m_1^*} = \frac{m_2+\overline{\nu}(m_2^*)}{m_1+\overline{\nu}(m_1^*)}\cdot\frac{m_1}{m_2} = \frac{1+\overline{\nu}(m_2^*)/m_2}{1+\overline{\nu}(m_1^*)/m_1}. \tag{3.31}$$

The $\overline{\nu}(m_i^*)$ values are taken from Ref.[Bud88]. The iteration procedure is repeated starting now with the new values of the pre-neutron mass Eqs. (3.29-3.30). Calculations are finished when the values of m_i^* converge to less than 1/8 amu.

The provisional masses can be obtained by assuming β=0, i.e. no neutron emission. The resulting mass, energy and total kinetic energy distributions for the ^{252}Cf(sf), as well as the comparison of the obtained results with published data is presented later in this document. But first, the dependence of the center-of-gravity to the fragment mass should be considered and taken into account.

3.1.7 Final Correction of the Angular Distribution

In the previous paragraph only the energy dependence of the center-of gravity was discussed. Actually, $\overline{X}$ depends not only on the fragment energy but also on the mass and charge of the fission fragments $\overline{X}(E,A,Z)$. After the neutron correction one can plot the $cos\theta$ as a function of the post-neutron mass (see Fig.3.18 (left)). The effect of the mass dependence of $\overline{X}$ can be seen in the two "wings" at $cos\theta \sim 1$. It can be corrected in the same way as described in paragraph 3.1.4. The result of the correction is presented in Fig.3.18 (right).

3.2 Results and Comparison with Literature

3.2.1 Results

The resulting pre- and post-neutron fragment mass and kinetic energies distributions for the backing and sample sides are presented in Fig.3.19.

The kinetic energy distributions for the backing and sample sides should be identical for both sides of the ionization chamber. It indicates the quality of the

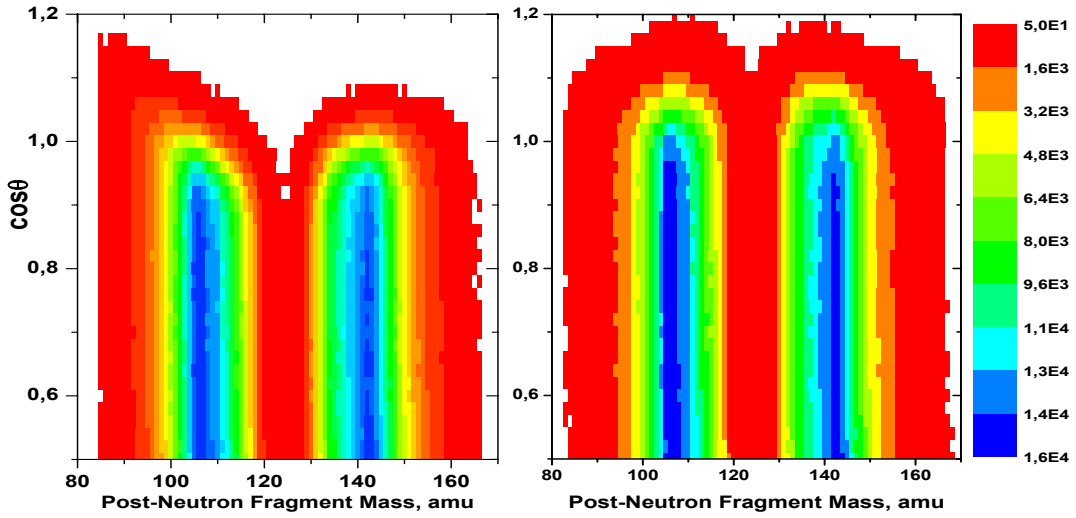

Figure 3.18: The fragment angular distribution as a function of the post-neutron mass before correction of the dependence of $\overline{X}$ on the fragment mass (left) and after correction (right), respectively.

applied corrections to the anode signal and determination of the post-neutron energy from the anode pulse.

Good agreement of the present data with literature was observed (see next paragraph).

3.2.2 Comparison with Literature Data

Analysing pre-neutron energy distributions obtained in this work, one can infer the mean values for light and heavy peak positions. These values are 104.62 ± 0.5 MeV and 80.2 ± 0.5 MeV, respectively. If we now compare those values with the known literature data (Tab.3.1) one note a good agreement with the values recommended by Goennenwein (see Ref.[Gon91]).

The obtained uncertainties are due to the statistics and systematics, i.e. due to all corrections applied to the anode signal.

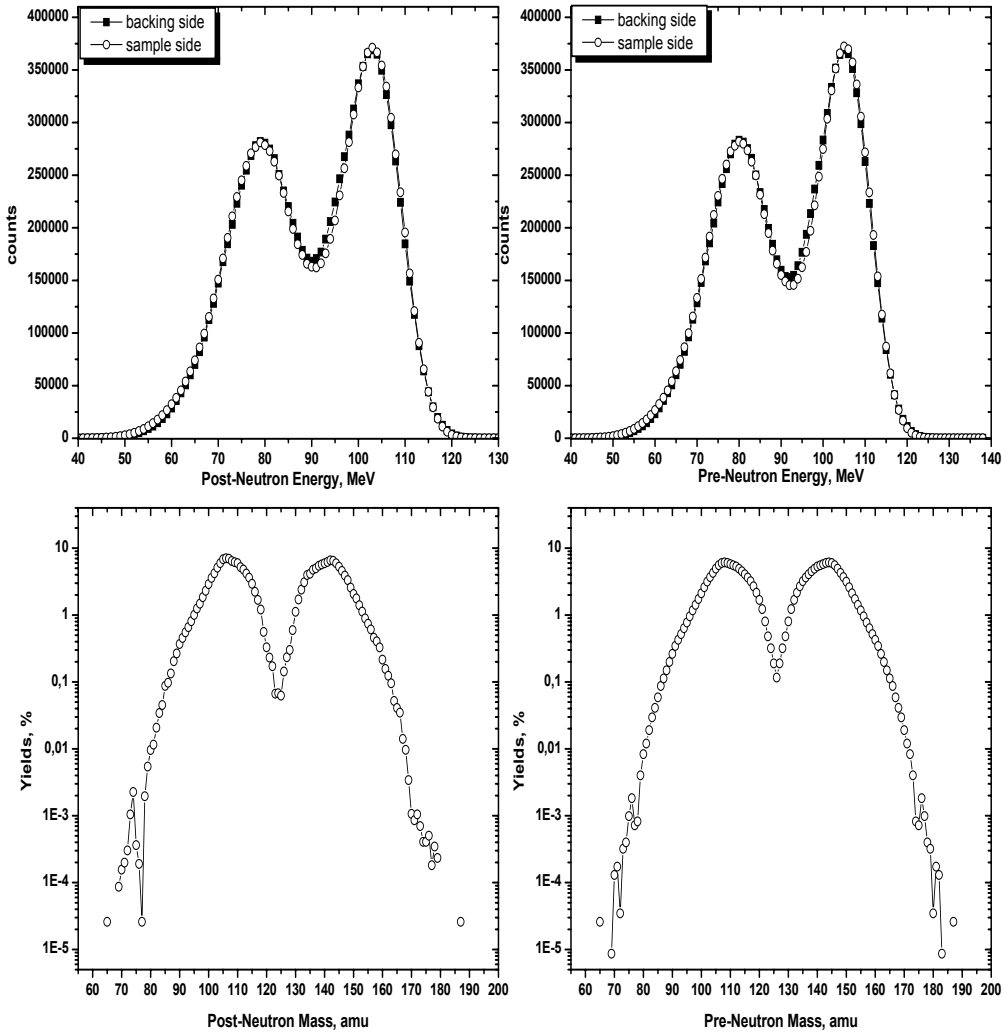

Figure 3.19: Fission fragment pre- and post-neutron mass yields and kinetic energy distributions ($\cos\theta > 0.5$).

If we now compare the mean values of the pre-neutron total kinetic energy (TKE) presented in Tab.3.1 a good agreement with the values recommended by Goennenwein [Gon91] is observed. The data collected in this table were obtained using different methods of fission fragment properties determination such as double energy and double velocity methods.

Literature	KE_L^* (MeV)	KE_H^* (MeV)	TKE^* (MeV)
[Whe63]	105.71 ± 1.06	80. ± 0.8	185.70 ± 1.8
[Sch66]	106.2 ± 0.7	80.3 ± 0.5	186.50 ± 1.2
[Bar85]	105.5 ± 0.6	80.3 ± 0.4	185.80 ± 1.0
[Bud87]	102.7 ± 1.1	79.2 ± 1.0	181.40 ± 2.0
[Gon91]	104.7 ± 0.7	79.4 ± 0.5	184.10 ± 1.3
[Tov02]	102.9 ± 1.1	78.9 ± 1.0	181.40 ± 2.0
Present work	104.62 ± 0.5	80.2 ± 0.5	184.82 ± 1.0

Table 3.1: Comparison of the mean values of the pre-neutron fragment kinetic energy for light and heavy peaks and TKE^* obtained in this work with literature data.

It is also interesting to look at the pre-neutron mass yields and compare the mean values for the light and heavy peak positions (Table 3.2). Again we can note a good agreement of the results obtained using the digital technique with Goennenwein's recommendations [Gon91].

Literature	$Mass_L^*$ (amu)	$Mass_H^*$ (amu)
[Whe63]	108.4	143.6
[Sch66]	108.55	143.45
[Bar85]	108.6	143.4
[Bud87]	109.3 ± 0.1	142.7 ± 0.1
[Gon91]	108.6	143.5
[Tov02]	109.0 ± 0.1	143.0 ± 0.1
Present work	108.76 ± 0.1	143.28 ± 0.1

Table 3.2: Comparison of the pre-neutron fragment mass of the present work with the literature data

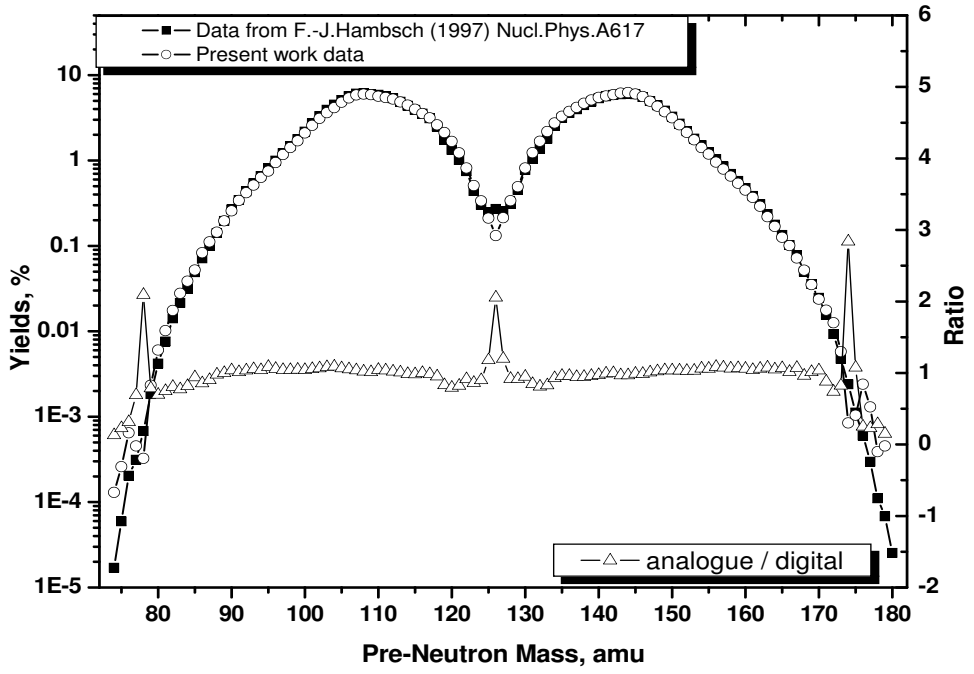

Figure 3.20: Comparison of the pre-neutron mass yields obtained using the digital (open circles) and the analogue (black squires) techniques ($\cos\theta > 0.9$). The ration between both distributions must be read at the right scale.

The mass yields obtained using the digital technique (our work) and the analogue one [Ham97] are compared in Fig.3.20. Good agreement can be observed except may be in the very asymmetric mass region ($M_L < 80$ amu and $M_H > 170$ amu). In our pre-neutron mass distributions the "shoulders" appear in this very asymmetric mass region (see also Fig.3.19). Similar behavior was obtained by Barreau [Bar85]. It is believed that this behavior is not caused by the correction for prompt neutron emission as reported by Barreau (as explained in 3.2.3).

If we now look at the fragment kinetic energy and total kinetic energy as a function of the fragment mass (Figs. 3.21-3.22) we can observe a small bump at $M_H \approx 176$ amu (see Fig. 3.21) which was also observed by Barreau [Bar85].

The total kinetic energy as a function of the pre-neutron fragment mass is presented in Fig.3.22 where one can observe the bump at M_H=146 amu. This

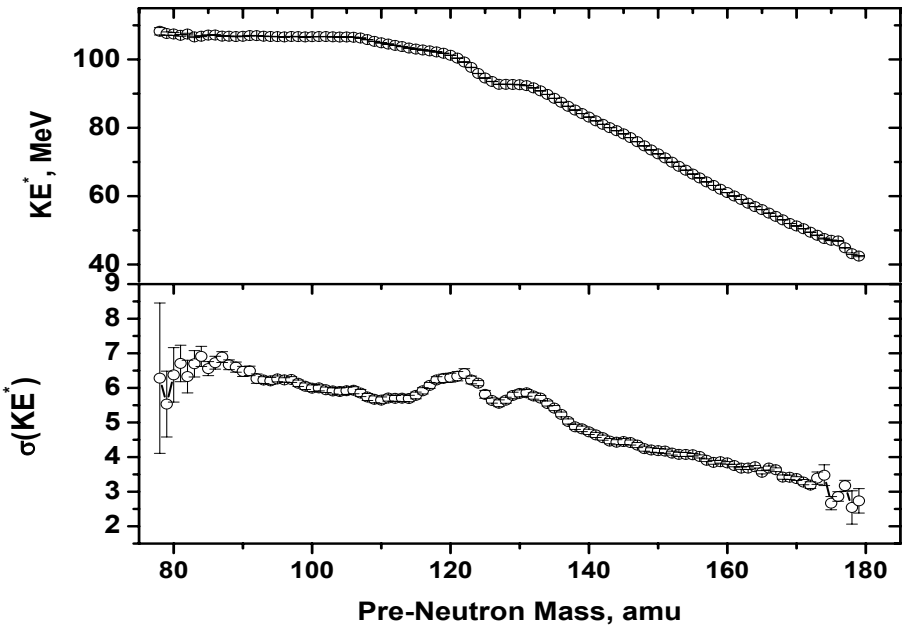

Figure 3.21: The fragment pre-neutron kinetic energy (up) and the standard deviation σ of the kinetic energy (down) as a function of the pre-neutron fragment mass. The presented small uncertainties are only statistical errors.

small bump was also discussed in [Bar85]. It might be explained by the deformed neutron shell for N $\approx$ 88 in the heavy fragment.

In Figs. 3.21-3.22 the standard deviations for the fragment kinetic and total kinetic energies are presented. Comparing σ_{TKE} obtained in this work with the one from [Sch66] one can see that close to the symmetry (M_H=130 amu) σ_{TKE} reaches a maximum value at almost 12.5 MeV while Schmitt reported a value of 14.5 MeV. Our data are in good agreement with the ones obtained by Barreau [Bar85].

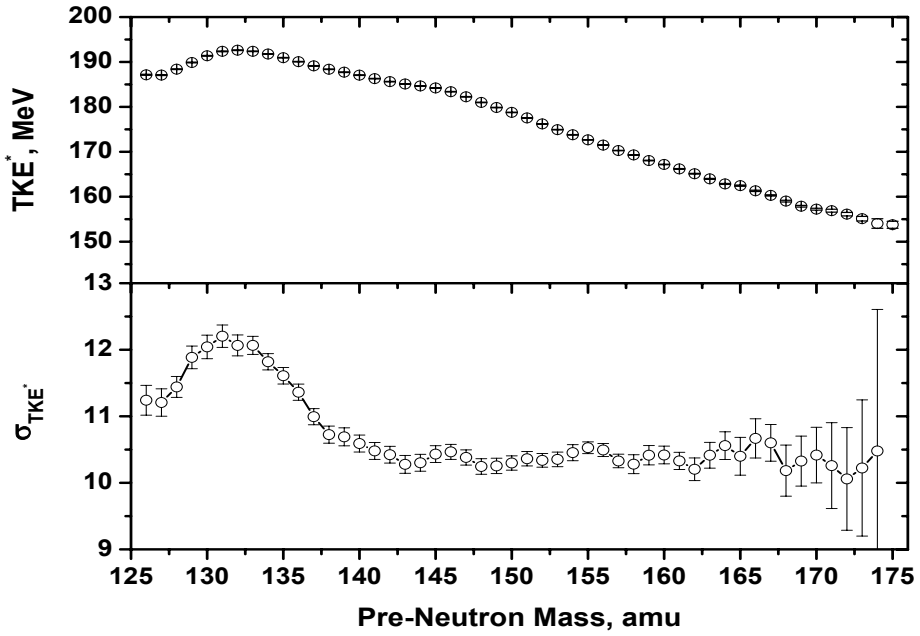

Figure 3.22: The average total kinetic energy as a function of the pre-neutron mass (up) and its standard deviation σ (down) as a function of the pre-neutron fragment mass.

3.2.3 Impact of the $cos\theta$ Limits Selection

In Ref.[Ham97] it was shown that the enhanced far asymmetric yield in the spontaneous fission of ^{252}Cf observed in [Bar85] and [Bud88] is most probably an artificial effect due to energy degradation. In the present work this enhancement was not observed; different cosine limits ($\cos\theta > 0.9$ and $\cos\theta > 0.5$) were considered and fission fragment yields for the selected angular cones were compared. It was found by Hambsch [Ham97] that by reducing the angular cone, in order to take into account only the events for which $\cos\theta > 0.9$, the enhancement disappears. In our work this effect was not observed as it can be seen in Fig.3.23 where the mass yields for the two angular cones ($\cos\theta > 0.9$ and $\cos\theta > 0.5$) are presented. It can be explained due to the use of the digital technique.

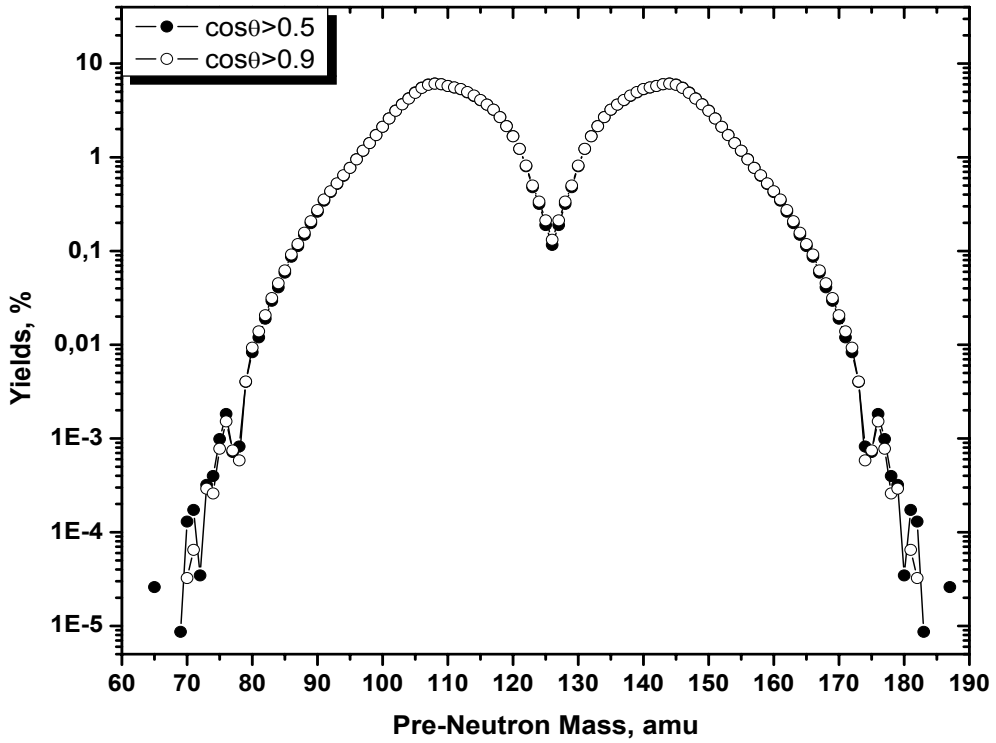

Figure 3.23: Pre-neutron mass yields for the different cosθ limits.

Chapter 4

Prompt Neutron Analysis

In this chapter a detailed description of the off-line analysis of the experimental data is given. The first part describes the NE213 calibration using γ - sources with well known energies Eγ. The second part of this chapter describes the analysis procedure of the neutron detector signals. Two methods used for the time-mark determination for the Time-of-Flight spectrum calculations are discussed.

4.1 Neutron Detector Calibration

The detection mechanism of a NE213 scintillator is based on proton recoil by elastic scattering. In order to determine the incident neutron energy and to estimate the detection threshold it is necessary to calibrate the neutron detector (to relate the channel number, i.e. the integrated charge of the detector pulses Q_{tot}, to light outputs) and to know its response function.

The calibration of the liquid scintillator NE213 was performed using 3 γ-sources with known energies ^{241}Am (Eγ=59.54 keV), ^{60}Co (Eγ=1173 keV,Eγ=1333 keV), ^{22}Na (Eγ=511 keV, Eγ=1274.54 keV). In case of ^{60}Co the value of the light output Q_{tot} was determined for the average of the 2 lines, i.e. Eγ=1252.87 keV since the resolution of the NE213 was not sufficient to distinguish both lines. Every source was placed at the center of the entrance window of the detector. The anode signal from the photomultiplier was sent to the channel 0 of the WFD1. In this measurement the external trigger was created only from the dynode signal of the NE213 (see Fig.4.1).The measuring time of every γ-source was 1 hour.

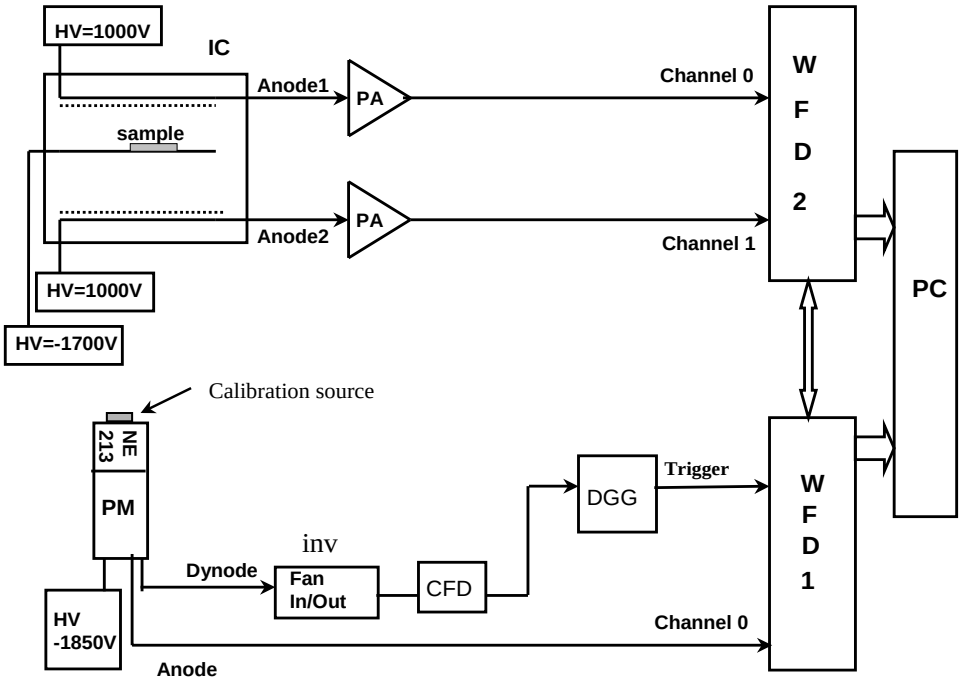

Figure 4.1: Schematic layout of the detector calibration measurement. PA - PreAmplifier; TFA - Timing Filter Amplifier; CFD - Constant Fraction Discriminator; HV - High Voltage; CU - Coincidence Unit; WFD - Wave Form Digitizer; DGG - Dual Gate Generator; PC - Computer

For the calibration measurements the amplification of the neutron detector was set to be able to see ^{241}Am (Eγ=59.54 keV). During the measurements with other γ-sources one could observe the signals with the amplitude greater than the 2 Volts. Unfortunately, these signals were not correctly digitized by the WFD due to its features (12 bit). So, during the analysis the saturated events (with an amplitude greater than the 2 Volts allowed by the WFD) were rejected. Fig.4.2 presents the spectra in the pulse height scale. One can see the large number of the events with an amplitude greater than 2V. The rejection of such events does not influence the calibration curve but influences the detector efficiency, as explained

later.

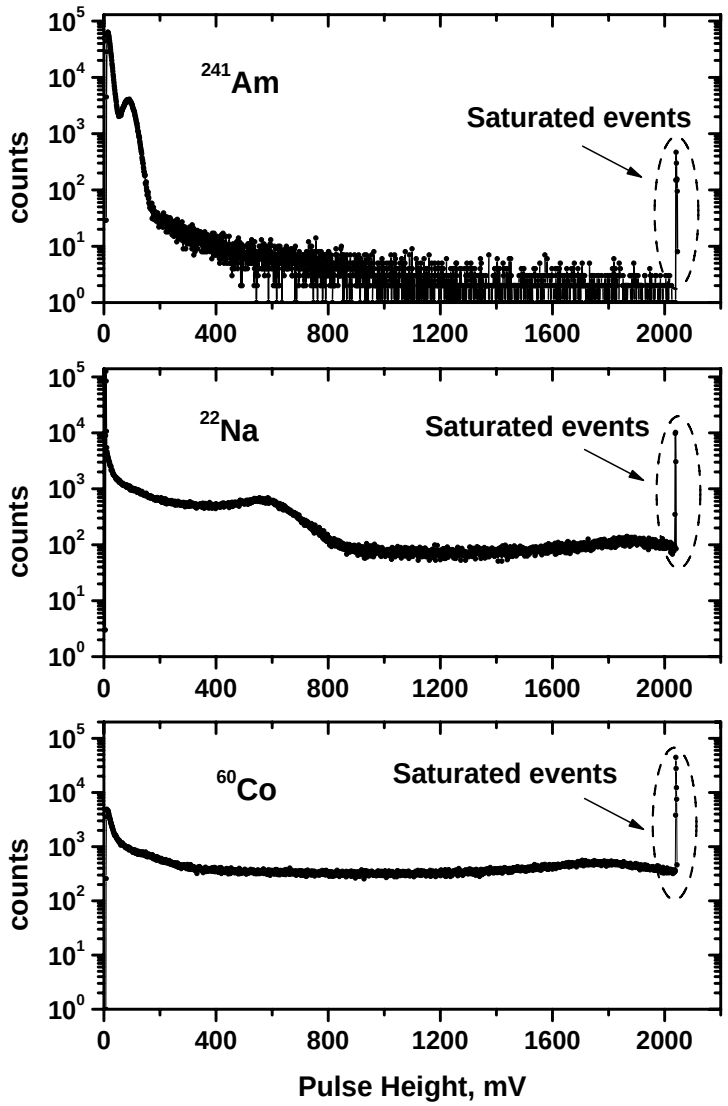

Figure 4.2: Electron recoil spectra for ^{241}Am, ^{60}Co, ^{22}Na in the pulse height scale.

In order to obtain the calibration curve it is necessary to know the light outputs Q_{tot}. The resulting pulse height distributions for the used γ-sources after the rejection of the saturated signals are presented in Fig.4.3.

The energy of a Compton-recoiled electron after Compton scattering of an

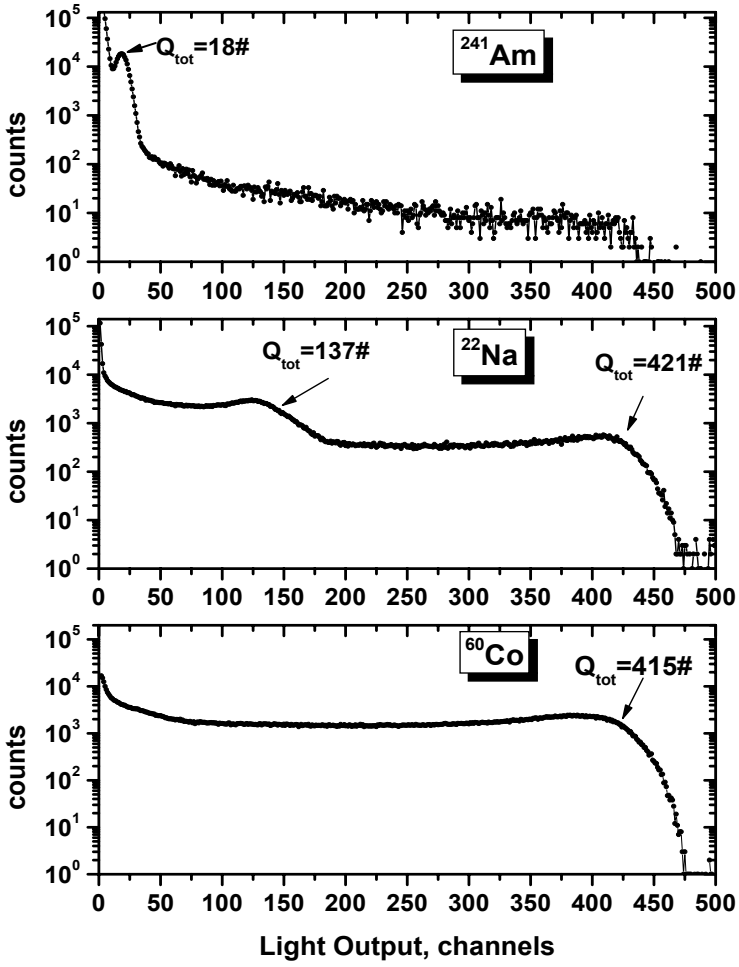

Figure 4.3: Electron recoil spectra for the γ-sources with known energies ^{241}Am (E=59.54 keV), ^{60}Co (E_γ=1252.87 keV), ^{22}Na (E_γ=511 keV, E_γ=1274.54 keV).

incident γ-ray with energy E_γ is given by:

$$E_{e^-}^{max} = \frac{2E_\gamma^2}{m_e c^2 + 2E_\gamma}. \tag{4.1}$$

The maximum energy of Compton recoiled-electrons $E_{e^-}^{max}$ corresponds to the position 80% down the height of the Compton edge (indicated by the arrows in

Fig. 4.3). The light, created in the scintillator, is due to the recoiled electrons, so the $E_{e^-}^{max}$ is expressed in keV equivalent electron, i.e. keVee. The determined Compton edge for the corresponding E_γ provides a calibration curve that is presented in Fig.4.4.

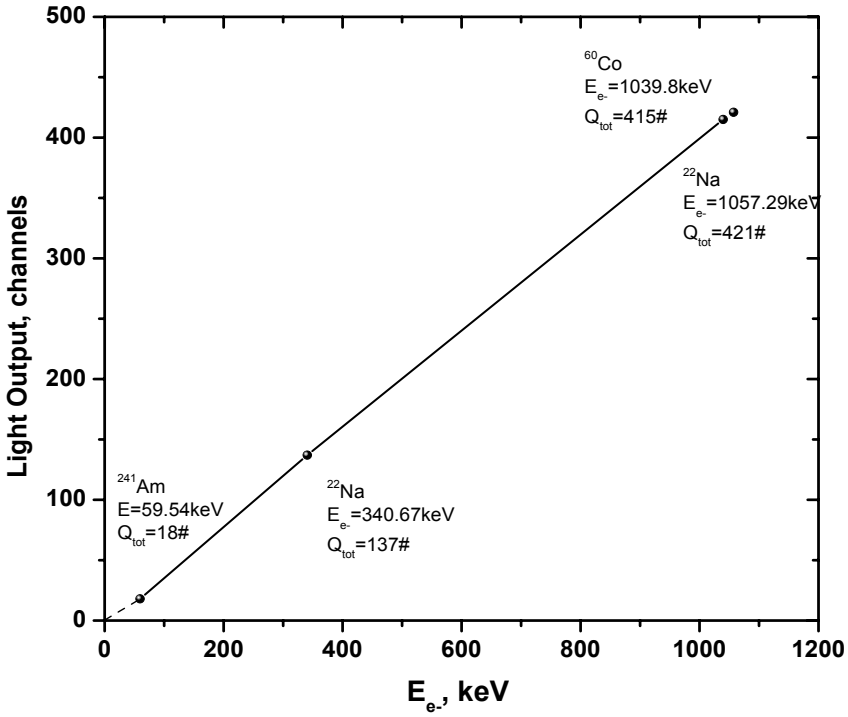

Figure 4.4: The calibration curve.

The calibration curve shows a very good linearity:

$$Q_{tot}(channels) = -3.5116 + 0.4025 \cdot E_{e^-}(keV). \tag{4.2}$$

In order to determine the resolution of the detector one can perform a Monte Carlo simulation. To realize this simulation the MCNPX Monte Carlo code [Wat04] was used that has the capability to simulate the experimental γ-spectra. However, the resolution parameters have to be known a priori. So, a possible way

to find these parameters is to simulate the raw γ-spectrum (no resolution) in a first step. In a second step, a home-made code performs the convolution product of this raw spectrum with a Gaussian [Lit06]. The Full Width at Half Maximum (FWHM) of the Gaussian can be expressed by the well-known NE213 resolution function:

$$\frac{FWHM}{E} = \sqrt{\alpha^2 + \frac{\beta^2}{E} + \frac{\gamma^2}{E^2}}. \tag{4.3}$$

The Gaussian parameters (the resolution parameters α, β, γ) are obtained by a minimization procedure, i.e. MINUIT2 package [Jam04] developed at C.E.R.N.. This package is used to minimize the χ^2 between the experimental spectrum and the broadened calculated spectrum. The minimum χ^2 gives the resolution parameters. In our case, the resolution was found to be equal to 12 % at 1 MeV. The measured and calculated Compton electron pulse height distributions for ^{22}Na and ^{60}Co sources are presented in Fig.4.5

The electron recoil spectra for γ-sources as well as the calibration curve allow us to find not only the detector resolution but also to determine the value of $E_{threshold}$ from the minimal light output Q_{tot}. For our neutron detector the value of Q_{totmin} corresponds to $E_{e^-} \sim 7$ keVee (from the Eq. 4.2). According to Ref.[Sch02] for the NE213 scintillator, $E_{threshold}$ for the protons can be determined from the following response function:

$$E_{e^-} = 0.83 \cdot E_p - 2.82 \cdot [1 - exp(-0.25 E_p^{0.93})], \tag{4.4}$$

where E_{e^-} is expressed in MeVee, i.e. in MeV equivalent electron, and E_p in MeV.

Finally:

$$E_{e^-} \sim 7keVee => E_p = E_{threshold} = 150keV \tag{4.5}$$

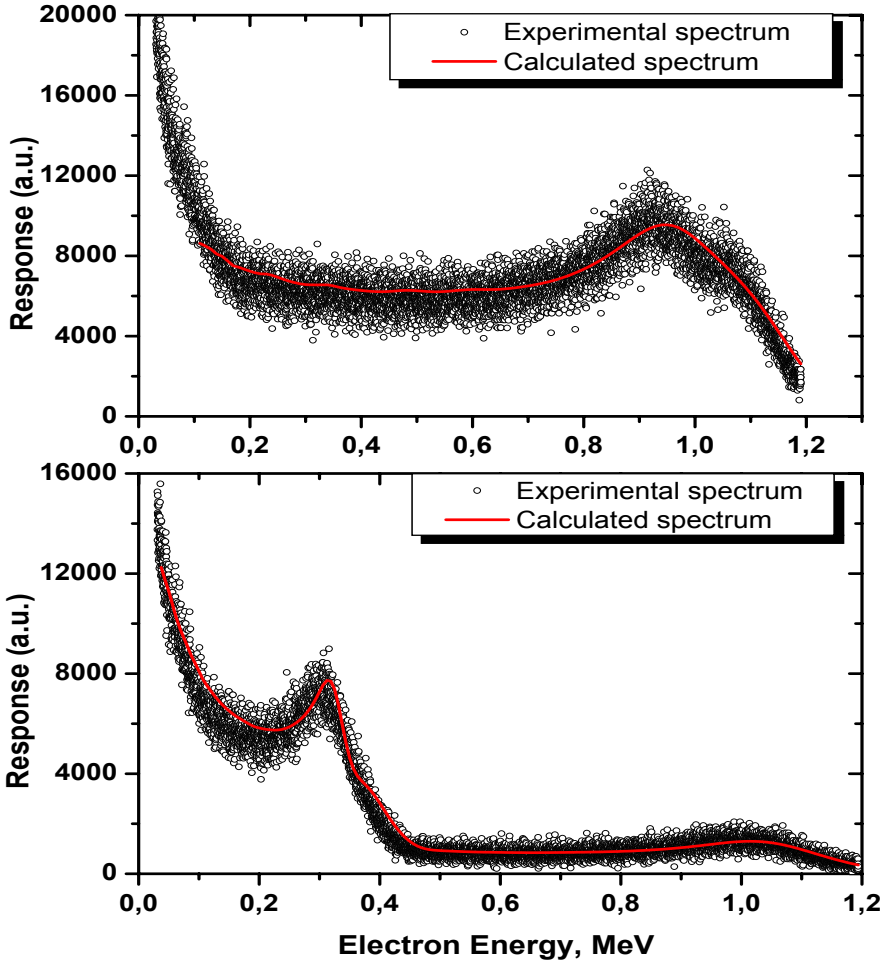

Figure 4.5: Measured and calculated pulse height spectra for ^{60}Co (up) and ^{22}Na (bottom) sources.

4.2 Neutron Identification

4.2.1 "Bad" Events Rejection

The neutron analysis was performed off-line on the coincident events. An example of such events is presented in the Fig.4.6.

The first step of the analysis is the correction for the base line fluctuation.

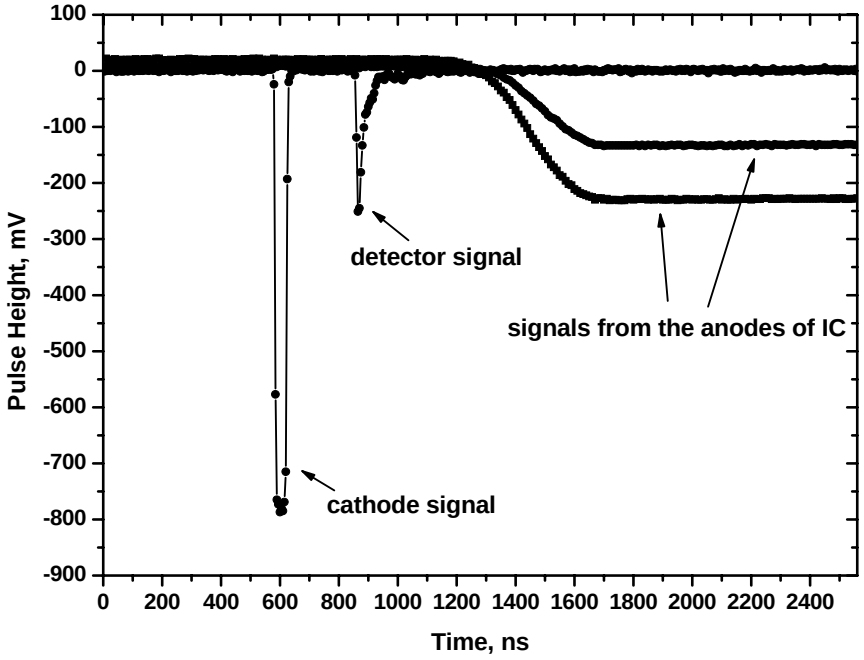

Figure 4.6: Typical waveforms from the ionization chamber and neutron detector.

Then so called "bad" events should be determined and rejected. Such events were recorded because both WFD's were working in internal trigger mode. Examples of "bad" events are presented in Fig.4.7:

a) - a saturated detector pulse, i.e. the amplitude of the signal was more than 2V. Only signals with amplitude less than 2V were saved correctly by WFD (12 bit). In principle, it is possible to reconstruct such events in order to avoid their rejection as shown by Kornilov [Kor03];

b) - events where the detector pulse appears in the WFDs channels after channel 458 (i.e. more than 2.29 μsec). In that case it is not possible to determine correctly the slow component for the Pulse Shape Discrimination (PSD);

c) - events with two or more signals from the cathode of the ionization chamber.

Only after the rejection of such events the further analysis of the data can be performed.

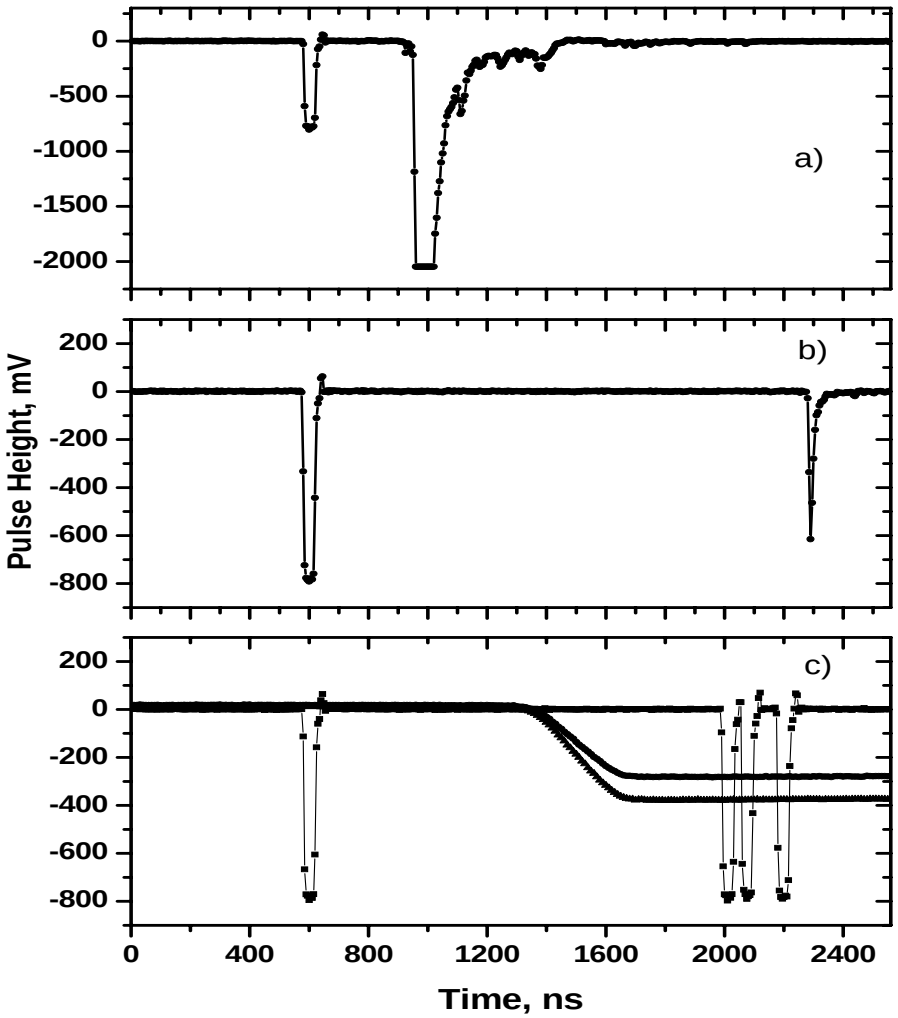

Figure 4.7: Examples of the different types of "bad" events: a) saturated pulse; b) detector pulse arrives after channel 458; c) 2 or more signals from the cathode.

4.2.2 Pulse Shape Discrimination

The Pulse Shape Discrimination (PSD) in organic scintillators has been known for many years, particularly for the liquid scintillator NE213. PSD is possible due to the long-lived decay of scintillator light caused by the specific energy losses (dE/dx) of the different particles in the detector material. Figure 4.8 illustrates

the different decay times exhibited by the liquid scintillator.

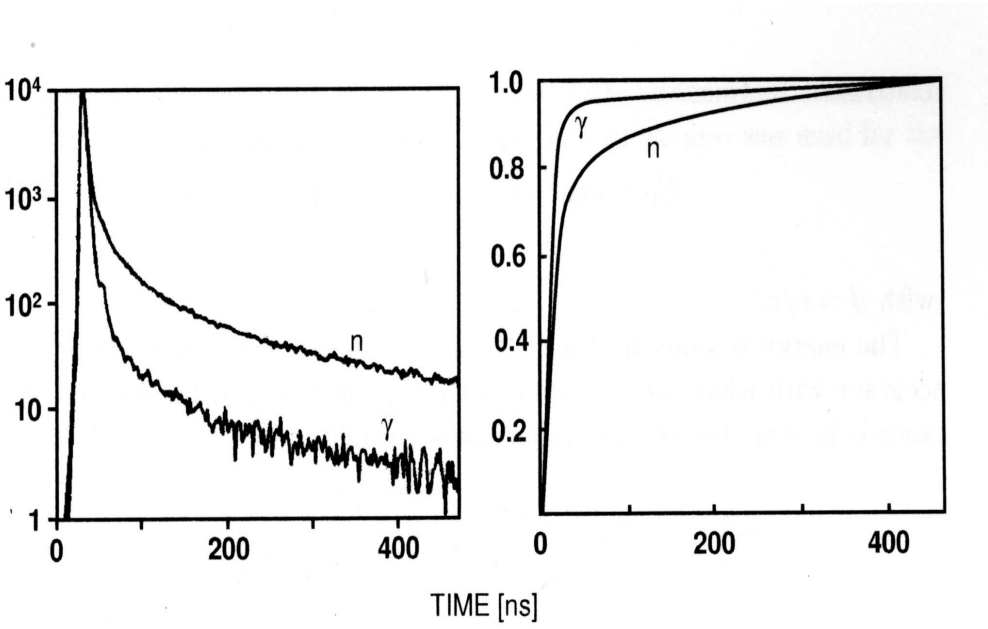

Figure 4.8: Original pulse shapes (left) and integrated pulses (right) from a NE213 liquid scintillator by interaction of neutrons and γ (Adopted from Ref.[Leo87]).

The shape of the emitted light pulse can be described by a single fast decay component and a substantial slow component. It is known that the effectiveness of n/γ discrimination depends on the position and width of the gate at the slow and fast components. The use of the digital technique allows us to set, off-line, the best position and width of these gates in order to achieve the best discrimination between neutrons and γ's without repeating the experiment. A special software was developed and the best PSD was achieved with gates of 25 ns for the fast component and 250 ns for the slow component (see Fig.4.9).

The resulting two dimensional spectrum of the fast component charge versus the slow component charge is shown in Fig.4.10. Two well separated branches corresponding to γ-rays and neutrons can be observed.

The quality of the n/γ separation can be assessed by the Figure Of Merit (FOM) quantity:

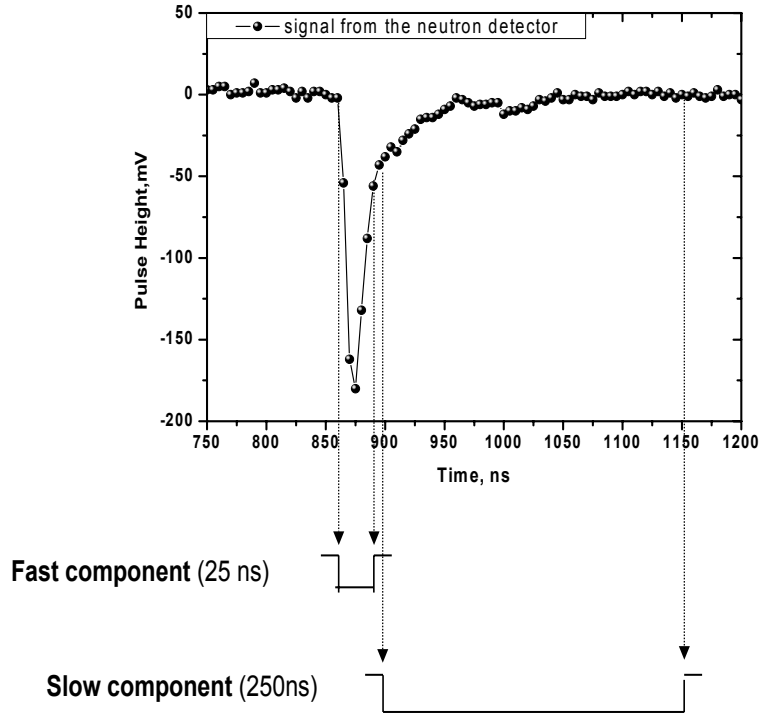

Figure 4.9: The timing windows for the pulse shape discrimination.

$$FOM = \frac{S_{n\gamma}}{F_n + F_\gamma}, \tag{4.6}$$

where $S_{n\gamma}$ represents the separation of 2 peaks; F_n and F_{gamma} are the n, γ peak centroid positions, respectively. This method is similar to the conventional analogue PSD technique. A FOM more than 1 is required for "good" PSD (Fig.4.11). In this figure the proton energies E_p for the corresponding Q_{tot} values (from Fig. 4.10) are determined from the calibration of the neutron detector (Eq. 4.2) and the response function for NE213 detectors (see Eq. 4.4).

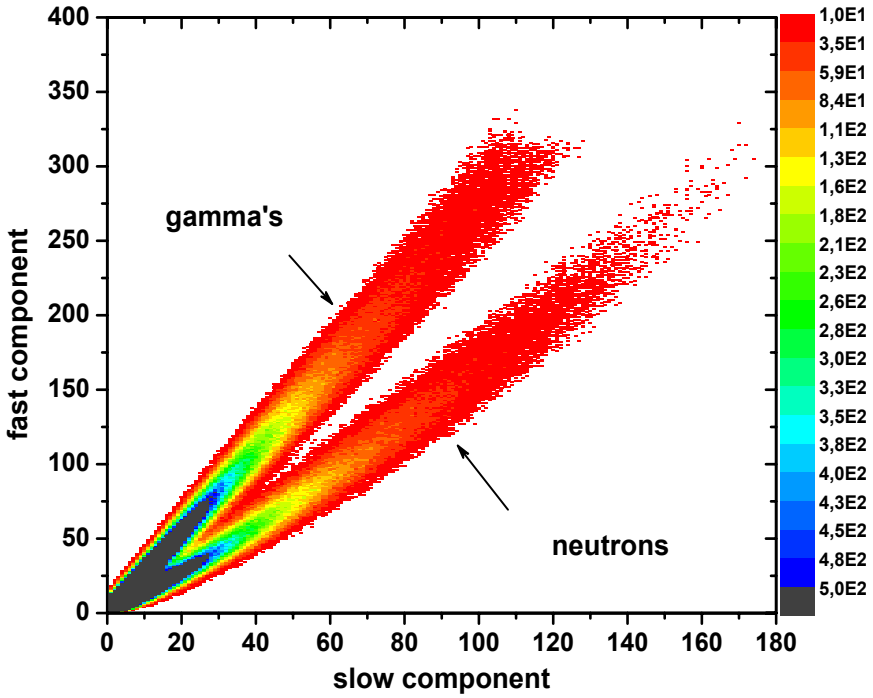

Figure 4.10: Discrimination between γ-rays and prompt emitted neutrons from fission of ^{252}Cf by Pulse Shape Analysis.

4.2.3 Time-Of-Flight Technique

The Time-Of-Flight (TOF) method was used to determine the energy of the prompt neutrons from ^{252}Cf(sf) and then to infer the detector efficiency. This method is based on the measurement of the time difference T_{TOF} between the neutron production and the moment it hits the detector. The cathode signal from IC gives the time of the neutron production while the detector signal gives the time when the neutron is detected in NE213. The time that neutrons and γ's need to cover the distance L=1.47 m can be determined as $T_{TOF}=T_{det}$ - T_{IC}. As we will see later, a reliable determination of the "start" signal (given by the cathode of IC) and "stop" signal (given by the anode signal of the neutron detector) leads to a timing resolution less than the WFD channel width (5 ns/channel in

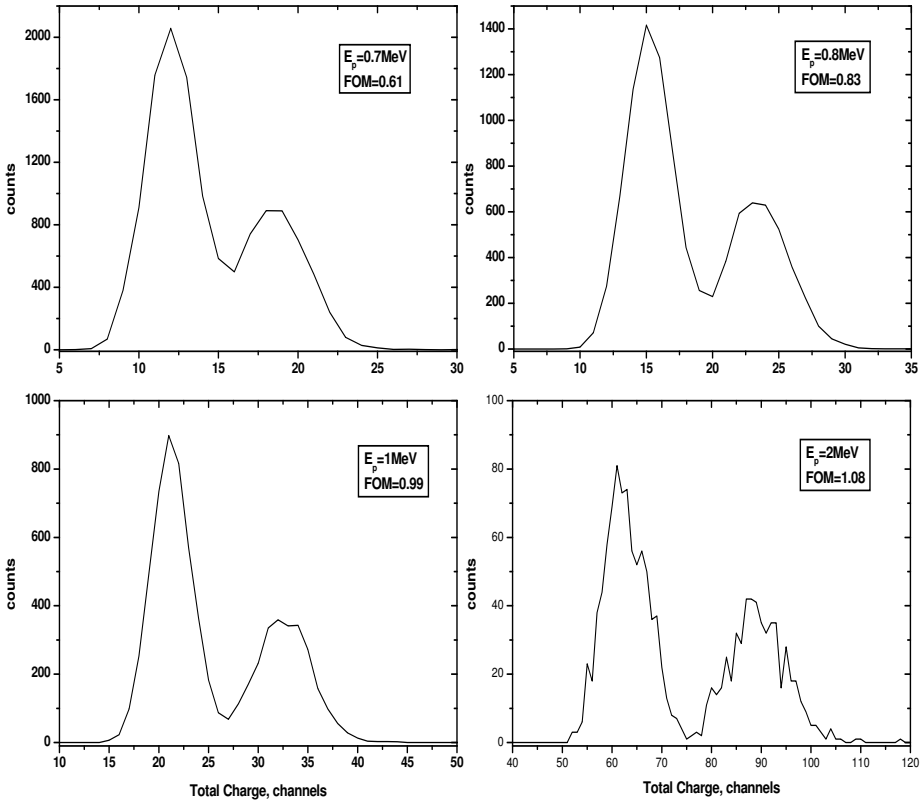

Figure 4.11: The spectra of the n/γ separation obtained for the different energies E_p.

our experiment). In order to be able to obtain this resolution the width of the cathode signal was enlarged in the CFD. Having both signals in one channel we also avoid the possible problem of the synchronization of different WFD channels. For the determination of the time marks (T_{det}, T_{IC}) and T_{TOF}, different methods can be applied. In the present work two methods are discussed.

The first method consists in the determination of both time marks as a position of the center-of-gravity of signals from the cathode of the IC and anode of the neutron detector. The time mark for the cathode is obtained by deriving the increasing part of the signal function (see Fig.4.12).

First of all the maximum of the derived function for the increasing part of the

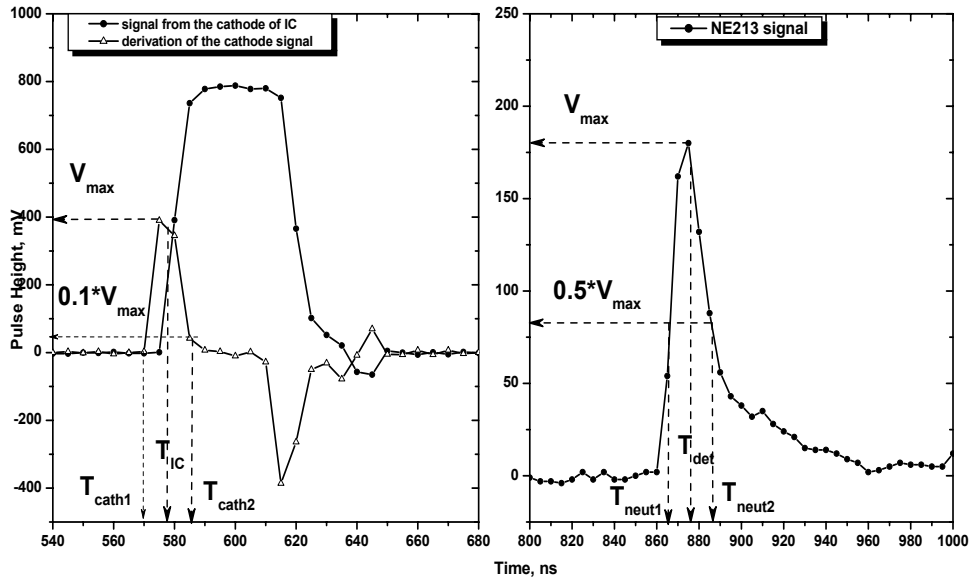

Figure 4.12: Determination of the "start" (left) and "stop" (right) time-marks needed for the TOF spectrum calculations using the first method.

cathode signal and its position should be determined. Then two points (T_{cath1} and T_{cath2}) corresponding to the positions of the values less or equal than $0.1 \cdot V_{max}$ are found. Finally, T_{IC} represents the center-of-gravity position of the derived curve between the points T_{cath1} and T_{cath2} calculated by:

$$T_{IC} = \frac{\sum_i N_i t_i}{\sum_i N_i}, \tag{4.7}$$

where i=(T_{cath1}, T_{cath2}).

A similar procedure is applied for the detector pulse (see Fig.4.12). After the determination of the maximum of the signal V_{max} as well as T_{neut1} and T_{neut2} that correspond to the positions for the values less or equal than $0.5 \cdot V_{max}$, the

time mark for the detector pulse T_{det} is determined as the center-of-gravity of the signal between T_{neut1} and T_{neut2}:

$$T_{det} = \frac{\sum_i N_i t_i}{\sum_i N_i}, \tag{4.8}$$

where i=(T_{neut1}, T_{neut2}).

The choice of the value $0.5 \cdot V_{max}$ instead of $0.1 \cdot V_{max}$ for the cathode signal lets us to determine T_{det} correctly as the detector signal shape is different for different incident particles (see Fig.4.8) and T_{det} can not be determined as the center-of-gravity of the signal.

Once T_{IC} and T_{det} are known the T_{TOF} can be obtained as:

$$T_{TOF} = w \cdot \frac{T_{det} - T_{IC}}{\triangle t}, \tag{4.9}$$

where $\triangle$t=1 ns is the step in time scale; w=5ns is the width of the WFD channel. The time resolution of γ-peak from this method is 2.76 $\pm$ 0.06 ns (see Fig.4.13a).

Fig.4.13b presents the TOF spectrum obtained applying another method that is more precise in the time mark determination. One could see that the quality of the time marks determination is very important. During the transformation of the analogue signal into the digital one, with WFD channel width of 5 ns /channel, fluctuations of the signal writing in 1-2 channels can appear. After using the first method of the time mark determination one could observe fluctuations in the TOF spectrum (see Fig.4.14). The frequency of these fluctuations is about 5 ns that corresponds to the WFD channel width. So, another method can be used in order to determine the "start" and "stop" marks for the TOF spectrum determination.

A second method of time mark determination uses the correlation between the reference signal and the experimental signal from the detector [Kor03]. Examples of both reference signals taken with the oscilloscope are presented in Fig.4.15.

The experimental waveform was separated into 2 arrays that were analyzed separately : one array - for the cathode signal, and a second one for the detector pulse. In order to be able to apply the correlation procedure, both experimental and standard waveforms should have the same time scale. So, the experimental

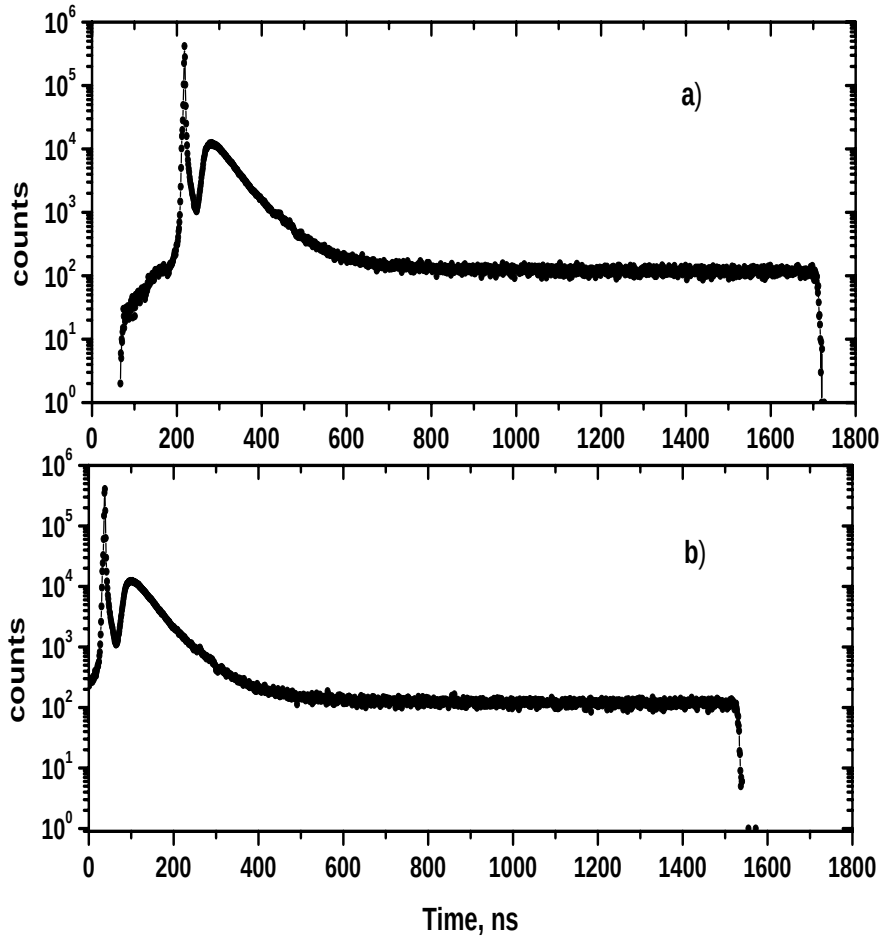

Figure 4.13: TOF spectrum obtained from the 2 methods of the time mark determination: a) - time marks are determined by the center-of-gravity of the cathode and neutron detector signals; b) - time marks are determined by use of the correlation function.

waveform (5 ns channel width) and the signal from the oscilloscope (0.2 ns channel width) were transformed into waveforms with 0.5 ns channel width. Then, the correlation analysis can be performed

$$Corr(T) = \int S(T - T^{'})N(T^{'})dT^{'}, \tag{4.10}$$

where Corr(T) is the resulting correlation function; S(T) is the "standard"

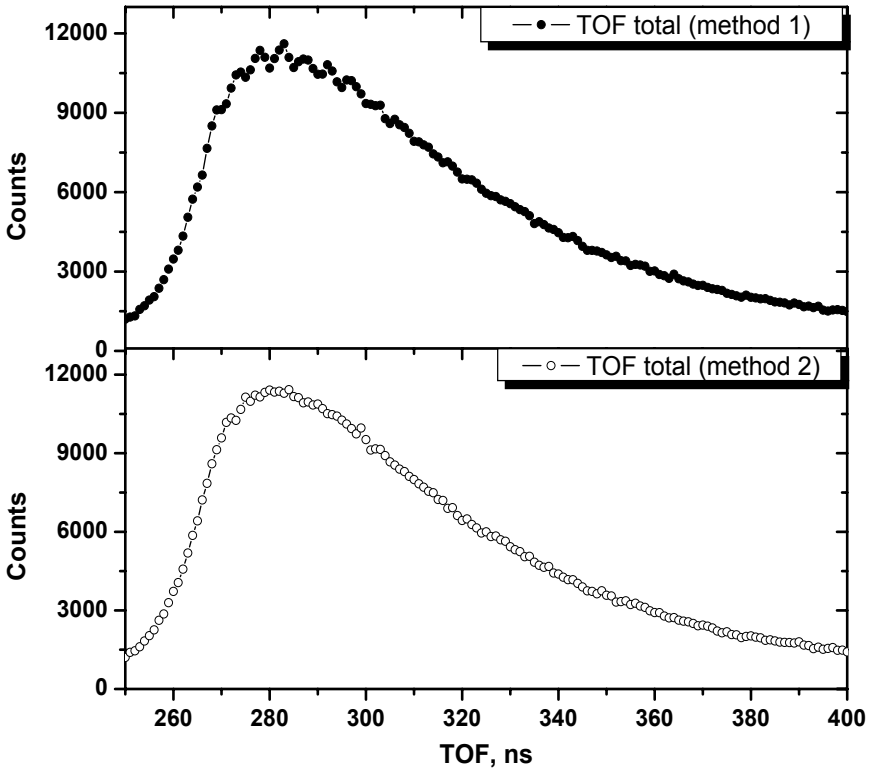

Figure 4.14: The time-of-flight spectra obtained by the use of 2 methods of the time mark determination: the center-of-gravity of the cathode and neutron detector signals (method 1) and the correlation of these signals with the reference ones (method 2).

signal; N(T) is the experimental waveform. Examples of the experimental waveforms for the cathode and detector pulses as well as the resulting correlation function for these signals for one event are presented in Fig.4.16. In order to find the maximum of the correlation function a parabola fit is applied in the region of the maximum. The positions of the maximum of the parabolic fit correspond to the position of T_{IC} and T_{det} in ns time scale.

Then, the time-of-flight is calculated as:

$$T_{TOF} = \frac{T_{det} - T_{IC}}{\triangle t}, \tag{4.11}$$

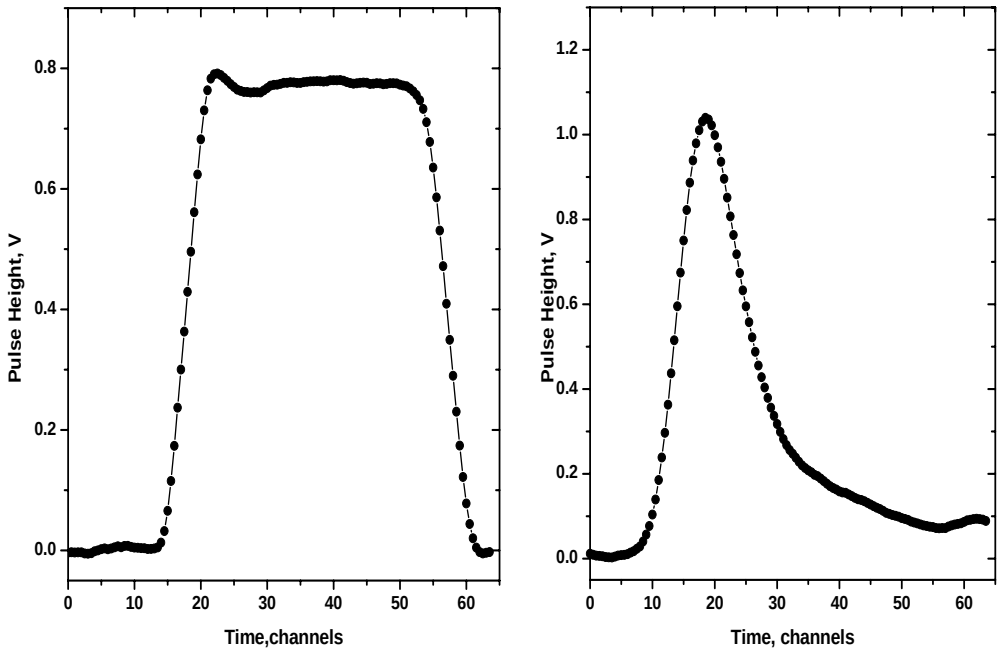

Figure 4.15: The examples of the reference signals registered with the oscilloscope from the cathode of the ionization chamber (left) and from the neutron detector (right).

where $\triangle$t=1 ns. The time resolution of the spectra obtained by this method is 2.75 +/- 0.08 ns. One can see that the difference in time resolution for the TOF spectra obtained by 2 different methods for the time mark determination is rather small in the case of this type of WFD working with the 200 MHz frequency. One can mention that the second method gives better time resolution while using the WFD working with higher frequency. Unfortunately, the second method is more CPU time consuming. However, it is possible to reduce the analysis time by separating the fission fragment events in coincidence with only neutrons in separate files and then to analyse these files only. The procedure of the coincidence events (fission fragments plus neutrons only) selection is given in

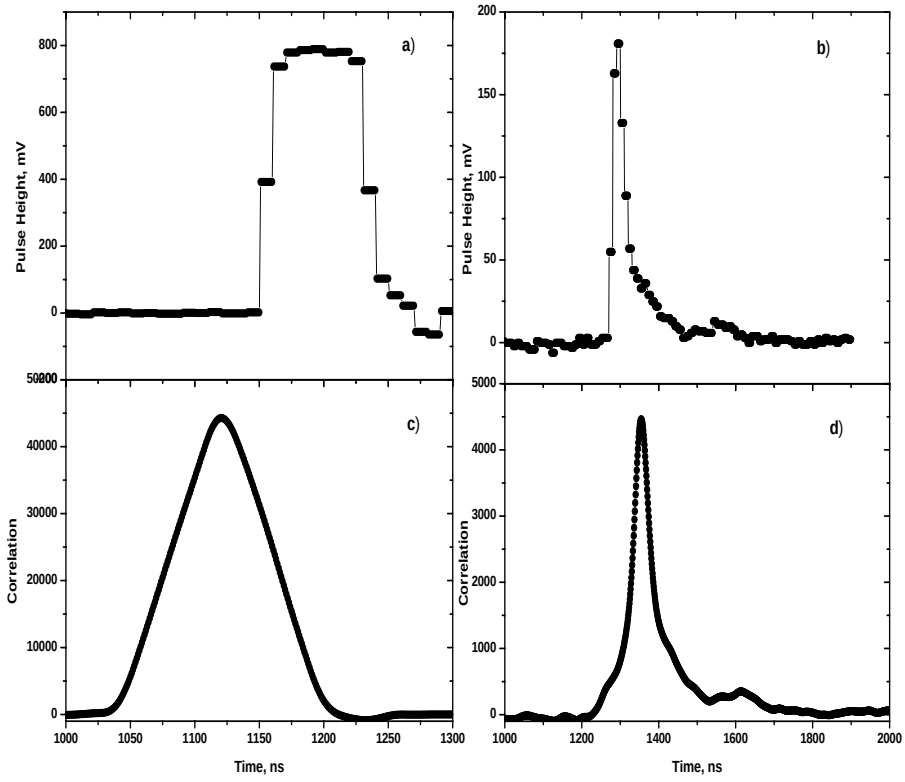

Figure 4.16: Examples of the resulting correlation functions ((c) and (d)) for the experimental waveforms of the cathode signal from IC (a) and the detector signal (b).

the following paragraph.

4.2.4 Neutron Selection

In order to make the analysis of the fission fragments in coincidence with neutrons, the proper selection of the neutron events should be done. First of all, all events with TOF greater than the TOF of the prompt γ are selected. But this selection is not sufficient as can be seen in the Fig.4.17.

The delayed γ's from fission and the correlated background events (inelastic

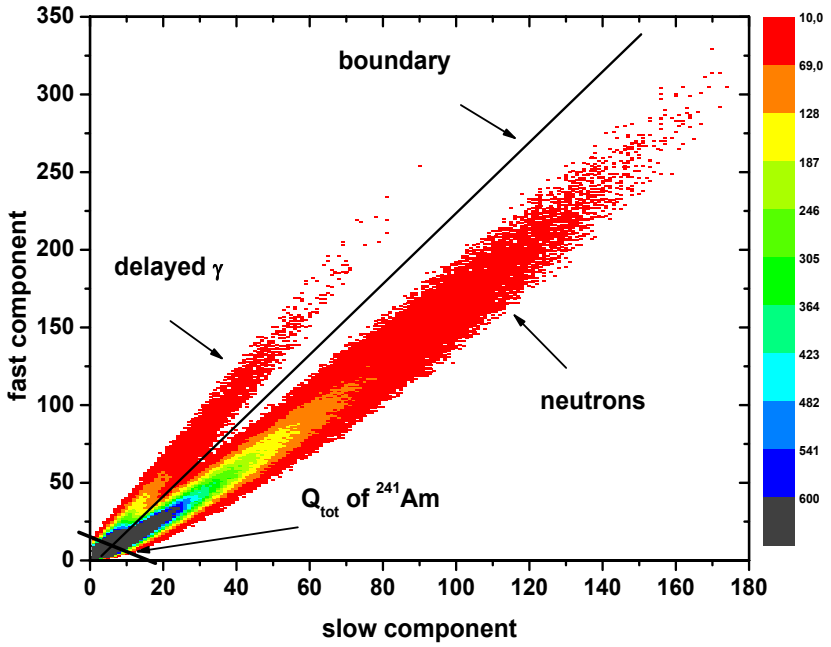

Figure 4.17: Discrimination between neutrons / γ's after the elimination of the prompt γ's.

scattering on ^{12}C(n,n$'$) of the scintillator material) can arrive in the same time as the neutrons emitted from the fission event. Such events should be eliminated. It can be done by applying the PSD method described above. It is possible to determine the boundary between the neutrons and delayed γ's plus correlated background as shown in Fig.4.17. Unfortunately, the separation between neutrons and delayed γ's in the region of small Q_{tot} is rather difficult. It was therefore decided to remove the events with Q_{tot} less than Q_{tot} of ^{241}Am (Eγ=59.54 keV) from the analysis. The TOF spectra for the selected neutrons as well as for the delayed γ's are presented in Fig.4.18. On this figure one can see that the background contribution in the neutron TOF spectrum is very low. So, one can say that the method used for the neutron selection permits both a proper selection of the neutron events and a reduction of the background. The remaining correlated

background will be removed during the neutron energy calculations. After applying all conditions for the neutron separation, the analysis of the neutron events can be performed, i.e. the prompt neutron energy spectrum and the detector efficiency can be determined.

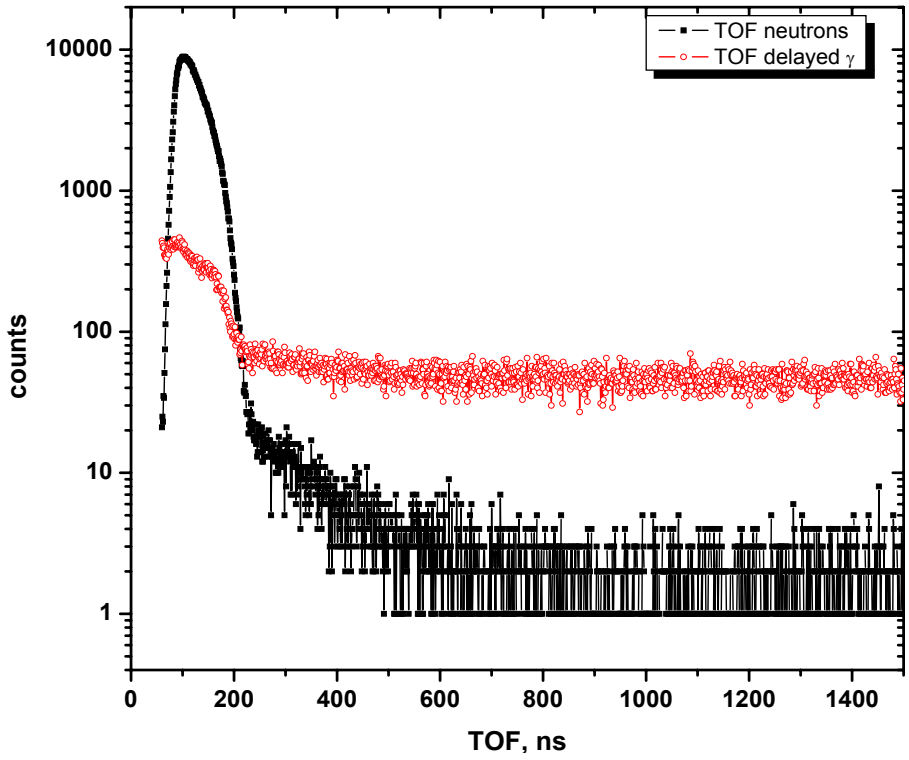

Figure 4.18: The neutron and delayed γ time-of-flight spectra.

4.3 Neutron Energy Spectrum

After the selection of the neutron events, the prompt neutron energy spectrum can be calculated. The energy distribution is obtained using the Time-of-Flight technique. Knowing the distance between the fission source and the neutron detector (l=1.47 m) that was covered by the neutron during the time t one can determine its velocity $v = l/t$. Then the kinetic energy of the particle can be calculated in relativistic treatment:

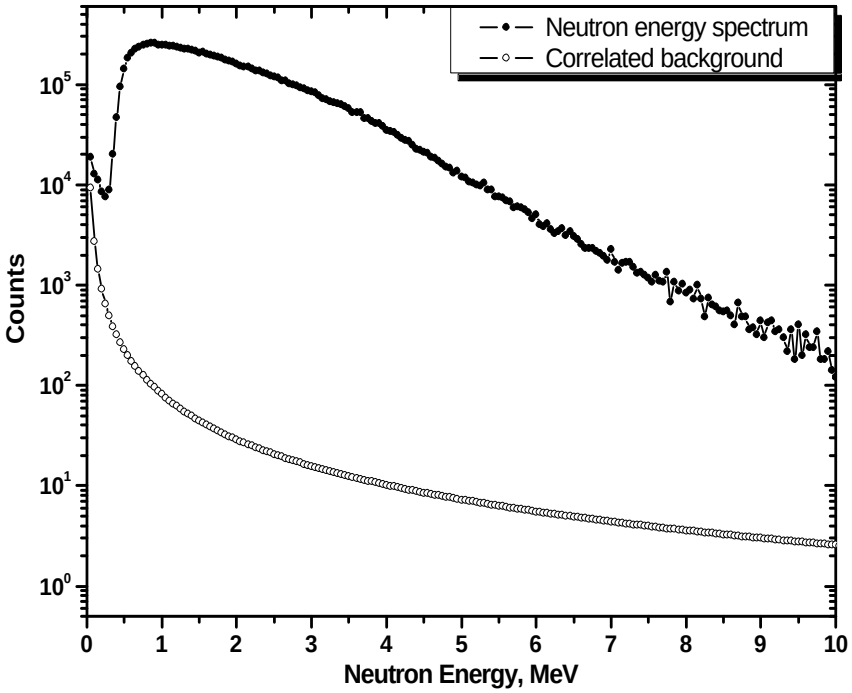

Figure 4.19: The neutron energy spectrum in laboratory system (not corrected for the detector efficiency) and the background as a function of the neutron energy.

$$E_k = m_0c^2(\frac{1}{\sqrt{1-\beta^2}} - 1), \tag{4.12}$$

where $\beta = v/c$. The resulting neutron energy spectrum is presented in Fig.4.19. This energy spectrum is not corrected for the detector efficiency and the correlated background that was not removed completely.

The correlated background Φ(TOF) is constant in the time scale but it has different behavior in the energy scale. If we transform Φ(TOF) in the energy scale as:

$$\Phi(E_n) = \Phi(TOF) \cdot \frac{dT}{dE_n}, \tag{4.13}$$

and then plot in E_n scale (see Fig.4.19), one can see that the correlated background is not negligible in the region of small E_n. So, $\Phi(E_n)$ should be extracted from the neutron energy spectrum in order to determine the experimental detector efficiency.

4.4 Neutron Detector Efficiency

4.4.1 Experimental Determination

The detector efficiency can be determined by comparing the experimental neutron energy spectrum to the evaluation performed by Mannhart [Man87]. Usually, the fission neutron energy spectrum for ^{252}Cf is represented by the Maxwellian shape:

$$Maxw(E) = \frac{2}{\sqrt{\pi}T}\sqrt{E} \cdot e^{-E/T}, \tag{4.14}$$

with T=1.42 MeV, the temperature of the Maxwellian distribution.

Nevertheless, it was shown by Mannhart [Man87] that a deviation of the experimental fission neutron spectrum of ^{252}Cf exists compared to this Maxwellian shape as shown in Fig.4.20. In this figure the ratio between the Mannhart evaluation and the Maxwellian spectrum is plotted. Taking into account this Mannhart evaluation, the detector efficiency is now given by:

$$\epsilon(E) = \frac{N_d(E)}{N_f \cdot M(E) \cdot \overline{\nu} \cdot \frac{\omega}{4\pi}}, \tag{4.15}$$

where

ϵ(E) - detector efficiency as a function of the neutron energy;
M(E) - Mannhart evaluation as a function of the neutron energy;
N_d(E) - experimental neutron energy spectrum;
N_f - number of the fission events detected during the experiment;
$\omega/\ 4\pi$ - the detector solid angle (in our experiment $\omega/\ 4\pi$=0.064%);

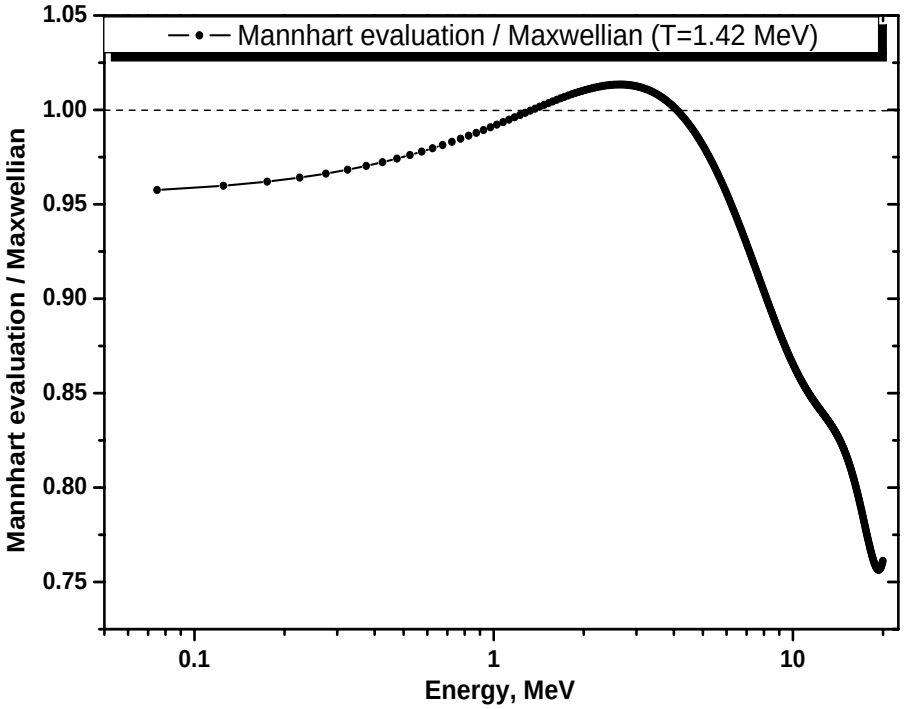

Figure 4.20: Evaluated data of the ^{252}Cf neutron spectrum.

$\overline{\nu}$ - the average neutron multiplicity ($\overline{\nu}$=3.767).

4.4.2 Simulation

Once parameters of the experimental resolution of NE213 were inferred (see section 4.1), the neutron detection efficiency was simulated using the NEFF4 code (Ref. [Die82]) and compared to the experimental efficiency (see Fig. 4.21). The NEFF4 code is a Monte Carlo code dedicated to the calculation of the detection efficiency of NE213 scintillation detectors for fast neutrons in the energy range from 0.02 MeV to 20 MeV. Fig. 4.21 shows the difference in the efficiency curves above E_n=3 MeV. It is due to the rejection of the saturated pulses above 2V (see paragraph 4.2.1), which reduces the experimental efficiency above this energy.

As mentioned before, the saturated pulses are caused by the WFD characteristics. These pulses can be seen in Fig.4.2 in the region of 2V on the pulse height scale. If we calculate the proton recoil energy that corresponds to the light output of the saturated events (using the equations 4.2 and 4.4), one can see that E_p is equal to 3 MeV. So, by rejecting the saturated events in the off-line analysis we reduce the intrinsic efficiency of the neutron detector. Unfortunately, such events can not be used in the analysis unless the procedure of the signal shape reconstruction can be applied (see Ref. [Kor03]).

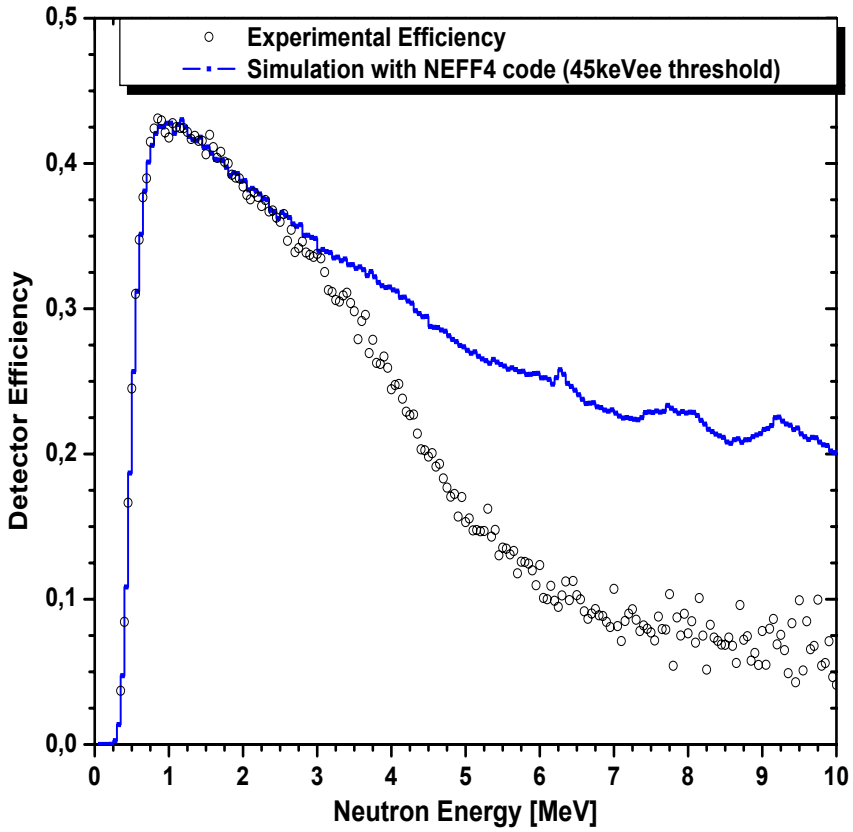

Figure 4.21: Comparison of the experimental and theoretical detector efficiency.

Chapter 5

Fission Fragments in Coincidence with Neutrons

This section describes the fission fragments analysis in coincidence with emitted prompt neutrons. The resulting fission fragment mass, kinetic energy and total kinetic energy distributions for the ^{252}Cf(sf) are presented. After the analysis of the coincidence events, series by series, one could see a very good stability (see Fig. 5.1). The average counting rate is 0.13 neutrons /sec. The analysis of the fission fragments in coincidence with prompt neutrons is similar to the one described in Chapter 3. All above described corrections to the anode pulse have to be applied. The center-of-gravity and angular distributions of the fission fragments in coincidence with the emitted prompt neutrons are obtained and discussed.

5.1 Mass and Energy Distributions

As already mentioned, during the experiment one can measure only the post-neutron properties such as the post-neutron fragment energy. It was shown that this characteristic can be found from the anode pulse height. Then, from the post-neutron energy and mass, one can infer the pre-neutron fragment mass and energy.

First of all, the proper separation of the fission fragment events in coincidence with prompt neutrons only was done using the time-of-flight and pulse shape

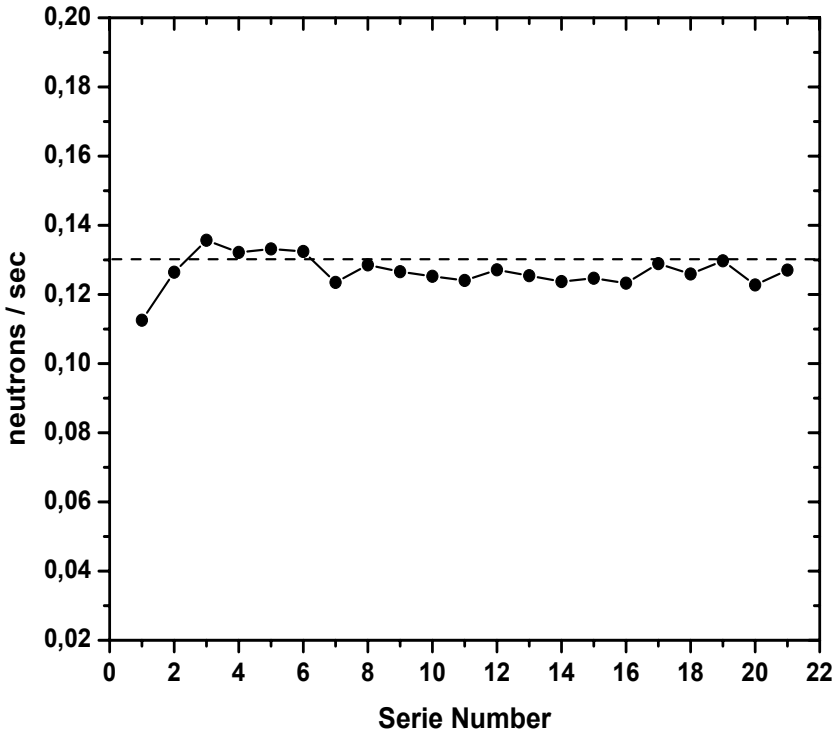

Figure 5.1: The number of the coincidence events (fission fragments in coincidence with only neutrons) acquired by LabView (0.13 neutrons /sec).

discrimination techniques (see Chapter 4). Then the fission fragment events were analysed. The anode pulse was corrected for the grid inefficiency, "ballistic" effect and the real anode pulse height was determined (see Chapter 3). The next step is the calculation of the fission fragment emission angle.

5.1.1 Kinematics of the reaction

Fission fragment angular distributions were obtained from the center-of-gravity distributions using the procedure described in Chapter 3. The resulting 2-dimensional distributions of the cosine of the fragment emission angle versus anode pulse

height for backing and sample sides are presented in Fig.5.2. One-dimensional angular distributions for backing and sample sides are given in Fig.5.3.

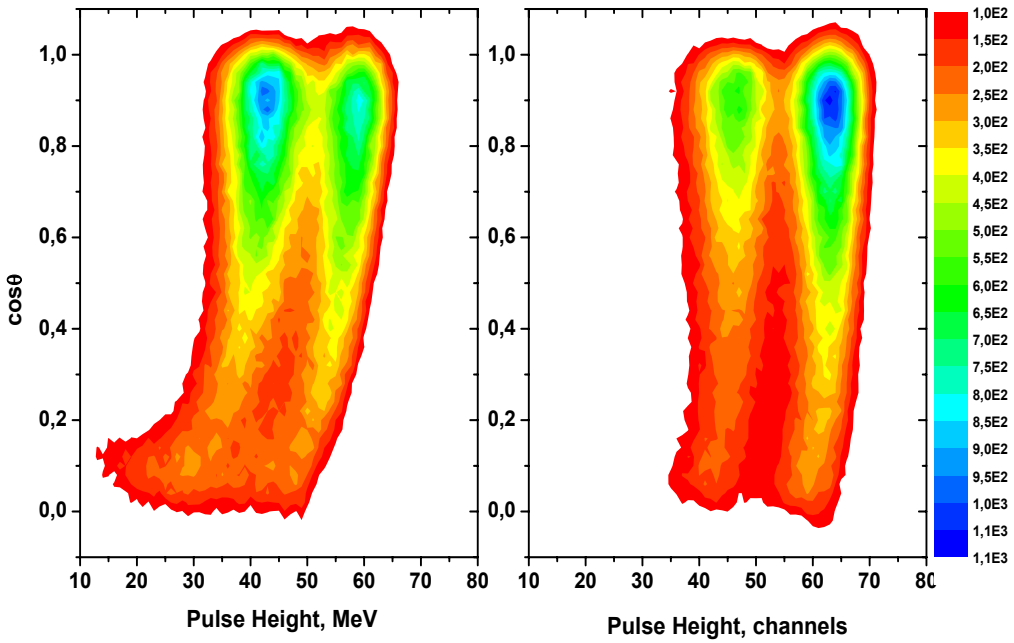

Figure 5.2: The resulting two-dimensional distributions of the cosine of the fission fragment emission angle versus the pulse height for backing (a) and sample (b) sides. The distributions are obtained for the fission fragments in coincidence with emitted prompt neutrons.

Comparing these angular distributions with the ones obtained for the fission fragments without the coincidence with emitted prompt neutrons, one can see a peak close to $\theta \sim 0^0$ not observed in Fig.3.13. This can be explained by:

- the kinematics of the neutron evaporation process, i.e. neutrons are emitted mainly in the fission fragment motion direction;

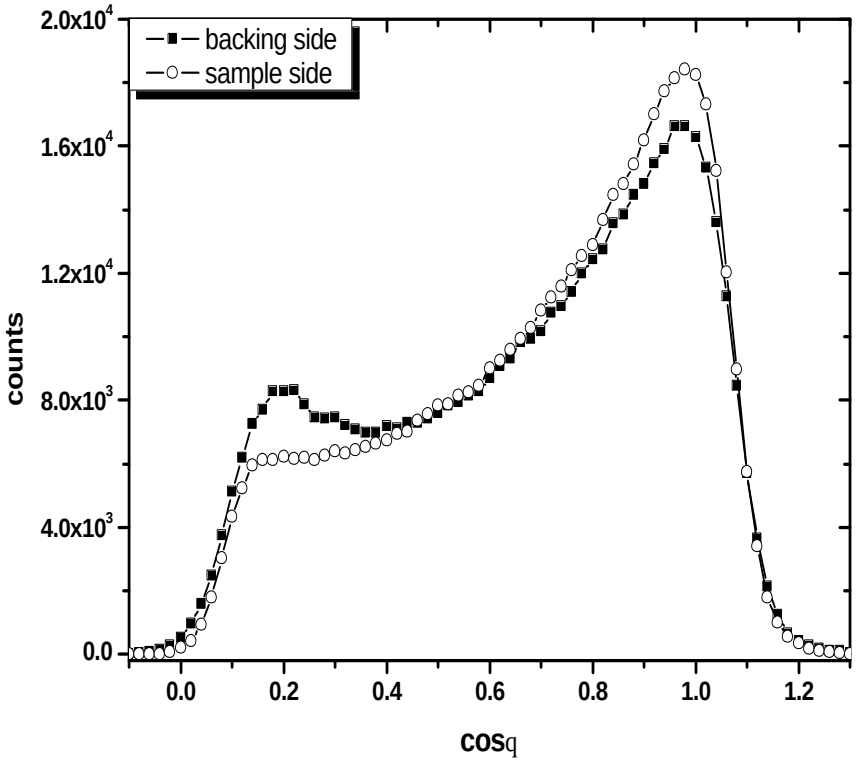

Figure 5.3: One-dimensional angular distributions of the fission fragments in coincidence with emitted prompt neutrons.

- the geometry of the experiment: our neutron detector was placed in the axis of the ionization chamber, so it detected more neutrons coming from the fragments that have been emitted with a small angle θ.

Then the fragment energy (in MeV) can be found from the anode pulse (in WFD channels) using the procedure described in Chapter 3.

5.1.2 Fragment Mass and Energy Distributions

Using the same analysis procedure as in Chapter 3, the anode pulse height should be corrected for the fragment energy loss in the target backing and sample. Then

this corrected anode pulse height was transformed into the fragment post-neutron kinetic energy. The pre-neutron masses and energies were then calculated from the post-neutron energies E_1 and E_2, where indices 1 and 2 correspond to the two parts of the ionization chamber (backing and sample, respectively) using the following procedure.

The iteration procedure of the fragment mass and energy determination in case of the coincidence of the fission fragments with emitted prompt neutrons is similar to the one described in Chapter 3. Hence, in the case of a neutron emission it is necessary to take into account the recoil correction of the pre-neutron energies (see Ref. [Gav74]).

The initial estimates of mass were done by assuming $m_1^*=m_2^*=126$ amu (for ^{252}Cf). The star superscript designates fission fragment characteristics before neutron emission. Let us also assume that $E_1^*=E_1$ and $E_2^*=E_2$ for the first iteration. Then the post-neutron mass can be determined as $m_i=m_i^*$ - $\overline{\nu}(m_i^*)$, where $\overline{\nu}(m_i^*)$ are the literature values for the average neutron multiplicity as a function of a pre-neutron fragment mass (see Ref. [Bud88]). The experimental post-neutron energies have to be corrected for the Pulse Height Defect (PHD) that is calculated as explained in Annexe A:

$$E_i^{corr} = E_i + PHD(m_i). \tag{5.1}$$

After the correction of the post-neutron energy for the PHD, the pre-neutron energy can be calculated by taking into account the recoil correction (see Ref. [Gav74]):

$$E_i^* = [1 + \frac{\overline{\nu}(m_i^*)}{m_i^*}] \cdot E_i^{corr} + 2E_i^{corr} \cdot [\frac{V_n cos\theta}{V_{FF}^*} - 1]\frac{1}{m_i^*}. \tag{5.2}$$

Fragment and neutron velocities (V_{FF}^*, V_n) can be obtained from the well-known equations:

$$E_{FF}^* = \frac{1}{2}m^* V_{ff}^{*2}, \tag{5.3}$$

$$E_n = \frac{1}{2} m_n V_n^2. \tag{5.4}$$

By simple substitution of V_{ff}^*, V_n from eqs. (5.3 - 5.4) into eq. (5.2) one finally obtains the pre-neutron fragment energy:

$$E_i^* = [1 + \frac{\overline{\nu}(m_i^*)}{m_i^*}] \cdot E^{corr} + 2E^{corr} \cdot [\sqrt{\frac{m_i^* E_n}{E_i^*}} cos\theta - 1] \frac{1}{m_i^*}. \tag{5.5}$$

From the pre-neutron energy E_i^* and the mass of the compound nucleus A, one can calculate the pre-neutron mass as:

$$m_1^* = A \cdot \frac{E_2^*}{E_1^* + E_2^*}, \tag{5.6}$$

$$m_2^* = A \cdot \frac{E_1^*}{E_1^* + E_2^*}. \tag{5.7}$$

From this point the procedure is repeated with new m_i^* and E_i^* values, with i=1,2. The values m_i^* from the last iteration are compared to the prior values of m_i^* until convergence within 1/8 amu.

The resulting distributions of the pre- and post-neutron fragment masses and energies are presented in Fig.5.4. From the distribution of the pre-neutron mass yields one can observe the asymmetry between the light and heavy fragment peaks. For example, from the distribution of the fragment mass yields for the sample side of the target one can see that the majority of the detected fission fragments are the light fragments. This difference in yields for light and heavy fragments does not exist for the fission fragments without the coincidence with neutrons (see Fig.3.19). This difference in mass yields can be explained by:

- kinematics of the neutron evaporation process;

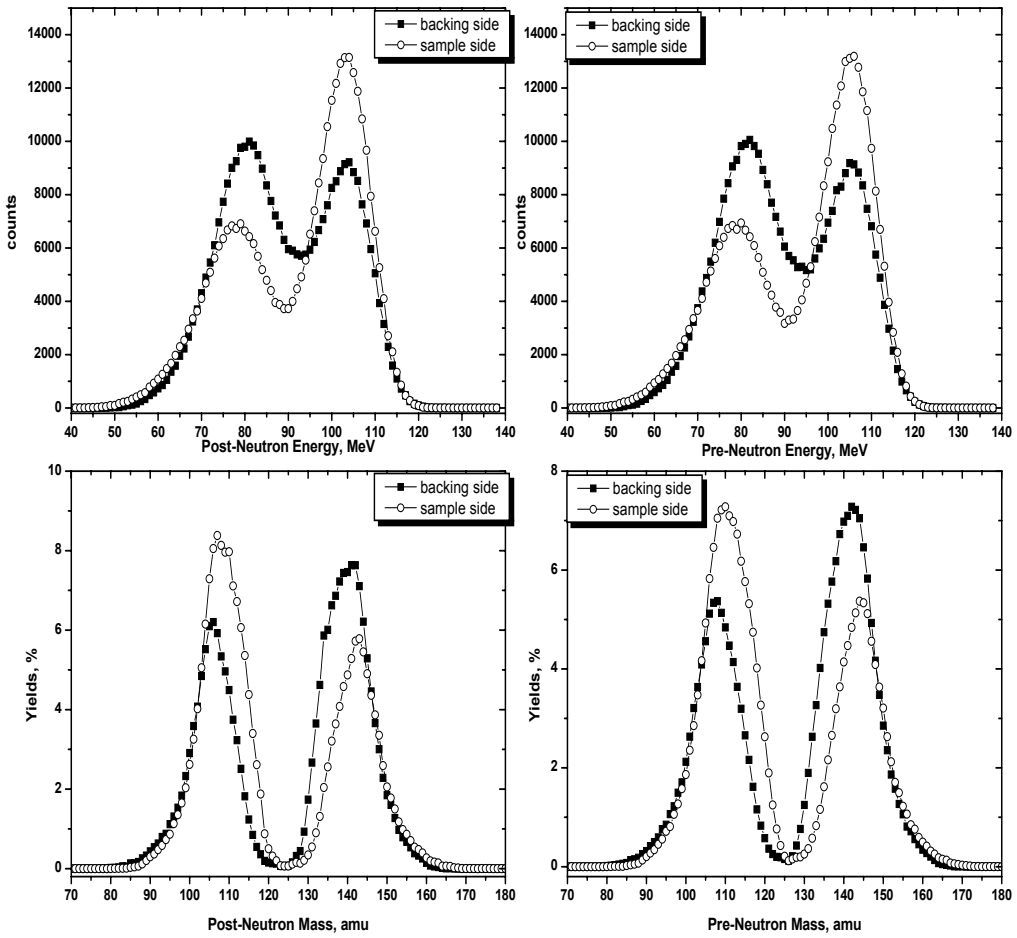

Figure 5.4: Fission fragment pre- and post-neutron mass and kinetic energy distributions in coincidence with neutrons.

- and the difference in $\overline{\nu_L}$ and $\overline{\nu_H}$.

According to Ref.[Kal05] the average neutron multiplicity for light fragments, $\overline{\nu}_L$=1.71, represents 54.3 % of the total prompt neutron multiplicity, $\overline{\nu_{tot}}$=3.74. Comparing the mass yields obtained in this work in the light peak Y_L with the total yields Y_{tot} of the fission fragment in coincidence with neutrons, one obtains $\frac{Y_L}{Y_{tot}}$=(59.3 $\pm$0.28) % .

5.2 Center-of-Mass Neutron Energy Distribution

From the kinematics of the neutron emission from the fully accelerated fragments (Fig.5.5) and from the known laboratory system quantities ($V_{FF}^{lab}, V_n^{lab}, cos\theta^{lab}$) one can find the neutron center-of-mass velocity V_{cm}:

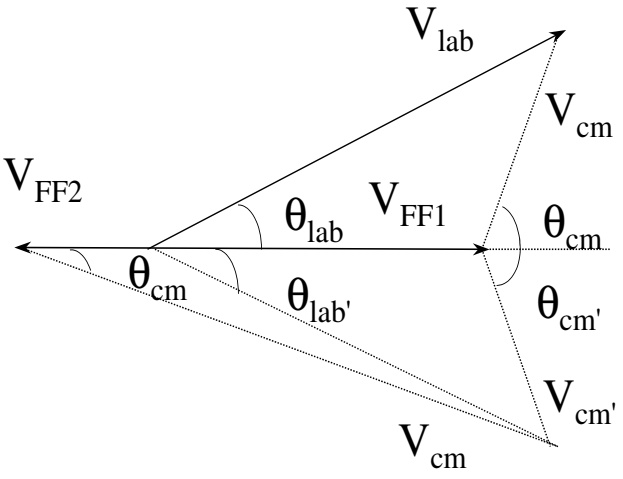

Figure 5.5: Schematic representation of neutron emission from the fully accelerated fragments in both the center-of-mass and laboratory systems.

$$V_{cm}^2 = V_{FFlab}^2 + V_{nlab}^2 - 2 \cdot V_{FF}^{lab} V_n^{lab} cos\theta^{lab}, \tag{5.8}$$

where V_n^{lab}, V_{FF}^{lab}, θ^{lab} are the neutron and fragment velocities and the neutron emission angle, respectively, in the laboratory system. As soon as we know the

fragment and the neutron energies and masses in the laboratory system, the equation 5.8 can be expressed as:

$$E_n^{cm} = \frac{E_{FF}^{lab}}{M_{FF}^{lab}} + E_n^{lab} - 2E_n^{lab}\sqrt{\frac{E_{FF}^{lab}}{E_n^{lab}M_{FF}^{lab}}} \cdot cos\theta^{lab} \tag{5.9}$$

According to standard nuclear evaporation theory the center-of-mass energy spectrum corresponding to a fixed residual nuclear temperature T is given as (Ref.[Wei37]):

$$\Phi(E_n^{cm}) = \frac{E_n^{cm}}{T} \cdot exp(-E_n^{cm}/T). \tag{5.10}$$

Then the evaporation spectrum for neutrons emitted in a cascade process was expressed by [LeC59]:

$$\Phi(E_n^{cm}) = const \cdot (E_n^{cm})^{\lambda} \cdot exp(-E_n^{cm}/T_{eff}). \tag{5.11}$$

We have fitted the obtained center-of-mass neutron energy spectrum (integrated over all fission fragments) with Eq.5.11 where the parameters λ and the effective temperature T_{eff} were two free parameters (see Fig. 5.6). We obtained values λ=0.379±0.005 and T_{eff}=0.966±0.006 MeV. Here, the given uncertainties are only statistical errors. The obtained parameter λ is in very good agreement with the one determined by Budtz-Jørgensen [Bud88] (λ=0.38). While the value of the effective temperature is reasonably good agreement with the one given in [Bud88] (T_{eff}=1.07 MeV). In additional, from this spectrum we obtained the average neutron energy $\overline{E_n}$=2.15 MeV

5.3 Neutron Multiplicity

Another aim of this work was also to show that the procedure used for the neutron analysis allows a good determination of the average prompt neutron multiplicity

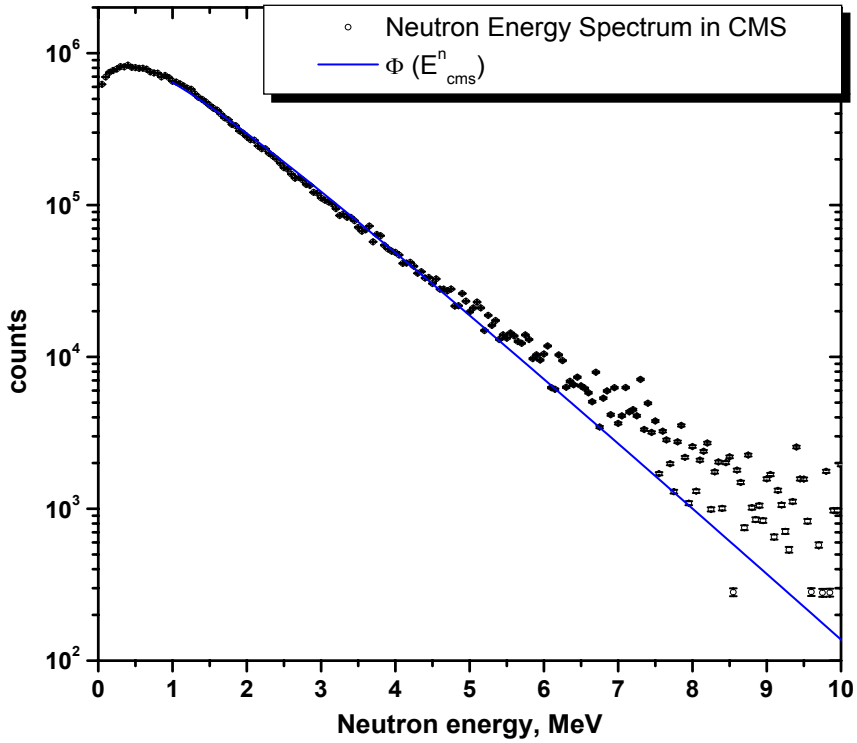

Figure 5.6: Fission neutron energy spectrum in the center-of-mass system (indicated errors are due to the statistics).

as a function of the fragment mass. This neutron multiplicity can be determined as (see Ref.[Gav74]):

$$\overline{\nu}(m_1^*, TKE_1^*) = \frac{4\pi}{N_T(m_1^*, TKE_1^*) \cdot \omega} \times \sum_{V_n^{lab}} \frac{N_1(m_1^*, TKE_1^*, V_n^{lab}) \cdot V_n^{cm} \cdot (V_n^{lab} - V_{FF} cos\theta)}{\epsilon(V_n^{lab}) \cdot V_n^2}, \tag{5.12}$$

where

$N_T(m_1^*, TKE_1^*)$ - the total number of the fission fragment events at the given pre-neutron mass and kinetic energy;

$N_1(m_1^*, TKE_1^*, V_n^{lab})$ - the number of the fission fragment events for which the

neutron velocity V_n^{lab} was detected;
θ - the neutron emission angle;
V_{FF} - the fission fragment velocity;
V_n^{cm} - the neutron velocity in the fragment center-of-mass frame;
$\epsilon(V_n^{lab})$ - the detector efficiency as a function of the neutron velocity V_n^{lab};
$\omega/4\ \pi$ - the solid angle of the neutron detection system.

By simple substitution of velocities by energies one obtains:

$$\overline{\nu}(m_1^*, TKE_1^*) = \frac{4\pi}{N_T(m_1^*, TKE_1^*)\omega} \times \sum_{E_n^{lab}} \frac{N_1(m_1^*, TKE_1^*, E_n)\sqrt{2E_n^{cm}}(\sqrt{2E_n^{lab}} - \sqrt{\frac{2E_{FF}}{m_1^*}}cos\theta)}{2 \cdot \epsilon(E_n^{lab}) \cdot E_n^{lab}}. \quad (5.13)$$

The neutron energy in the laboratory system was transformed into the the center-of-mass system as explained in paragraph 5.2 and in Ref.[Bud88]. Figure 5.7 illustrates the resulting average prompt neutron multiplicity for ^{252}Cf(sf) as a function of the pre-neutron fragment mass obtained by use of the digital technique. These data start from M=80 amu up to M=180 amu. Comparing the obtained values to the well-known literature values one observes only small differences with the data from Budtz-Jørgensen (see Ref.[Bud88]) and larger differences with the data of Bowman (see Ref.[Bow62]).

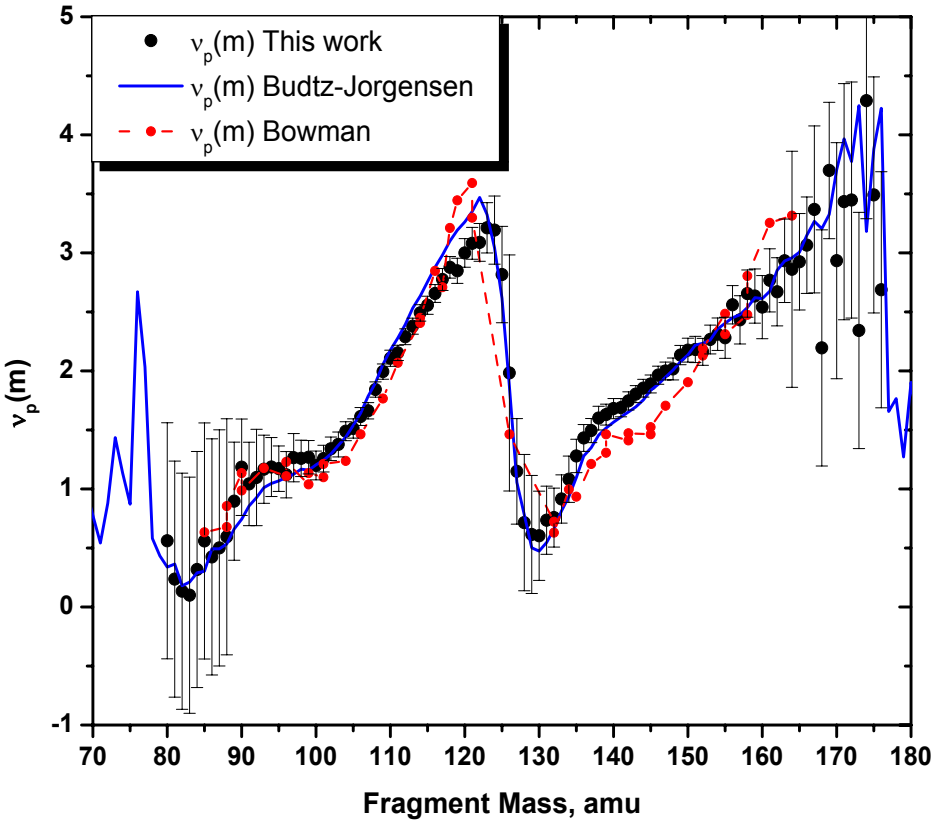

Figure 5.7: Comparison of the average neutron multiplicity obtained in this work with literature data (Ref.[Bud88], Ref.[Bow62]).

Chapter 6

Conclusions

In this work the successful application of the digital technique to nuclear experiments was demonstrated. This technique was successfully applied to the determination of the fission fragment and prompt neutron characteristics in the case of spontaneous fission of ^{252}Cf.

The digital technique presents several advantages compared to the more traditional analogue technique:

1. it is possible to simplify the traditional analogue experimental set-up with separate units used for the separation and storage of the experimental data;

2. all necessary information on the fission fragment and prompt neutrons properties can be determined from the digitalized pulses of the fission fragment and neutron detectors. Different methods for the off-line analysis of the digitalized pulses can be applied in order to extract the necessary information;

3. the choice of the off-line analysis methods is limited only by the imagination of the scientist;

4. it is possible to develop a special procedure for the correction of the pile-up affected pulses that will permit to keep such pulses in the analysis, i.e. in order to increase statistics and to get a reliable pulse height determination;

Using the digital technique we were able to:

1. determine the grid inefficiency of the meshed grid directly from the anode signal of the ionization chamber;

2. reconstruct the well-known literature values for the ^{252}Cf(sf) such as energy distributions, mass yields, prompt neutron energy spectra in the laboratory and center-of-mass systems and the average prompt neutron multiplicity as a function of the fragment mass;

3. obtain a reasonably good n-γ separation using the pulse shape analysis;

4. obtain time resolution for the TOF spectrum smaller than the WFD channel width by sending the signals from the cathode of the IC and the neutron detector to one channel of WFD;

So, this technique seems to be appropriate for the studies of the fission fragment and prompt neutron characteristics for ^{252}Cf(sf) and can be also used for the investigations of the prompt neutron multiplicity fluctuations in the resonance energy region for ^{239}Pu. Nevertheless, it requires that the problem of the too high dead time (mainly due to the LabView software) should be solved.

References

[Bar04] L. Bardelli, et al., *Nucl. Phys.* **A521** (2004) 480. 4

[Bar85] G. Barreau, et al., *Nucl. Phys.* **A432** (1985) 411-420. 52, 53, 54, 55

[Bat04] O. A. Batenkov, et al., *Proc. Int. Conf. on Nucear Data for Science and Technnology (ND2004), Santa Fe, 2004, Eds. R.C. Haight et al., p.1003.* 4

[Bon03] U. Bonnes, J. Foh, CSTA2HV, 7.12.1998, IKP, TU Darmstadt, D-64289 Darmstadt, private communication. 17

[Bow62] H.R. Bowman, S.-G. Thompson, J.C.D. Milton, W.J. Swiatecki, *Phys. Rev.* **126** (1962) 2120. 92, 93, 106

[Bud87] C. Budtz-Jørgensen, H.-H. Knitter, Ch. Straede, F.-J. Hambsch and R. Vogt, *Nucl. Instr. and Meth.* **A258** (1987) 209. 7, 9, 10, 34, 36, 47, 52

[Bud88] C. Budtz-Jørgensen, H.-H. Knitter, *Nucl. Phys.* **A490** (1988) 307-328. 49, 55, 86, 90, 92, 93, 106

[Bun49] O. Bunemann, T.E. Cranshaw, J.A. Harvey, *Can. Jour. of Res.* **A27** (1949) 191. 9, 29

[Dem98] L. Demattè, et al., *Conf.on Dynamical Aspects of Nuclear Fission, Casta Papiernicka, Slovakia, 19-23 October 1998.* 4, 34

[Dem02] L. Demattè, F.-J. Hambsch, H. Bax, *Nucl. Instr. and Meth.* **A480** (2002) 706-712. 3, 4, 34

[Die82] G. Dietze, H. Klein, *"Neutron Response Functions and Detection Efficiencies for NE213 Scintillation Detectors*, PTB-ND-22 (1982). 80

[Fast] http://fastcomtec.com. 14

[Fre74] J. Frehaut, D. Shackleton , *Symp. on Physics and Chemistry of Fission* **vol.II** (1974) 201. 3

[Gav74] A. Gavron, *Nucl. Instr. and Meth.* **115** (1974) 93-98. 86, 91

[Gon91] F. Goennenwein, *"The Nuclear Fission Process", ed. C.Wagemans (CRC Press, Boca Raton)* (1991) 323. 50, 51, 52

[Hai66] E.L. Haiene,A.B. Witehead , *Rev. Sci. Instr.* **37** (1966) 190.

[Ham95] F.-J. Hambsch, J. Van Aarle , R. Vogt , *Nucl. Instr. and Meth.* **A361** (1995) 257. 8, 47

[Ham97] F.-J. Hambsch, S. Oberstedt , *Nucl. Phys.* **A617** (1997) 347-355. 53, 55

[Ham99] F.-J. Hambsch, H.-H. Knitter , C. Budtz-Jørgensen and J. P. Theobald, *Nucl. Phys.* **A491** (1999) 56. 3

[Jam04] F. James and M. Winkler, *http://www.cern.ch/minuit, CERN (2004).* 62

[Kal05] V.A. Kalinin, O.I. Batenkov, V.N. Dushin, *"Development of the Model for Calculation of the evaporation spectra of neutrons emitted from ^{252}Cf(sf) Fission Fragments"*, (2005), private communication. 88

[Kau74] S.B. Kaufman, E.P. Steinberg, B.D. Winlkins, et al. , *Nucl. Instr. and Meth.* **115** (1974) 47.

[Khr99] V.A. Khriatchkov,F.-J. Hambsch, *private communication* (1999). 24

[Kno00] G.F. Knoll, *Radiation Detection and Measurements, 3rd edition* (2000). 10

[Kor03] N.V. Kornilov, V.A. Khriatchkov, M. Dunaev, et al. , *Nucl. Instr. and Meth.* **A497** (2003) 467-478. 4, 64, 71, 81

[LeC59] K.J. Le Couteur,D.W. Lang, *Nucl. Phys.* **13** (1959) 32. 90

[LeCroy] http://www.lecroy.com. 17

[Leo87] W. R. Leo, *"Techniques for Nuclear and Particle Physics Experiments", Springer-Verlag, Berlin, Germany, ISBN 3-540-17.86-2* (1987). 66, 105

[Lin63] J. Lindhard, M. Scharff, H.E. Schiøtt , K. Dan Vidensk , *Selsk. Mat.-Fys. Medd.* **33** (1963) no.14.

[Lit06] O. Litaize, *Proc. 10th Inter. Symp. on Radiation Physics (ISRP-10), 17-22 september 2006, Coimbra, Portugal.* 62

[Man87] W. Mannhart, *"Properties of Neutron Sources"* IAEA-TECDOC-410, IAEA, Vienna, (1987) 158. 79

[NILab] http://www.ni.com/labview. 14

[ORTEC] http://www.ortec-online.com. 17

[Sch66] H.W. Schmitt, J.H. Neiler, F.J.Walter, *Phys. Rev.* **141** (1966) 1146. 46, 48, 52, 54

[Sch02] C. Schmitt, *"Fission des noyaux lourds et superlourds"* PhD Thesis, University of Strasbourg, 2002. 62

[Smi68] D.L. Smith, et al., *Nucl. Instr. and Meth.* **64** (1968) 157. 10

[Tov02] F. Tovesson, et al., *Proc. Int. Conf. on Nucear Data for Science and Technnology (ND2001), Tsukuba, Japan, 2001, Eds. R.C. Haight et al., p.673.* 8, 47, 52

[Ver68] V.V. Verbinski, et al., *Nucl. Instr. and Meth.* **65** (1968) 8. 10

[Viv98] F. Vivès *Mesure des propriété des fragments de fission de la réaction* ^{238}*U(n,f) à des énergies de neutrons incidents jusqu'à 5.8 MeV* PhD Thesis, Universite de Bordeaux I, 1998. 9

[Wat04] L. S. Waters, *Los Alamos National Laboratory, USA* (2004). 61

[Wei37] E. Weissenberger, *Phys. Rev.* **52** (1937) 295. 90

[Whe63] S.L. Whetstone, *Phys. Rev.* **131** (1963) 1232. 52

List of Figures

List of Tables

Resume

Ce travail de thèse décrit la mise en place d'un dispositif expérimental basé sur la digitalisation des signaux et dédié à l'étude des neutrons prompts de fission émis en coincidence avec les fragments de fission lors de la fission spontanée du 252Cf. Ce dispositif comprend une chambre à ionisation utilisée pour la détection des fragments de fission ainsi qu'un scintillateur liquide de type NE213 pour la détection des neutrons prompts. Nous montrons comment l'analyse délicate des signaux digitalisés nous a permis de déterminer à la fois les distributions en masse et en énergie cinétique des fragments de fission ainsi que le spectre en energie et la multiplicité des neutrons de fission.

Mots clefs : Digitalisation des Signaux, Spectroscopie de Fragments de Fission, Spectroscopie de Neutrons Prompts, Scintillateur, Fission Spontanée du 252Cf.

Abstract

The present work demonstrates the application of the digital technique for nuclear measurements. This method has been implemented for measurements of promptly emitted fission neutrons in coincidence with fission fragments from 252Cf(sf). A double Frisch-grid ionization chamber is used as fission fragment detector. The promptly emitted neutrons are detected by a NE213 liquid scintillation detector. This work displays how delicate analysis of the digitalized signals permitted us to infer the mass and kinetic energy distributions of the fission fragments as well as the neutron energy spectrum and multiplicity.

Keywords : Waveform Digitizer, Fission Fragment Spectroscopy, Neutron Spectroscopy, Scintillator, Spontaneous Fission of 252Cf.
